CENTRAL RESEARCH LIBRARY
DOCUMENT COLLECTION

OAK RIDGE NATIONAL LABORATORY
operated by
UNION CARBIDE CORPORATION
NUCLEAR DIVISION
for the
U.S. ATOMIC ENERGY COMMISSION

LOCKHEED MARTIN ENERGY RESEARCH LIBRARIES
3 4456 0513754 4

ORNL - TM - 2615

1

THE SURFACE PLASMON RESONANCE EFFECT IN GRATING DIFFRACTION

(Thesis)

J. J. Cowan, E. T. Arakawa, and R. H. Ritchie

OAK RIDGE NATIONAL LABORATORY
CENTRAL RESEARCH LIBRARY
DOCUMENT COLLECTION
LIBRARY LOAN COPY
DO NOT TRANSFER TO ANOTHER PERSON
If you wish someone else to see this document, send in name with document and the library will arrange a loan.

Submitted by J. J. Cowan as a dissertation to the Graduate School of The University of Tennessee in partial fulfillment of the requirements for the degree of Doctor of Philosophy.

LEGAL NOTICE

This report was prepared as an account of Government sponsored work. Neither the United States, nor the Commission, nor any person acting on behalf of the Commission:

A. Makes any warranty or representation, expressed or implied, with respect to the accuracy, completeness, or usefulness of the information contained in this report, or that the use of any information, apparatus, method, or process disclosed in this report may not infringe privately owned rights; or

B. Assumes any liabilities with respect to the use of, or for damages resulting from the use of any information, apparatus, method, or process disclosed in this report.

As used in the above, "person acting on behalf of the Commission" includes any employee or contractor of the Commission, or employee of such contractor, to the extent that such employee or contractor of the Commission, or employee of such contractor prepares, disseminates, or provides access to, any information pursuant to his employment or contract with the Commission, or his employment with such contractor.

ORNL-TM-2615

Contract No. W-7405-eng-26

HEALTH PHYSICS DIVISION

THE SURFACE PLASMON RESONANCE EFFECT IN GRATING DIFFRACTION

J. J. Cowan, E. T. Arakawa, and R. H. Ritchie

Submitted by J. J. Cowan as a dissertation to the
Graduate School of The University of Tennessee
in partial fulfillment of the requirements
for the degree of
Doctor of Philosophy

NOVEMBER 1969

OAK RIDGE NATIONAL LABORATORY
Oak Ridge, Tennessee
operated by
UNION CARBIDE CORPORATION
for the
U. S. ATOMIC ENERGY COMMISSION

LOCKHEED MARTIN ENERGY RESEARCH LIBRARIES

3 4456 0513754 4

ACKNOWLEDGMENTS

The authors wish to express appreciation to members of the Radiation Physics Section for support during this study. In particular, they extend thanks to Dr. R. N. Hamm for assistance in the computer programming of the dispersion relations, to Dr. R. D. Birkhoff for his special interest in the research problem, and to J. A. Harter and A. G. Kenerly for helping to maintain the electronic apparatus.

One of us (JJC) would like to thank the U. S. Public Health Service and the University of Tennessee for a U. S. Public Health Service Fellowship which supported him during this study.

ABSTRACT

Anomalies in the intensity of p-polarized light from concave diffraction gratings and from thin grating foils have been analyzed in terms of an interaction between the incoming photon and a surface plasmon resonance in the grating surface.

Non-radiative surface plasmon dispersion curves have been obtained for various metal- and dielectric-metal layers on concave gratings. The cases investigated were an Al substrate coated with (1) Ag, Au, and Al metals (2) Al_2O_3, MgF_2, and diffusion pump oil dielectrics, and (3) Al_2O_3 , Al, and Al_2O_3 composite layers. The wavelength region investigated was from the infrared through the vacuum ultraviolet (14000 - 500 A°). The experimental results are in substantial agreement with the theoretical dispersion curves for these cases.

Also considered were radiative mode surface plasmon excitations in thin Ag grating foils and in Al and Al - Al_2O_3 - Al layers on concave gratings. A study was also made of the anomalous peak intensities for (1) the first order on-blaze diffracted spectra (2) metal overcoating layers of various thicknesses, and (3) some aspects of the reflected (zero-order) and off-blaze first order spectra.

TABLE OF CONTENTS

CHAPTER	PAGE
I. INTRODUCTION	1
Anomalies in Grating Polarization	2
Surface Waves	6
Scope of the Present Research	17
II. THEORY	19
The Rayleigh Wavelengths	19
Classical Macroscopic Theory	20
The bulk (volume) plasma frequency	26
Bound electrons	31
Surface plasma excitations	34
Wave dampling	40
Thin foil bounded by vacuum	41
Dielectric on a semi-infinite metal substrate	46
Metal layer on a dielectric-coated metal layer	50
Dielectric-coated metal layer on a second dielectric-coated metal layer	51
Metal substrate coated with a double dielectric layer	55
Quantum Mechanical Considerations	57
Volume and surface plasmons	58
The quantum hydrodynamical model	59
The radiative mode	61

CHAPTER PAGE

The non-radiative modes 69

Surface plasmon self energy 74

III. EXPERIMENTAL APPARATUS 75

Principal Components 77

Light sources 77

Vacuum monochromator system 81

Vacuum system 83

Variable-angle optical system 83

Polarizers 84

Detection and amplification system 84

Vacuum evaporator 86

Reflectance chamber 87

Film thickness monitor 87

Anodic oxidation apparatus 87

Diffraction gratings 88

IV. EXPERIMENTAL PROCEDURES 90

Preparation of Grating Surfaces 90

Vacuum evaporation 92

Anodic oxidation technique 95

Grating foils 98

The Vacuum Monochromator System 101

Optical alignment 101

Resolution 102

CHAPTER PAGE

Polarization measurements 103

The Reflectance Chamber 107

The Variable-Angle Apparatus 107

V. RESULTS AND DISCUSSION 111

Non-Radiative Surface Plasmon Dispersion 111

Metal layers on metal substrates - visible and near-ultraviolet 111

Dielectric layers on aluminum substrates - visible and near ultraviolet regions, Al_2O_3 and diffusion pump oil 126

Magnesium fluoride 135

Dielectric layers on metal substrates - vacuum ultraviolet region 137

Intensity Considerations 148

The zero order (reflected) beam 150

The first order off-blaze spectrum 150

Metal layers 153

The first order on-blaze spectrum 153

Grating Foils and the Radiative Mode 157

Foils on concave gratings - non-radiative mode 157

Concave gratings - radiative mode 162

Grating foils 164

The grating profile 169

CHAPTER PAGE

VI. SUMMARY 171

BIBLIOGRAPHY 175

APPENDIXES 181

Appendix A 182

Appendix B 185

Appendix C 187

Appendix D 189

LIST OF TABLES

TABLE		PAGE
I.	Anomalous Wavelengths for $\theta = 20°$. Rayleigh Passing-off Orders, m , are Compared with Branch Values, n	121
II.	Calculation of $\lvert\kappa_n\rvert$ for $\theta = 20°$ Using Anomalous Wavelengths and Equation (93)	123
III.	Wavelengths of Anomalous Peaks at $\theta = 35°$ for a Layer of Al: (a) Freshly Vacuum-Evaporated at 10^{-6} Torr; (b) the Same Layer Exposed to Air for 10 Hours . .	128
IV.	Wavelengths of Anomalous Peaks at $\theta = 25.7°$ for an Al-Coated Grating (a) Used in a Monochromator for Seven Months and Coated with Diffusion Oil; (b) Same Surface with the Oil Removed; (c) the Surface Coated with 600 A° Al and Exposed to Air for 24 Hours	131

LIST OF FIGURES

FIGURE PAGE

1. Diffraction Grating Nomenclature for Incident (I_o) and Reflected (R) Light and Diffracted Orders for Grating with Line Spacing δ and Blaze Angle θ . The Diffraction Angle is β for the n = +1 Diffracted Order and the Incidence Angle is α 3

2. Typical Dispersion Relations for the Non-retarded Surface Modes 10

3. Surface Charge Distribution and Field Configurations for (a) Tangential (Symmetric) Mode on Thin Foil (b) Normal (Antisymmetric) Mode on Thin Foil (c) Non-radiative Mode as Foil Thickness Approaches Infinity 11

4. Typical Dispersion Relations for the Retarded Surface Modes 12

5. Metal-Dielectric Configurations: (a) Semi-infinite Metal-Vacuum (b) Metal Foil Bounded by Vacuum (c) Semi-infinite Metal-Dielectric-Vacuum (d) Semi-infinite Metal-Dielectric-Metal-Vacuum (e) Semi-infinite Metal-Dielectric-Metal-Dielectric-Vacuum (f) Metal Foil Bounded by Uneven Dielectric Layers and by Vacuum (g) Semi-infinite Metal-Dielectric 1-dielectric 2-Vacuum 35

FIGURE PAGE

6. (a) - (e) Photon-Radiative Surface Plasmon Interactions in Thin Grating Foils (f) Photon- Non-radiative Surface Plasmon Interaction on Semi-infinite Metal Substrate . . . 65

7. Schematic Diagram of Light Source, Spectrometer, and Reflectance Chamber 76

8. Schematic Diagram of Variable-Angle Apparatus. θ is the Half-angle Between the Source and Detector and α is the Angle of Incidence to the Grating Surface 78

9. Configuration of the Light Source Capillary Tube 80

10. Anodic Oxidation Apparatus 96

11. Oxide Thickness Versus Applied Voltage 97

12. Polarization Parameter, $\rho = r_p/r_s$, Versus Wavelength for Triple Polarizer 106

13. Anomalous Polarization Peaks in p-Polarized Spectra for Al-coated Grating 112

14. Photon Energy of Anomalous Peaks Versus Half-angle, θ , Between Source and Detector for Au (Dotted Lines) and Al (no Dotted Lines) Layers on Grating Surface 114

15. Anomalous Polarization Peaks in $|p - s|$ Difference Spectra for Ag-coated Concave Grating 116

16. Photon Energy of Anomalous Peaks Versus Half-angle, θ , Between Source and Detector for Ag (Solid Lines) and Al (Dotted Lines) Layers on Grating Surface 117

FIGURE PAGE

17. Feynman Diagram for Photon - Non-radiative Surface Plasmon Interaction (b) Surface Plasmon Dispersion Relation for Al, Ag, and Au Coatings on Grating. Dotted Lines - Theoretical Curves 119

18. Theoretical Tangential Mode Surface Plasmon Dispersion Curves for Various Thicknesses of Al and Au on an Al Substrate 125

19. Anomalous Polarization Peaks for Concave Grating After Two Month Exposure in Vacuum System 129

20. Anomalous Polarization Peaks for Al (Grating) Substrate Coated with Various Thicknesses of Anodized Al_2O_3 132

21. Surface Plasmon Dispersion Curves for Different Anodized Al_2O_3 Thicknesses on Concave Grating. ● - Left Edge, O - Right Edge, ▲- Center 133

22. Anomalous Polarization Peaks in $|p - s|$ Difference Spectra for 350 A° MgF_2 - Coated Concave Grating 136

23. Energy of Anomalous Peaks Versus Angle. Solid Lines, Au; Dotted Lines, MgF_2 138

24. Surface Plasmon Dispersion Curves for (a) 50 A° Al_2O_3 and (b) 350 A° MgF_2 on Al Substrate. Dotted Lines - Theoretical Curves 139

25. Change in Polarization Ratio, R_p/R_s, With Time for Vacuum Evaporated Ag, Au, and Al Coatings on Concave Grating 140

FIGURE PAGE

26. Theoretical Surface Plasmon Dispersion Curves for Various Thicknesses of Al_2O_3 on an Al Substrate. Uses $\eta(\omega) = \eta_1$ for Al_2O_3 and $\varepsilon(\omega) = \varepsilon_1$ for Al 142

27. Theoretical Surface Plasmon Dispersion Curves for Various Thicknesses of Al_2O_3 on an Al Substrate. Uses $\eta = \eta_1 + \eta_2$ for Al_2O_3 and $\varepsilon = \varepsilon_1$ for Al. Dotted Line - 20 A° Al_2O_3 and 20 A° Pump Oil on Al Substrate 144

28. Change in Polarization Ratio, R_p/R_s, with Time for a New Diffraction Grating 146

29. Polarization Ratio, R_p/R_s, for Al Grating Coated with 650 A° Al_2O_3 149

30. Anomalous Polarization Phenomena in (a) Specular Reflected (Zero-order) and (b) Diffracted 1st Order On-blaze Spectra. Reflected Spectrum is 100 Times More Intense Than Diffracted Spectrum 151

31. First-order Diffracted On- and Off-blaze Spectra for Ag-coated Grating 152

32. Relative Intensity in Spectra of Grating Coated with Various Thicknesses of Ag 154

33. Relative Intensities of Anomalous Peaks for Positive Branches, +n, as a Function of Angle, θ 155

34. Relative Intensities of Anomalous Peaks for Negative Branches, -n, as a Function of Angle, θ 156

FIGURE PAGE

35. Non-radiative Surface Plasmon Dispersion Curves for Al Substrate Coated with 650 A° Al_2O_3, 150 A° Al, 40 A° Al_2O_3, and Vacuum. Dotted Line - Normal Mode; Heavy Dashed Line - Tangential Mode; Medium Dashed Line - 40 A° Al_2O_3 on Al Substrate; Solid Line - Pure Al 159

36. Radiative Surface Plasma Modes for Al Foil of Thickness (a) 12000 A° (b) 240 A°, for Different Angles of Incidence 165

37. Plasma Radiation Excited by Light for 300 A° Ag Grating Foil. Intensity of Transmitted Beam is 100 Times that of Diffracted Beam 167

38. Relative Intensity at the Plasma Wavelength of p-Polarized Peak in Diffracted Beam for Various Diffraction Angles 168

39. (a) Grating Profile of 600 Line/mm Concave Grating Exhibiting Anomalies (b) Grating Profile of 600 Line/mm Plastic Replica Grating Exhibiting no Anomalies 170

CHAPTER I

INTRODUCTION

Anomalies in the intensity of light diffracted from reflection gratings have been the subject of extensive experimental and theoretical study since they were first observed in 1902 by Wood, who termed them anomalies because they could not be explained by the ordinary grating theory of that time. These anomalies are rapid variations in the intensity of diffracted light that occur over a fairly narrow wavelength region when the incident light is polarized with its electric vector parallel to the plane of incidence which in turn is perpendicular to the rulings on the grating. For a source with a continuous, slowly varying spectrum these anomalies appear as sharp peaks or dips in the diffracted spectra.

There has been a renewed interest in grating anomalies for two primary reasons. One is the increasingly widespread use of concave gratings in monochromators, due largely to the ability of these gratings to disperse and focus light over a large spectral region, including the vacuum ultraviolet, a region that has become of great importance lately in space research and in solid state physics. In experiments where the state of polarization of the light passing from the monochromator to the specimen under study is required, it is desirable to know something about these anomalous polarization effects and in many cases to modify or eliminate them.

A second reason for the interest in grating anomalies is the current belief that they can be explained in terms of plasma resonances in the surface of the metal coating of the grating. These resonances involve the excitation of certain collective modes of oscillation of the electron gas that in ordinary metal surfaces can be difficult to observe but in grating surfaces are detected without great difficulty. Studies of the anomalies can lead to a better understanding of plasma phenomena in metals, such as the dispersion of surface plasma waves, the interaction of electromagnetic radiation and plasma waves, and the elementary interactions.

I. ANOMALIES IN GRATING POLARIZATION

The first theoretical treatment was given by Rayleigh in 1907 and was based on scattering between the incident and diffracted waves. This theory involved an expansion of the electromagnetic field in terms of outgoing waves which predicted a singularity at certain specified wavelengths [Rayleigh (1907b)]. In simplest terms the theory says that for a given angle of incidence there might exist several diffracted orders, one of which, for a given wavelength of light, might be a "passing-off" order; that is, one for which the angle of diffraction from the grating normal is 90 degrees. This passing-off order would consist of light moving across the grating and parallel to the surface (Figure 1). This light could then be scattered into one of the diffracted orders and appear as a peak in intensity in that order at that

ORNL-DWG 69-7582

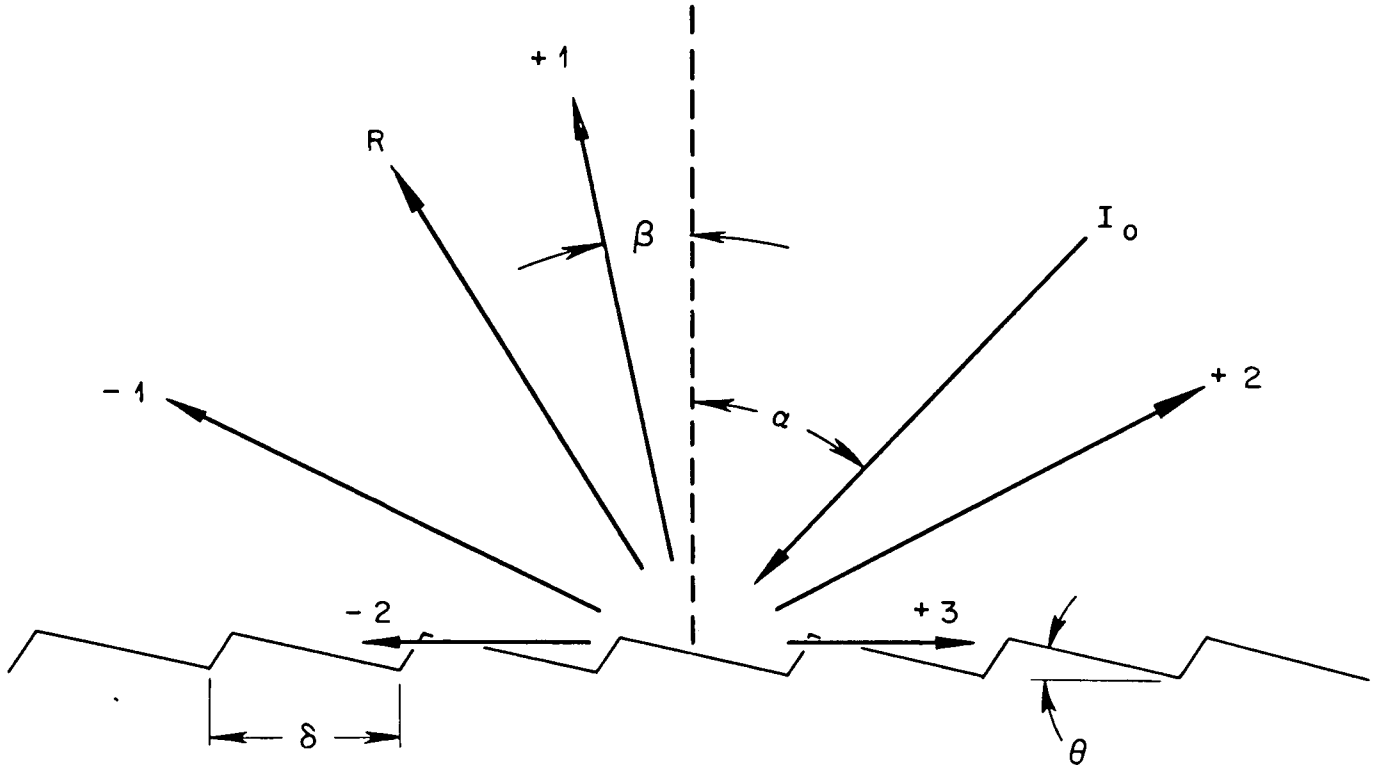

Figure 1. Diffraction grating nomenclature for incident (I_o) and reflected (R) light and diffracted orders for grating with line spacing δ and blaze angle θ . The diffraction angle is β for the n = +1 diffracted order and the incidence angle is α .

particular wavelength. These wavelengths, which can be calculated from the grating equation (Chapter II), are known as the Rayleigh wavelengths [Rayleigh (1907a)].

Rayleigh's theory was useful in predicting the position of the wavelengths but not their shape or intensity. Other theories presented in recent years, in an attempt to correct this deficiency, have been based on rather sophisticated multiple wave scattering techniques [Twersky (1952, 1962)]. A good review of these has been given by Hessel and Oliner (1965). The multiple-scattering theories predict the position and shapes of the anomalies fairly well, but are only applicable for gratings having shallow grooves. It has been shown, by Palmer (1952, 1956) that for gratings with deep grooves another anomaly appears for light polarized perpendicular to the plane of incidence. This type of anomaly was not observed, however, in the present work because only gratings with comparatively shallow grooves were used.

Some of the more recent treatments of Wood's anomalies have taken into account the dielectric properties of the metal coating of the grating. In the treatment of Fano (1941) the passing-off plane wave of Rayleigh is replaced by surface waves in the metal that can be resonantly excited by incident light. The wave vector of the incident light is modulated by the periodic grating structure so that it can resonate with one of the surface waves having a similar wave vector. Fano showed that the wavelengths at which this occurs are approximately equal to the Rayleigh wavelengths.

A recent extension of Fano's idea was made by Hägglund and Sellberg (1966) who took into special account the reflection and absorption properties of the optical grating for Wood's anomalies. They were able to confirm in some quantitative detail an earlier observation of Wood's that the energy for the anomalous peaks comes from the central image [Wood (1935)]; that is, peaks in the diffracted orders correspond to dips in the zero order at the same wavelength. Their theoretical treatment was similar to Fano's in that one represents the fields inside and outside the grating as an infinite superposition of plane waves, both homogeneous and inhomogeneous and expands the equation for the grating surface as a Fourier series. The unknown field amplitudes are found from the boundary conditions.

Recent experimental work has been done by Stewart and Galloway (1962) on the Wood's anomalies appearing in the zero order and some of the diffracted orders. They observed that where two anomalies occur at close to the same wavelength (because of passing-off orders propagating in opposite directions on the grating surface) there is a reluctance of the anomalous peaks to coincide. Elsewhere the observed wavelengths correspond rather closely to the Rayleigh wavelengths.

One of the most comprehensive theoretical treatments of Wood's anomalies based on classical electromagnetic theory was given by Hessel and Oliner (1965). Their treatment makes use of a surface reactance to take into account the standing waves in the grating surface and derives the locations and shapes of the anomalies. It is shown that two types

of anomalies may exist: A Rayleigh type due to the emergence of a new spectral order at grazing angle, and a resonance type which is related to the guided complex waves supportable by the grating. It is shown that for shallow grooves such as are typical for many diffraction gratings the two anomalies are virtually indistinguishable. In principle, their guided wave approach is similar to that of Fano's where resonances can occur between the incident light and the surface waves on the grating.

Anomalous behavior has not been restricted to the optical range. Palmer, Evering, and Nelson (1965) and Evering (1966) detected anomalies from reflection gratings with rectangular profiles in the microwave region. In fact, Evering produced artificial anomalies by reflecting microwaves across the grating as if they were in a passing-off order. Evering and Aujouanne (1969) later repeated the experiment in the optical region with laser light.

II. SURFACE WAVES

The use of surface waves by several of the authors cited above to explain Wood's anomalies leads us to investigate surface wave phenomena in metals in more detail in their general historical context and in their specific application to the problem of grating anomalies.

In 1909 Sommerfeld showed that an electromagnetic wave could propagate at the boundary between two dielectric media. The solution of Maxwell's equations for this case was not a plane wave but a bound

surface wave of the transverse magnetic (TM) mode type [Sommerfeld (1909)]. It has since become known as the Sommerfeld surface wave [Stratton (1941)]. It was specifically derived for the case of radio frequency waves propagating along the surface of the earth at the earth-air boundary, but it is perfectly applicable to optical frequency waves moving along a metal-vacuum boundary. One interesting property of a TM wave is that it has a small longitudinal electric field component and as such is parallel to the direction of wave motion. In a metal the oscillating longitudinal field can interact with the conduction electrons which in turn oscillate in the same direction. The essentially free conduction electrons and the lattice ions constitute a plasma in the metal. The conduction electron oscillation brought about by the surface wave can be interpreted as a charge wave, plasma wave, or more exactly, as a surface plasma wave.

Another interesting property of this surface wave is that its phase velocity is less than the speed of light. Thus an incident plane wave cannot excite the surface wave because momentum and energy cannot be simultaneously conserved at the boundary. Exceptions can occur when the surface is not perfectly smooth.

The Sommerfeld wave is only a special case of plasma excitations in metals. There is also a bulk volume mode and, where the metal is thin, more than one surface mode. Pines (1956) has shown that when fast electrons are scattered by thin solid films, collective energy losses occur in the valence electrons of the metal. A collective loss is

described as an energy transfer to a number of electrons moving cooperatively in consequence of their mutual interaction, a type of motion that is characteristic of the behavior of plasmas. The term "plasmon" was introduced to describe the quantum of elementary excitation associated with this high-frequency collective motion. The energy associated with this loss is

$$\hbar \omega_p = \hbar \left(\frac{4 \pi n e^2}{m} \right)^{1/2}$$

where ω_p is the plasma frequency, n the valence electron density, and m the free electron mass. We shall refer to ω_p as the bulk plasma frequency since it depends only on the bulk properties of the metal.

Ritchie (1957) has shown in a dielectric treatment of an electron gas that when the boundary is taken into account in an interaction of fast electrons with metal foils, a new energy loss appears at a reduced frequency $\omega_p / \sqrt{2}$. This is due to the depolarizing effect of the vacuum at the metal-vacuum interface. The quantum of the energy loss at the reduced frequency, $\hbar \omega_p / \sqrt{2}$, is referred to as the surface plasmon. The term surface plasmon is also used to describe the quanta of surface plasma waves. Ritchie also derived a dispersion relation for surface plasmons on thin foils having the following form

$$\omega = \frac{\omega_p}{\sqrt{2}} \left[1 \pm \exp(-a\kappa) \right]^{1/2}$$

where a is the foil thickness and κ is the wave vector of the surface plasma wave and which reduces to the previous expression for large values of a or κ. A plot of this relation is shown in Figure 2. The two branches of this dispersion relation describe two different distributions of the electric field in the interior of the foil, or two modes of plasma oscillation. The positive sign is associated with electronic motion predominantly normal to the surface of the foil and is referred to as the normal surface plasmon. The minus sign involves motion predominantly parallel to the surface, and this mode is referred to as the tangential surface plasmon. Typical electric field patterns are shown in Figure 3. The above dispersion relation, which is the electrostatic solution, is changed when retardation is taken into account; i.e., when the full set of Maxwell's equations including the radiation terms are used. In this case we obtain radiative and non-radiative modes on each side of the light line, $\omega = ck$ (Figure 4). The non-radiative modes are split into the higher-energy normal mode and a lower energy tangential mode, which, as the foil thickness increases, get closer together and eventually merge into a single non-radiative mode for a semi-infinite metal surface. This latter mode is identical with the Sommerfeld surface wave discussed earlier. This non-radiative dispersion relation has been derived by Ritchie and Eldridge (1962), Otto (1965), and Kloos (1968). Radiative modes have been considered by Kliewer and Fuchs (1967) and by Romanov (1964).

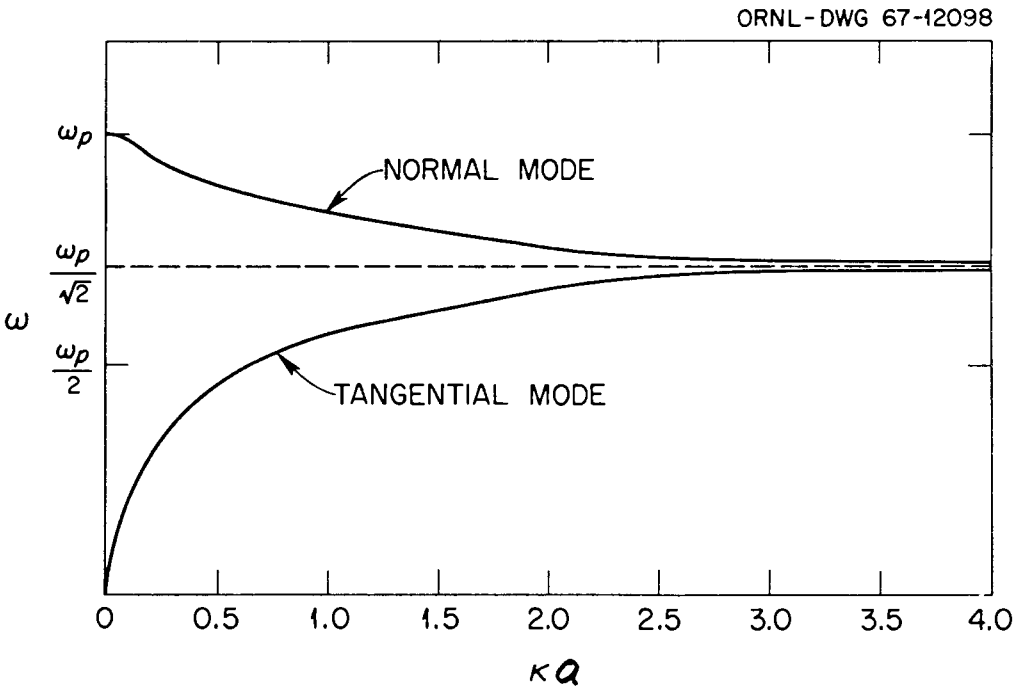

Figure 2. Typical dispersion relations for the non-retarded surface modes.

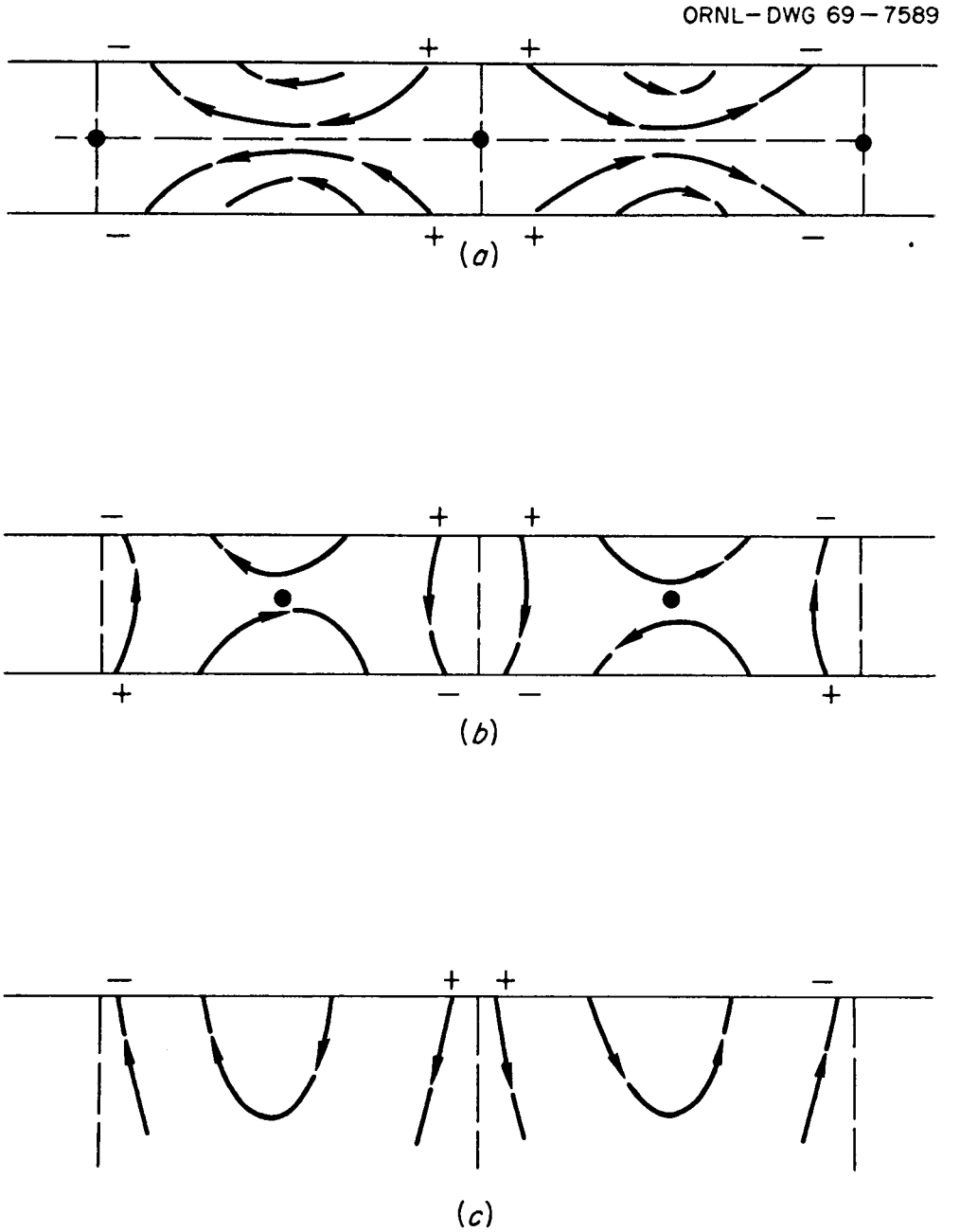

Figure 3. Surface charge distribution and field configurations for (a) tangential (symmetric) mode on thin foil (b) normal (anti-symmetric) mode on thin foil (c) non-radiative mode as foil thickness approaches infinity.

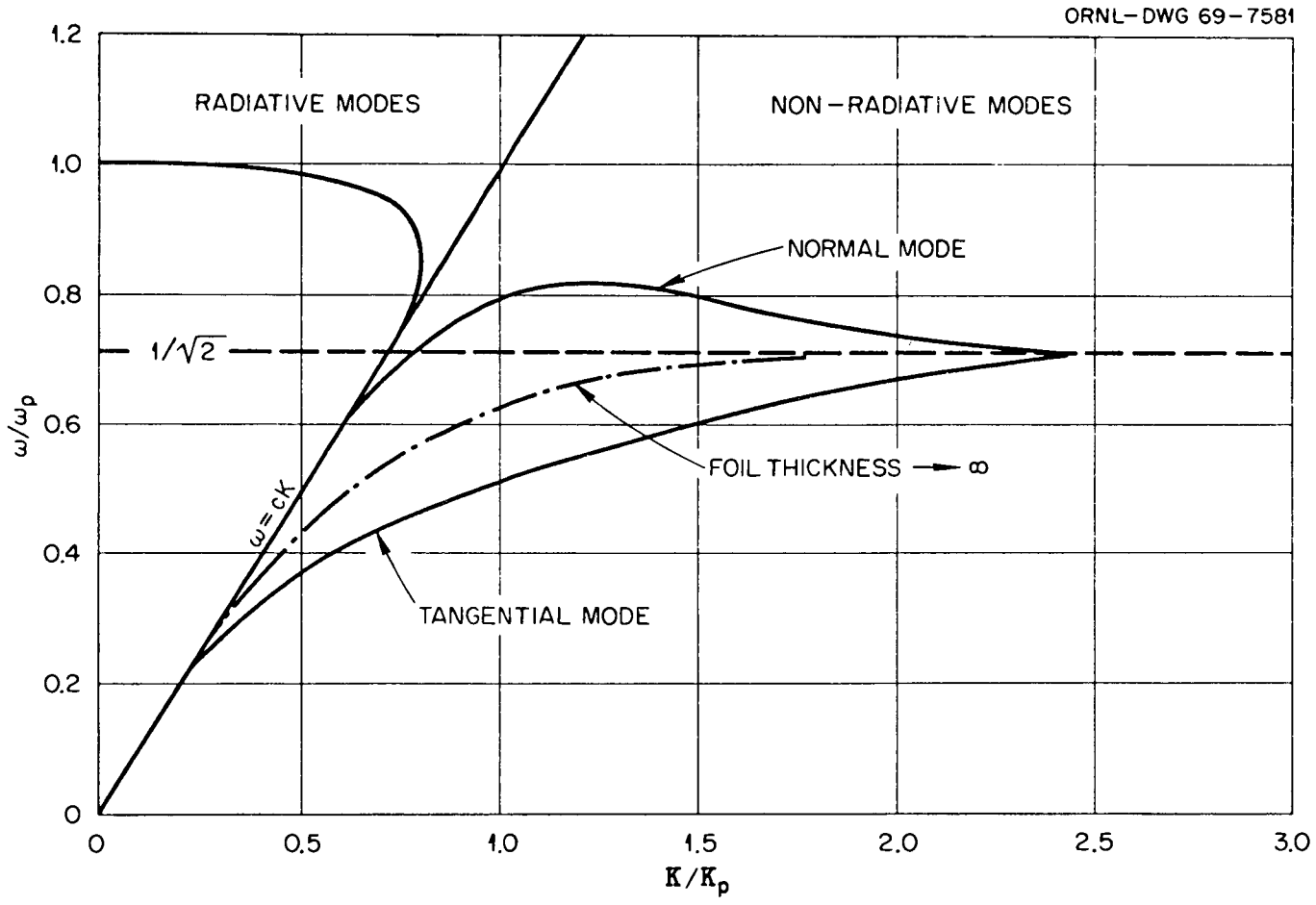

Figure 4. Typical dispersion relations for the retarded surface modes. $\kappa_p = \omega_p/c$.

The energy losses discussed above have been determined experimentally by measuring the energy of the electrons after they have passed through the foil or by reflection from the foil surface. Ferrell (1958) first suggested that for thin foils plasma radiation might occur at the characteristic (bulk) plasma frequency and that detection of this radiation would allow the energy loss to be measured directly. Ferrell considered the excitation of the (radiative) normal plasma mode, which because of the electronic motion normal to the foil would produce radiation similar to an oscillating dipole. Radiation of the non-radiative modes was discounted at that time because of the energy and momentum considerations mentioned earlier. This normal mode radiation has since been observed experimentally many times [Steinmann (1960), Arakawa, Herickhoff, and Birkhoff (1964), Boersch, et al. (1965) and Arakawa, Davis and Birkhoff (1964)]. Ritchie and Eldridge (1962) showed that the mathematical description of this radiation was identical to that of transition radiation proposed earlier by Frank and Ginsburg (1945).

In experiments designed to detect the surface losses predicted by Ritchie, it was found for many metals, for example, aluminum and magnesium, that an energy loss did occur at $\hbar\omega_p/\sqrt{2}$ for a pure metal surface, but if the surface were allowed to oxidize this loss peak disappeared and a new loss peak appeared at a still lower energy. Stern and Ferrell (1960) showed that this new loss line could be accounted for by the thin oxide layer that forms naturally on aluminum and

magnesium. By utilizing the dielectric constants of the oxide layer and metal surface, they showed that this new loss should occur at the reduced frequency $\omega_p/\sqrt{1+\varepsilon}$ where ε is the dielectric constant of the oxide. For a metal bounded by a vacuum this reduces to Ritchie's result.

That the non-radiative mode might indeed radiate under certain conditions was pointed out by Stern (1966) and later verified in an experiment by Teng and Stern (1967). As mentioned previously this mode does not radiate because it propagates at less than the speed of light, but a certain amount of surface roughness may permit momentum transfer to occur that would permit coupling between the surface wave and light. In Teng's experiment a grating surface coated with thick layers of aluminum and silver was bombarded by normally incident electrons and light from the plasma oscillations was detected. The surface roughness in this experiment was provided by the periodic grating structure. From his data dispersion curves for the non-radiative surface mode were constructed for aluminum and silver.

The plasma excitation experiments discussed up to this point have all been performed where the exciting agent is a beam of fast electrons. But one should also be able to excite plasma oscillations with a plane-polarized beam of light. This was first predicted by Ferrell and Stern (1962), who reasoned that the decay of normal mode radiative plasmons into photons indicated strong coupling between them and that the inverse process of exciting plasmons by incident photons should be possible.

Since a component of the incident electric field perpendicular to the foil normal is required to excite normal mode plasmons, this requires light polarized with its electric vector parallel to the plane of incidence (p-polarized light). Because of momentum considerations this radiation appears in the reflected beam only, and there is a corresponding dip in intensity in the transmitted beam. This phenomenon has since been experimentally verified many times [Huebner, et al. (1965), Brambring (1967), McAlister and Stern (1963)].

That plasma radiation excited by light could appear in directions other than the reflected and transmitted beams was shown by Brambring and Raether (1965, 1967). In this experiment a thin Ag foil was irradiated at a large angle of incidence by p-polarized light and the emitted (polarized) light was detected at the bulk plasma frequency in a direction almost opposite to the reflected beam and at almost 90° to the transmitted beam. In order for such radiation to occur, some momentum transfer must occur at the foil surface to conserve momentum. An explanation was offered by Stern (1967) and by Wilems and Ritchie (1967). Stern's explanation was based on classical considerations in which a certain amount of random surface roughness is assumed for the foil surface. This roughness allows surface currents normal to the foil surface to exist and thus normal mode radiation could occur. Wilems and Ritchie used a quantum-mechanical approach involving a photon-plasmon interaction. The normal modes of electronic motion in a plane plasma slab were found from the Bloch hydrodynamical equations for a

degenerate electron gas. The plasmon field was quantized with the assumption that deviations from a uniform electron density, such as might be found from surface irregularities, phonons, impurities, etc., could be represented by a static density variation function. Photons and plasmons could then scatter on these density variations, allowing momentum to be conserved at the boundary. These theories have agreed quite well with the experimental results. This type of radiation, which has come to be known as PREL (plasma resonance radiation excited by light) has been observed in several other experiments [Bösenburg and Raether (1967), Schreiber and Raether (1966), Steinmann, Hofmann, and Stettmaier (1966)]. In an interesting speculation, Wilems and Ritchie predicted that PREL radiation should be easily seen in grating foils where the surface roughness (static density variation) is regular and has a known value. The light should be emitted into definite directions determined by the diffraction equation instead of into a sphere of directions as in the systems studied by Raether and in most cases should be more intense.

The preceding experiments with PREL radiation have been concerned with radiative mode excitation in thin foils. Incident light can also excite the non-radiative mode in thick metal substrates if certain conditions are met. One is that the incident light pass into a medium and be incident on the metal surface at a phase velocity less than light. Non-radiative surface plasma waves have been produced in this way by the exponentially decaying wave from a quartz prism at a quartz-air-metal

interface in which absorption takes place at the plasma wavelengths, but no radiation is produced [Otto (1968)]. The non-radiative mode has also been excited by the exponentially decaying wave from an air-quartz-metal interface where decay of this mode into radiation results from the surface roughness [Kretschmann and Raether (1968)]. Another method of exciting the non-radiative mode is to directly irradiate a metal having surface roughness that can, as with the PREL experiments, allow momentum conservation to occur at the metal surface. In the case of diffraction gratings this roughness is provided by the regular grating structure. In this sense the grating serves the same purpose for the case of incident light as it does for the case of an incident beam of electrons where radiation is produced. Beside the electron beam experiment, Teng and Stern (1967) also conducted an experiment where the grating was irradiated by p-polarized light and the reflected beam analyzed. Dips were found at the plasma frequencies in this zero-order beam that corresponded to peaks at the same frequencies for radiation resulting from the electron bombardment.

A review of optical plasma resonance phenomena in solids has been given by Steinmann (1968).

III. SCOPE OF THE PRESENT RESEARCH

The previous experiments have suggested many possibilities for studying photon-plasma interactions in grating structures. The objects of the present research were essentially the following: (1) extend the wavelength region covered in the usual studies of Wood's anomalies

from the infra-red and visible into the near- and vacuum-ultraviolet regions; (2) investigate the non-radiative modes by constructing dispersion curves from the measured anomalous wavelengths for different metal and dielectric coatings on concave reflecting gratings and comparing these with the theoretical curves; (3) investigate the radiative mode by conducting experiments with thin grating foils; (4) evaluate proposed quantum-mechanical descriptions of the photon-plasmon interaction; and (5) compare intensities of the anomalies in the various diffracted orders.

The major emphasis in this study was placed on the dispersion relation calculations for the non-radiative mode and a secondary emphasis on the intensity calculations and the work with thin foils.

CHAPTER II

THEORY

In this chapter we present first a discussion of the Rayleigh wavelengths based on the diffraction equation. This is followed by a section on classical macroscopic theory including derivations of the dispersion relations for all the geometries considered in this study. The final section is concerned with the quantum-mechanical description of the photon-plasmon interaction and how it relates to anomalous polarization effects.

I. THE RAYLEIGH WAVELENGTHS

The basic equation governing the performance of a diffraction grating is the grating equation giving the order, n, and the wavelength, λ, in terms of the grating spacing, δ, the angle of incidence, α, and the angle of diffraction, β, as follows

$$n \lambda = \delta (\sin \alpha \pm \sin \beta) . \tag{1}$$

For the reflection gratings used in this work, the plus sign is used when both the incident and diffracted rays are on the same side of the grating normal, and the minus sign, when they are on opposite sides of the normal. The order number, n, can also be positive or negative; the negative sign is used when the reflected beam lies between the incident and diffracted beams. For diffracted orders lying on the

opposite side of the reflected beam, the positive sign is used. These are illustrated in Figure 1, page 3.

For a certain choice of grating parameters and at a given angle of incidence it is possible for the diffracted beam to be parallel to the surface of the grating; i.e., the angle of diffraction, β , is 90°. In this case the grating equation becomes

$$m \lambda_R = \delta (\sin \alpha \pm 1) \tag{2}$$

where m and λ_R are the particular order and wavelength for which this occurs. The λ_R are called the Rayleigh wavelengths because it is these passing-off orders which Rayleigh said were responsible for the grating anomalies. The order number, m , can be positive or negative, as for n . In Figure 1, passing-off orders are indicated for $m = -2$ and $+3$.

If the grating is bounded by a dielectric having a dielectric constant, ε , instead of by vacuum, Equation (2) becomes

$$m \lambda_R = \delta (\sin \alpha \pm \sqrt{\varepsilon}) . \tag{3}$$

II. CLASSICAL MACROSCOPIC THEORY

In a homogeneous, isotropic medium of dielectric constant ε , permeability μ , and conductivity σ , Maxwell's equations take the form [Born and Wolf (1959)]:

$$\nabla \times \vec{H} = \frac{\varepsilon}{c} \frac{\partial \vec{E}}{\partial t} + \frac{4\pi}{c} \sigma \vec{E} \tag{4}$$

$$\nabla \times \vec{E} = -\frac{\mu}{c}\frac{\partial \vec{H}}{\partial t} \tag{5}$$

$$\nabla \cdot \vec{E} = \frac{4\pi}{\varepsilon}\rho \tag{6}$$

$$\nabla \cdot \vec{H} = 0$$

where we have used $\vec{J} = \sigma \vec{E}$, $\vec{D} = \varepsilon \vec{E}$ and $\vec{B} = \mu \vec{H}$.

If an electromagnetic disturbance is incident on the medium from outside, Equation (6) may be written $\nabla \cdot \vec{E} = 0$. This can be seen from the following considerations. Taking the divergence of (4) and using (6) we obtain

$$-\frac{\varepsilon}{c}\nabla \cdot \frac{\partial \vec{E}}{\partial t} = \frac{4\pi\sigma}{c} \cdot \frac{4\pi}{\varepsilon}\rho \quad .$$

The time derivative of (6) gives $\nabla \cdot \frac{\partial \vec{E}}{\partial t} = \frac{4\pi}{\varepsilon}\frac{\partial \rho}{\partial t}$ and elimination of $\nabla \cdot \frac{\partial \vec{E}}{\partial t}$ between these two equations gives $\dot{\rho} + \frac{4\pi\sigma}{\varepsilon}\rho = 0$ which on integration yields $\rho = \rho_o e^{-t/\tau}$ where $\tau = \varepsilon/4\pi\sigma$. For metals the relaxation time τ is usually on the order of 10^{-15} to 10^{-19} sec, which is smaller than the periodic time of the incident light wave, so ρ can be considered always zero. Furthermore, in a non-permeable medium, $\mu = 1$. So Maxwell's equations become, for a non-permeable, homogeneous isotropic conductor

$$\nabla \times \vec{H} = \frac{\varepsilon}{c}\frac{\partial \vec{E}}{\partial t} + \frac{4\pi}{c}\sigma \vec{E} \tag{7}$$

$$\nabla \times \vec{E} = -\frac{1}{c}\frac{\partial \vec{H}}{\partial t} \tag{8}$$

$$\nabla \cdot \vec{E} = 0 \tag{9}$$

$$\nabla \cdot \vec{H} = 0 \ .$$

If we use the vector identity $\nabla \times (\nabla \times \vec{E}) = \nabla(\nabla \cdot \vec{E}) - \nabla^2 \vec{E}$ and $\nabla \cdot \vec{E} = 0$ we obtain from Equations (7) and (8) the equation

$$\nabla^2 \vec{E} = \frac{\varepsilon}{c^2}\frac{\partial^2 \vec{E}}{\partial t^2} + \frac{4\pi\sigma}{c^2}\frac{\partial \vec{E}}{\partial t} \ . \tag{10}$$

If the incident field has the form $\vec{E} = \vec{E}_o e^{i\omega t}$ (7) and (8) can be rewritten as

$$\nabla \times \vec{H} = \frac{i\omega}{c}\left(\varepsilon + i\frac{4\pi\sigma}{\omega}\right)\vec{E} = 0$$

$$\nabla \times \vec{E} - \frac{i\omega}{c}\vec{H} = 0$$

and thus Equation (10) becomes the wave equation

$$\nabla^2 \vec{E} + \tilde{\kappa}^2 \vec{E} = 0 \tag{11}$$

where $$\tilde{\kappa}^2 = \frac{\omega^2}{c}\left(\varepsilon + i\frac{4\pi\sigma}{\omega}\right) \ . \tag{12}$$

A similar calculation using the vector identity

$$\nabla \times (\nabla \times \vec{H}) = \nabla(\nabla \cdot \vec{H}) - \nabla^2 \vec{H} \quad \text{where} \quad \nabla \cdot \vec{H} = 0$$

yields

$$\nabla^2 \vec{H} + \tilde{\kappa}^2 \vec{H} = 0 \quad . \tag{13}$$

If we define the expression in parenthesis in Equation (12) by a complex dielectric constant, $\tilde{\varepsilon}$, we obtain

$$\tilde{\kappa}^2 = \frac{\omega^2}{c^2} \tilde{\varepsilon}$$

where $\tilde{\varepsilon} = \varepsilon_1 + i\,\varepsilon_2$ and where $\varepsilon_1 = \varepsilon$ and $\varepsilon_2 = \dfrac{4\pi\sigma}{\omega}$.

It is interesting to note that the wave equations (11) and (13) for a conducting medium have exactly the same form as the corresponding equations for a non-conducting medium with the exception that $\tilde{\kappa}$ and $\tilde{\omega}$ are complex instead of real. We shall see later that complex notation enables us to describe many phenomena of conducting media in the often comparatively simpler formalism of non-conducting media.

One solution to Equation (11) is that of a plane, time-harmonic wave

$$\vec{E} = \vec{E}_o \, e^{i(\vec{\kappa}\cdot\vec{r}-\omega t)} \tag{14}$$

where $|\vec{\kappa}|$ is the absolute square root of (12). If we also define the velocity and index of refraction as complex by

$$\tilde{v} = \frac{c}{\sqrt{\tilde{\varepsilon}}} \quad \tilde{n} = \frac{c}{\tilde{v}} = \sqrt{\tilde{\varepsilon}} = \frac{c}{\omega} \tilde{\kappa}$$

and set $\tilde{n} = n + ik$, where n and k are real, we obtain the following relations between ε , n , and k

$$\begin{aligned} \varepsilon_1 &= n^2 - k^2 \\ \varepsilon_2 &= 2\,n\,k \quad . \end{aligned} \tag{15}$$

With these relations, Equation (14) can be written, for a wave propagating in the x-direction, as

$$E = E_o\, e^{i(\frac{n}{c} x - t)} \quad e^{(-\frac{k\omega x}{c})} \quad .$$

This shows that the wave is damped exponentially in the x-direction. The coefficient k is thus called the extinction (or absorption) coefficient and n is the (real) index of refraction. From these relations we see that the phase velocity of the light in the medium is given by c/n and the spatial field amplitude is decreased by the factor

$$e^{-k\omega x/c} \quad .$$

The imaginary part of the dielectric constant, ε_2 ,is associated with energy absorption in the medium as we see from the following discussion. The power loss is given by the real part of

$$P = \vec{J} \cdot \vec{E} \tag{16}$$

and

$$\vec{J} = \frac{\partial \vec{D}}{\partial t} = \frac{\partial}{\partial t} (\varepsilon_1 \vec{E} + i \varepsilon_2 \vec{E}) .$$

If we assume an incident electromagnetic wave having the form

$$\vec{E} = \vec{E}_o e^{i\omega t}$$

we have

$$\vec{J} = (i\omega\varepsilon_1 - \omega\varepsilon_2) \vec{E}$$

and the power loss is

$$\text{Re } P = - \omega|\varepsilon_2||\vec{E}|^2 . \tag{17}$$

Although in this work we do not deal with incident electron excitation, it is nevertheless instructive to see the form of the energy loss function and how it differs from that for electromagnetic radiation. For incident electrons, $\nabla \cdot \vec{D} = 4\pi\rho$, the $\vec{D}$ field arising from the moving electrons. We have

$$\vec{J} = \frac{\partial \vec{D}}{\partial t} = i\omega\vec{D} \tag{18}$$

and

$$P = i\omega \vec{D} \cdot \frac{\vec{D}}{\varepsilon} = \frac{i\omega}{\varepsilon} |\vec{D}|^2$$

and

$$\text{Re } P = \frac{\omega\ \varepsilon_2}{|\varepsilon|^2}\ |\vec{D}|^2 \quad , \quad \text{where} \quad \frac{\varepsilon_2}{|\varepsilon|^2} = \frac{\varepsilon_2}{\varepsilon_1^{\ 2} + \varepsilon_2^{\ 2}} = \text{Im}(\frac{1}{\varepsilon}). \quad (19)$$

It will be subsequently shown in the discussion on the dispersion of surface plasmons that ε_2 is also a measure of the width of the anomalous emission peaks.

The Bulk (Volume) Plasma Frequency

A plasma is a large electrically neutral collection of charged particles possessing opposite signs that shield each other from their Coulomb fields as well as impinging fields. In a metal the plasma consists of the conduction electrons and the lattice ions. Because of charge neutrality there arises a natural resonant frequency, the plasma frequency, that is brought about by displacing the electrons as a group a small distance $\xi(t)$ from the positive ions. Then the charge density $\rho(t)$ which crosses a plane is $\rho = ne\xi$ where n and e are the electron density and charge, respectively. The field arising from this charge density is

$$E = -4\pi\rho = -4\pi\ ne\xi$$

and the equation of motion resulting from this field for a free electron is

$$\frac{d^2\xi}{dt^2} = \frac{e}{m_{eff}}\ E = -\frac{4\pi\ ne^2}{m_{eff}}\ \xi$$

where $m_{eff} = m^* m_o$ is the effective mass of the electron whose (rest) mass is m_o. This is the equation of simple harmonic motion whose resonant (plasma) frequency is

$$\omega_p^2 = \frac{4\pi ne^2}{m_{eff}} .$$

It is called the bulk, or volume, plasma frequency since it applies to an infinite metal without boundaries.

The dielectric properties, as well as ω_p, may be derived in a more general manner for a viscous medium by considering Maxwell's equations [Raether (1965)]. Let us assume that we have a longitudinal (plasma) wave traversing the medium. For longitudinal waves the propagation vector, $\vec{\kappa}$, is parallel to $\vec{E}$, so $\vec{\kappa} \times \vec{E} = 0$, or more generally, $\nabla \times \vec{E} = 0$. But since

$$\nabla \times \vec{E} = \frac{i\omega}{c} \vec{H} , \quad \text{then} \quad \nabla \times \vec{H} = 0 .$$

We have

$$\nabla \times \vec{H} = -\frac{i\omega}{c} \tilde{\varepsilon} \vec{E} , \text{ or } \quad \tilde{\varepsilon} \vec{E} = 0 . \tag{20}$$

Regarding $\vec{E}$ as finite, we have $\tilde{\varepsilon} = 0$ which is the condition for the existence of electrical longitudinal plasma waves.

Now let us consider the equation of motion of a free electron in an oscillating field subjected to viscous damping forces. This equation is, for vibration in the y-direction

$$m_{eff} \frac{\partial^2 y}{\partial t^2} + \frac{m_{eff}}{\tau} \frac{\partial y}{\partial t} + e\, E_y = 0 \tag{21}$$

where τ is the damping constant. A solution to this equation is

$$y = y_o\, e^{-i\omega t}$$

assuming E to vary as

$$\vec{E} = \vec{E}_o\, e^{-i\omega t} \quad .$$

We obtain

$$\omega^2 y + \frac{i\omega}{\tau} y = \frac{e\, E_y}{m_{eff}} \qquad \text{or} \qquad y = \frac{e/m_{eff}}{\omega^2 - \frac{i\omega}{\tau}} E_y \quad . \tag{22}$$

Now, from $\vec{D} = \vec{E} + 4\pi\vec{P}$, we have, taking the time derivative

$$\frac{\partial \vec{D}}{\partial t} = \frac{\partial \vec{E}}{\partial t} + 4\pi \frac{\partial \vec{P}}{\partial t} = \frac{\partial \vec{E}}{\partial t} + 4\pi \vec{J} \tag{23}$$

where J corresponds to a polarization current,

$$J = n\, e\, v = \frac{\partial P}{\partial t} = -\, n\, e \frac{\partial y}{\partial t} \quad . \tag{24}$$

Thus we have for the y-component, using the complex dielectric constant,

$$\tilde{\varepsilon} \frac{\partial E_y}{\partial t} = \frac{\partial E_y}{\partial t} - 4\pi\, n\, e \frac{\partial y}{\partial t}$$

and taking the time derivative of (22)

$$\frac{\partial y}{\partial t} = \frac{e/m_{eff}}{\omega^2 - \frac{i\omega}{\tau}} \quad \frac{\partial E_y}{\partial t}$$

and substituting, we get

$$\tilde{\varepsilon} = 1 - \frac{4\pi n\ e^2/m_{eff}}{\omega^2 - \frac{i\omega}{\tau}} = 1 - \frac{\omega_p^{\ 2}}{\omega^2 - \frac{i\omega}{\tau}} \tag{25}$$

where $\omega_p^{\ 2} = \dfrac{4\pi\ n\ e^2}{m_{eff}}$ = the bulk plasma frequency.

From (25) the real and imaginary parts of $\tilde{\varepsilon}$ are

$$\varepsilon_1 = 1 - \frac{\omega_p^{\ 2}}{\omega^2} \frac{1}{1 + \frac{1}{\omega^2\tau^2}} \tag{26}$$

and

$$\varepsilon_2 = \frac{1}{\omega\tau} \frac{\omega_p^{\ 2}}{\omega^2} \frac{1}{1 + \frac{1}{\omega^2\tau^2}} \quad . \tag{27}$$

Now, if we allow for a complex frequency, i.e., $\omega = \tilde{\omega} = \omega_1 + i\ \omega_2$ and solve (25) for $\tilde{\varepsilon} = 0$, we obtain

$$\omega_1^{\ 2} = \omega_p^{\ 2} - \frac{1}{4\tau^2} \tag{28}$$

and

$$\omega_2 = -\frac{1}{2\tau} \quad . \tag{29}$$

The time dependence, which is of the form $e^{-i\omega t}$ becomes $e^{-i\omega_1 t} e^{-\frac{t}{2\tau}}$ which shows that the wave decays exponentially and thus that ω_2 is a measure of the damping. If the damping (ε_2) is small, that is, if the lifetime τ is large, (26) and (28) become

$$\varepsilon_1 \approx 1 - \frac{\omega_p^2}{\omega^2} \tag{30}$$

$$\omega_1^2 \approx \omega_p^2 \quad . \tag{31}$$

A simple formula has been given by Ferrell (1958) for the broadening of the resonance peak

$$\hbar\gamma = \hbar\, \omega_p\, \varepsilon_2 \tag{32}$$

where γ is the damping rate and $\hbar\gamma$ is the width of the peak at half-maximum. γ is also the reciprocal of τ, i.e., $\gamma = \frac{1}{\tau}$.

Bound Electrons

The previous derivations for the dielectric constant are valid assuming a free electron gas, but are altered if bound electrons in a periodic lattice are considered. In this situation the discrete single-atom energy states are smeared into continua of states called bands because of the degeneracy brought about by the overlapping of the single electron wave functions. Descriptions for the calculation of the

dielectric constant can be made from quantum-mechanical considerations where one sum over a large number of discrete electron excitations. It is assumed that the electrons in a given band ℓ are in Bloch states characterized by a wave vector p. The dielectric constant takes the form [Raether (1965)]

$$\varepsilon(\omega) = 1 - \frac{4\pi e^2}{m_o} \sum_{\ell'} \sum_{m'} \frac{f_{\ell'm'}}{\omega^2 - \omega_{\ell'm'}^2} \tag{33}$$

where the summations are for transitions from all states m' to all unoccupied states ℓ'. It is assumed that damping is small, so that $\varepsilon(\omega) = \varepsilon_1(\omega)$ and that the equation is valid in the long wavelength limit; i.e., for a vanishing wave vector k, where $k = p' - p$. The $f_{\ell'm'}$ are the oscillator strengths for the transitions in question and the $\omega_{\ell'n'}$ characterize the energy difference between two electron states in different bands,

$$\hbar\, \omega_{\ell'm'} = E_{\ell'} - E_{m'} \quad .$$

Let us assume that we have, for example, two energy bands, one an unfilled conduction band c and the other a free band f above it. Equation (33) can be separated into contributions from the interband and the intraband transitions as follows

$$\varepsilon_1(\omega) = 1 - \frac{4\pi e^2}{m_o} \sum_p \frac{f(p',p)}{\omega^2 - \omega_{p'p}^2} - \frac{4\pi e^2}{m_o} \sum_p \frac{f_{fc}(p',p)}{\omega^2 - \omega_{fc}^2}$$

where the second term describes intraband transitions within band c and the third term describes (interband) transitions from band c to band f . In dealing with the second term, one usually has $\omega^2 >> \omega_{pp'}^2$, so that by introducing n , the conduction band electron density, and the effective electron mass, m_{eff} , the summation term can be replaced and the second term becomes

$$\frac{4\pi\, n\, e^2}{m_{eff}\, \omega} = \frac{\omega_p^{\,2}}{\omega} \quad .$$

Thus the intraband transitions are absorbed into an effective plasma frequency. If one assigns a finite lifetime to the electrons excited to the conduction band to account for collisions with phonons, impurities, or other electrons, the dielectric constant takes on a more complicated form. Pines (1963) has shown, in a generalization of the treatment of Lindhard (1954), that these constants can be expressed as

$$\varepsilon_1(\omega) = 1 - \frac{\omega_p^{\,2}}{\omega^2 + \tau^{-2}} - \frac{4\pi\, e^2}{m_o} \sum_{\ell} \frac{f_{\ell\nu}}{\omega^2 - \omega_{\ell\nu}^2} \tag{34}$$

$$\varepsilon_2(\omega) = \frac{\omega_p^{\,2}}{\omega\tau} \frac{1}{\omega^2 + \tau^{-2}} + \frac{2\pi^2\, e^2}{m_o} \sum_{\ell} \frac{f_{\ell\nu}}{\omega_{\ell\nu}} \delta\,(\omega - \omega_{\ell\nu}) \tag{35}$$

where ω_p is the same as that defined in (33) and τ is the relaxation time. Here $f_{\ell\nu}$ is the oscillator strength for a transition from the ground state distribution ν to an excited state ℓ in the different band, and $\delta(\omega - \omega_{\ell\nu})$ is an energy-conserving delta function. Note

that these equations, with the exception of the interband terms in each, are identical in form to Equations (26) and (27) for the free electron gas.

To see how the plasma frequency is shifted by interband transitions, let us assume that the damping is small and apply the condition $\varepsilon_1(\omega) = 0$ to Equation (34). This leads to a plasma frequency

$$\omega_p'^2 = \frac{\omega_p^2}{1 - \delta\,\varepsilon^b}\text{, where}$$

$\delta\,\varepsilon^b = \dfrac{4\pi\, n\, \ell^2}{m_o} \sum \dfrac{f_{\ell\nu}}{\omega^2 - \omega_{\ell\nu}^2}$ and ω_p' is increased if the interband frequency, is less than the plasma frequency ω_p, but decreased if $\omega_{\ell\nu}$ is greater than ω_p. However, if $\omega_{\ell\nu}$ is far away from the plasma frequency, the plasma frequency is changed only slightly and the excitation can still be considered as a free-electron resonance. For example, a metal like Al exhibits free-electron behavior below 1 ev, but because of an interband transition at 1.5 ev, the calculated plasma frequency at 12.7 ev is shifted to 15.2 ev. The situation is more complicated with a metal like Ag, which has a free electron plasma frequency calculated at 9.2 ev, but because of an interband transition at 3.9 ev and possibly others at energies greater than 9.2 ev, the plasma frequency actually falls at 3.75 ev [Raether (1965)].

Surface Plasma Excitations

The foregoing treatment has been concerned with bulk plasma oscillations in infinite crystals. The situation is different for the real case of a bounded crystal. Here we must account for what happens at the interface between two media having different dielectric properties when an electromagnetic disturbance passes from one medium into the other. This analysis is a classical boundary value problem in electromagnetic theory.

Let us assume that we have a semi-infinite conductor of dielectric constant $\tilde{\varepsilon}$, bounded by a vacuum, as in Figure 5a, page 35, and that we seek the solution for an electromagnetic wave propagating along the interface; where, for simplicity we take the propagation vector, κ, along the x-axis. The electric fields must satisfy the wave equations

$$\nabla^2 \vec{E} - \frac{1}{c^2} \frac{\partial^2 \vec{E}}{\partial t^2} = 0 \qquad z > 0 \tag{36}$$

$$\nabla^2 \vec{E} - \frac{\tilde{\varepsilon}}{c^2} \frac{\partial^2 \vec{E}}{\partial t^2} = 0 \qquad z < 0 \ . \tag{37}$$

Retardation effects are automatically accounted for by the time-dependent terms. We find that the solutions to Equations (36) and (37) have the following form

ORNL-DWG 69-7583

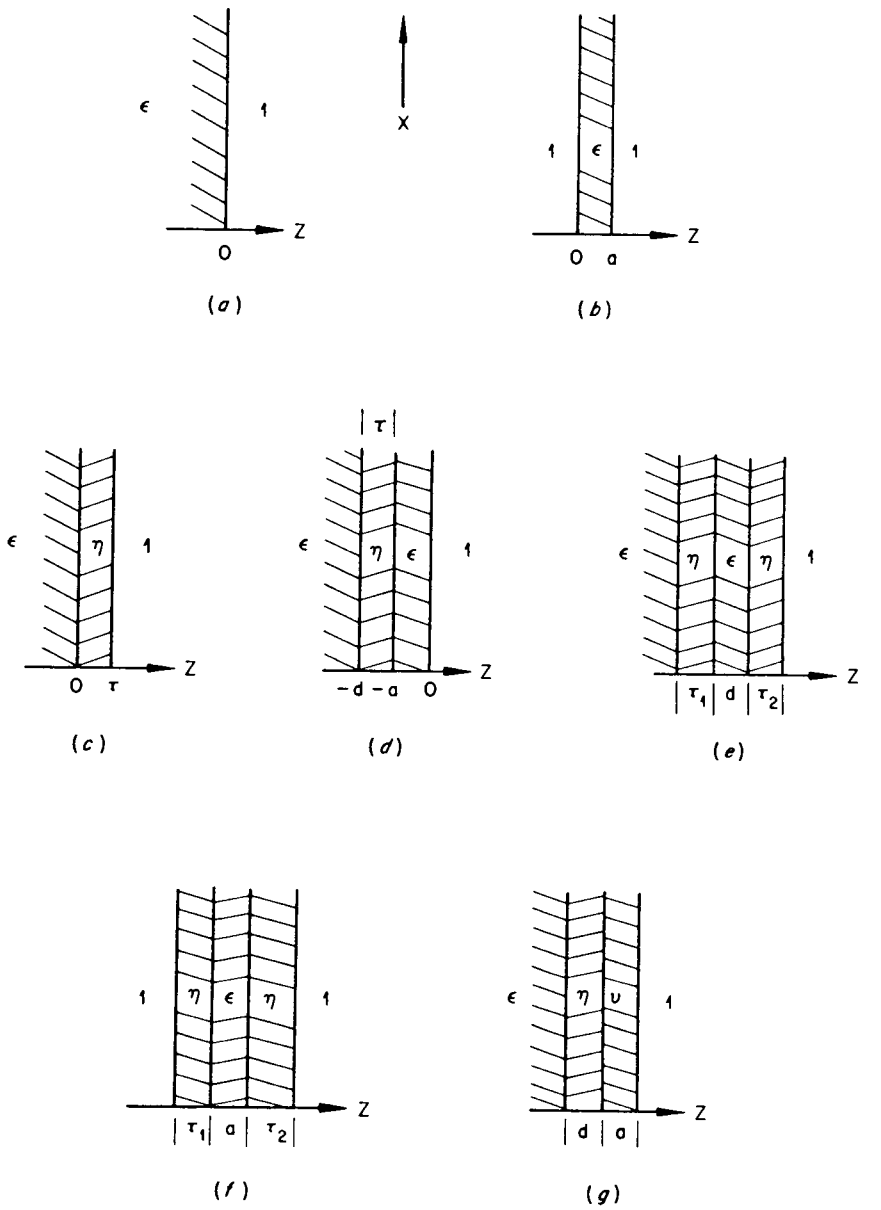

Figure 5. Metal-dielectric configurations: (a) semi-infinite metal-vacuum (b) metal foil bounded by vacuum (c) semi-infinite metal-dielectric-vacuum (d) semi-infinite metal-dielectric-metal-vacuum (e) semi-infinite metal-dielectric-metal-dielectric-vacuum (f) metal foil bounded by uneven dielectric layers and by vacuum (g) semi-infinite metal-dielectric 1-dielectric 2-vacuum.

$$\vec{E} = e^{i(\kappa x - \omega t)} \begin{cases} \vec{A}\ e^{-k_1 z} & z > 0 \\ \vec{B}\ e^{k_2 z} & z < 0 \end{cases} \tag{38}$$

where $\vec{E} = (E_x\ ,\ 0\ ,\ E_z\ )$

$$k_1 = \sqrt{\kappa^2 - \frac{\omega^2}{c^2}} \qquad k_2 = \sqrt{\kappa^2 - \tilde{\varepsilon}\ \frac{\omega^2}{c^2}}\ .$$

Hereafter we shall drop the circumflex over $\tilde{\varepsilon}$, so that $\tilde{\varepsilon} \equiv \varepsilon(\omega) \equiv \varepsilon$. The media, exclusive of the boundary, are homogeneous and charge-free and we may write

$$\nabla \cdot \vec{E} = 0$$

from which we have

$$i\kappa\ A_x - k_1\ A_z = 0 \quad , \qquad i\kappa\ B_x + k_2\ B_z = 0\ . \tag{39}$$

Now since the wave equations (36) and (37) have been cast in the form appropriate for dielectric media, where conduction effects are absorbed into the complex dielectric constant, we need not speak of free charges at the boundary, but only polarization charges. Thus the normal component of the displacement field, $\vec{D}$, is continuous across the boundary, since it is discontinuous only when free charges are present. Using

this and the condition that the tangential component of the electric field is continuous across the boundary, we obtain

$$A_x = B_x$$
$$A_z = \varepsilon B_z \quad . \tag{40}$$

Combining (39) and (40) we can write for the z-components of the field strength

$$k_1 A_z + k_2 B_z = 0$$

$$A_z - \varepsilon B_z = 0 \; .$$

This set of homogeneous equations yields a non-zero solution for the fields if its determinant vanishes, i.e.,

$$\begin{vmatrix} k_1 & k_2 \\ 1 & -\varepsilon \end{vmatrix} = 0$$

and we obtain

$$- k_1 \varepsilon - k_2 = 0 \quad , \text{ or}$$

$$\varepsilon = - \frac{k_2}{k_1} = - \frac{\sqrt{\kappa^2 - \varepsilon \frac{\omega^2}{c_2}}}{\sqrt{\kappa^2 - \frac{\omega^2}{c^2}}}$$

and solving for κ ,

$$\kappa = \frac{\omega}{c} \left(\frac{\varepsilon}{\varepsilon + 1} \right)^{1/2} \tag{41}$$

which is the dispersion relation for the surface wave that we have assumed to be propagating at the interface. This equation has been obtained by other investigators using different methods [Teng and Stern (1967b), Ritchie and Eldridge (1962)]. We see from Equation (38) that the field has a component parallel to the direction of motion and another one transverse to this direction. This is characteristic of a transverse magnetic (TM) electromagnetic wave. Because the z-dependence is exponentially decaying away from the interface the wave is bound to this interface. Thus we may think of the wave as being a bound surface wave, with the surface acting as a waveguide. Other modes such as the transverse electric (TE) and transverse electromagnetic (TEM) waves do not yield non-singular solutions, so the TM wave is the only type that can exist in this situation. This TM mode is the same as the one postulated by Sommerfeld for a wave propagating at an earth-air interface and it is also known as the Sommerfeld surface wave.

If we assign a value of unity to A_x and B_x , the following fields are obtained, using Equations (39) and (8)

$$\vec{E} = \vec{E}_o \, e^{i(\kappa x - \omega t)} \begin{cases} (1, 0, \frac{i\kappa}{k_1}) \, e^{-k_1 z} & z > 0 \\ (1, 0, -\frac{i\kappa}{k_2}) \, e^{k_2 z} & z < 0 \end{cases} \tag{42}$$

$$\vec{H} = \frac{i\omega}{c}\vec{E}_o \; e^{i(\kappa x-\omega t)} \begin{cases} (0, -\frac{1}{k_1}, 0)\; e^{-k_1 z} & z > 0 \\ (0, \frac{\varepsilon}{k_2}, 0)\; e^{k_2 z} & z < 0 \end{cases} .$$

It is interesting to see the form of the charge density at the surface. We can obtain this from Equation (42) and the divergence equation in $\vec{E}$,

$$\begin{aligned} \nabla \cdot \vec{E} &= 0 \qquad z > 0 \text{ and } z < 0 \\ \nabla \cdot \vec{E} &= 4\pi\rho \qquad z = 0 \; . \end{aligned} \tag{43}$$

At $z = 0$, Equation (42) in $\vec{E}$ is

$$\vec{E} = \vec{E}_o \; e^{i(\kappa x-\omega t)} \begin{cases} (1, 0, \frac{i\kappa}{k_1}) & z|_{o+} \\ (1, 0, -\frac{i\kappa}{k_2}) & z|_{o-} \end{cases}$$

and application of Equation (43) gives

$$\rho = \frac{i\kappa}{4\pi} \; E_o \; e^{i(\kappa x-\omega t)} \; \delta\,(z) \; . \tag{44}$$

This tells us that there is a longitudinal charge wave, propagating in the direction of the surface wave (and $\pi/2$ out of phase with it). Since in the formalism used here we are not considering free charge, this represents a polarization surface charge wave. It is this charge wave,

propagating in the conduction electron plasma of the metal, that leads us to also call it a surface plasma wave. Thus the alternate descriptions that have been considered up to now for this wave, such as the TM wave, Sommerfeld wave, surface charge wave, and surface plasma wave, all describe the same phenomenon. When this wave is quantized, it is also called a surface plasmon.

Let us now consider the the conditions on the dielectric constant that permit the surface wave to exist. Assuming an essentially free electron plasma with small damping, we have $\varepsilon_1 = 1 - \frac{\omega_p^2}{\omega^2}$ [Equation (30)], which for a metal is typically negative for $\omega < \omega_p$. The square root tern in Equation (41) represents the deviation of the propagation vector from the light line, $\kappa = \frac{\omega}{c}$, i.e., it tells us how fast the wave is moving with respect to the free space velocity of light. Since ε_1 is negative κ always lies to the right of the light line, that is, the surface wave propagates at less than the speed of light. In the limit of an infinitely large k vector, we see from Equation (41) that $\varepsilon_1 = -1$. ε_1 cannot be greater than -1 because (41) would become imaginary. Substituting into (30), we find $\omega = \frac{\omega_p}{\sqrt{2}}$ which is called the surface plasma frequency. This is in agreement with Ritchie's result.

Wave Damping

Following Teng's analysis (1967) we can express the dispersion relation, Equation (41) as

$$\frac{\omega}{\kappa c} = \left(\frac{\varepsilon + 1}{\varepsilon}\right)^{1/2} = \left(1 + \frac{1}{\varepsilon}\right)^{1/2} .$$

If we allow ω and ε to be complex, i.e., $\omega = \omega_1 + i\,\omega_2$ and $\varepsilon = \varepsilon_1 + i\,\varepsilon_2$ and κ be real, we can solve for the half-width of the peak, which is given as $2\omega_2$. Near the light line, $\omega_1 \approx c\kappa$, so

$$\frac{\omega}{\omega_1} \simeq 1 + \frac{1}{2\varepsilon} \qquad \text{where} \quad |\varepsilon| >> 1 .$$

Solving for the imaginary part only, we obtain

$$\frac{2\,\omega_2}{\omega_1} = \frac{\Delta\omega}{\omega} = \frac{\varepsilon_2}{\varepsilon_1^{\,2} + \varepsilon_2^{\,2}} \tag{45}$$

This is seen to be of the same form as that for the energy loss function, Equation (19). For Al, Au, and Ag, ε_2 increases with frequency greater than does ε_1 up to ω_p and the result is greater damping at the higher frequencies. This is in agreement with the experimental results.

This treatment is for electronic damping only, and does not include radiative damping. Radiative damping is considered later in the section dealing with quantum mechanical transition rates.

Thin Foil Bounded by Vacuum

If we now consider a thin metal foil of thickness a , bounded on both sides by vacuum, as in Figure 5b, page 35, a different situation develops. Now the equations for the electric field become

$$\vec{E} = e^{i(\kappa x-\omega t)} \begin{cases} \vec{A}\ e^{-k_1 z} & z > a \\ \vec{B}\ e^{-k_2 z} + \vec{C}\ e^{k_2 z} & 0 \leq z \leq a \\ \vec{D}\ e^{k_1 z} & z < 0 \end{cases} \tag{46}$$

where k_1 and k_2 have the same value as in Equation (38). Using the same method of analysis as before (see Appendix A), we obtain the following dispersion relation

$$\varepsilon^2 + 2\varepsilon \frac{k_2}{k_1} \coth (k_2 a) + \frac{k_2^2}{k_1^2} = 0 \quad .$$

Solving for ε we obtain

$$\varepsilon = -\frac{k_2}{k_1} \begin{cases} \tanh k_2 \frac{a}{2} \\ \coth k_2 \frac{a}{2} \end{cases} \quad . \tag{47}$$

This solution represents two plasma waves that propagate on each surface of the foil. For the lower (symmetric) solution these waves are in phase, and for the upper (antisymmetric) solution the waves are a half-wavelength out of phase. These modes are referred to as the tangential and normal modes, respectively, because in the former the electronic motion is predominately parallel to the foil surface, and in the latter it is perpendicular to it. For a thick foil the modes become decoupled. All three modes are illustrated in Figure 3, page 10. Equation (47) has been obtained in a slightly different form by Ritchie and Eldridge (1962):

$$k_1\varepsilon + k_2 = \pm (k_1\varepsilon - k_2)\, e^{-k_2 a} \tag{48}$$

where the plus and minus signs are for the normal and tangential modes, respectively. If retardation is neglected, we assume that $\kappa^2 >> \omega^2/c^2$, or in effect that the speed of light, c, is infinite. This means that instead of satisfying the wave equations (36) and (37), we need only satisfy the Laplacian, $\nabla^2 \vec{E} = 0$. We have $k_1 \to \kappa$ and $k_2 \to \kappa$, so that (47) and (48) become

$$\varepsilon = - \begin{cases} \tanh \kappa \dfrac{a}{2} \\ \\ \coth \kappa \dfrac{a}{2} \end{cases} \tag{49}$$

and

$$\varepsilon + 1 = \pm (\varepsilon - 1)\, e^{-\kappa a} \quad .$$

In the non-retarded solution the normal mode dispersion curve starts at the plasma frequency for vanishing κ and asymptotically approaches the line $\omega = \omega_p/\sqrt{2}$ for $\kappa \to \infty$. The tangential mode curve also approaches $\omega = \omega_p/\sqrt{2}$ for large κ but begins at $\omega = 0$ for vanishing κ (Figure 2, page 10). The asymptotic solution becomes clear when we realize that for large κ, $\varepsilon = -1$, and substitution into (30) gives $\omega = \omega_p/\sqrt{2}$. Equations (49) have been obtained earlier by Ferrell (1958) and Ritchie (1957). The effect of retardation is to split the normal mode dispersion curve into two branches, one starting at the plasma frequency and decreasing until it nears the light line and then

asymptotically approaching and remaining to the left of the light line as $\omega \to 0$. The other branch starts at $\omega = 0$ on the right of the light line, rises sharply above the line $\omega_p/\sqrt{2}$ and then asymptotically approaches $\omega_p/\sqrt{2}$ for large κ. The retarded tangential mode curve is shifted slightly from the non-retarded curve, remaining always to the right of the light line. Some typical curves are shown in Figure 4, page 12. Those dispersion curves lying to the right of the light line indicate phase velocities less than the speed of light and those modes are referred to as non-radiative modes. This is because energy and momentum cannot be simultaneously conserved at the boundary, so the plasma waves cannot be stimulated by or decay into electromagnetic radiation in free space. However, if the surface is not smooth the momentum restriction is relaxed, so in fact these surface waves can be excited in this way, as will be pointed out in the next section. As the thickness of the foil is increased, the two non-radiative modes get closer together until they become degenerate.

The dispersion curve lying to the left of the light line is called the radiative mode because its phase velocity is always greater than light and can thus couple directly to the free-space electromagnetic field. Equation (47) in its present form does not describe this mode because it applies to a bound surface wave. In a rather extensive analysis of the radiation modes, Kliewer and Fuchs (1967) pointed out that those must be regarded as virtual modes, described by the following equations

$$\varepsilon = \frac{k_2'}{k_1'} \begin{cases} i \tan k_2' a \\ -i \cot k_2' a \end{cases} \tag{48a}$$

where

$$k_1' = \sqrt{\frac{\omega^2}{c^2} - \kappa^2} = i\, k_1$$

$$k_2' = \sqrt{\varepsilon \frac{\omega^2}{c^2} - \kappa^2} = i\, k_2 \quad . \tag{48b}$$

It can be seen that Equation (48a) results naturally when the transformation (48b) extending to the left of the light line is applied to Equation (47). This no longer describes a bound wave, since the coefficients k_1' and k_2' when substituted into (45) give a sinesoidal instead of an exponential dependence. To insure proper behavior of the wave at infinity, a complex frequency is used which allows for a temporal decay of the radiating wave. In addition, the dielectric constant, ε , and the wave vector, κ, are made complex. So the frequency axis as shown in Figure 4, page 12, represents, for the radiative mode, only the real part of the frequency. The branch of the radiative mode shown in this curve is for a very thin foil and only for the lowest order excitation. In contrast to the non-radiative modes, the radiative modes can have multiple excitations, corresponding to the cyclic arguments of the tangent and cotangent functions, that can appear at frequencies larger

than the plasma frequency. As the thickness is increased these modes get closer together, but they can approach the light line asymptotically toward infinity instead of zero.

Dielectric on a Semi-Infinite Metal Substrate

The surface plasma frequency, it was found, appears at a value reduced from the volume plasma frequency by a factor $1/\sqrt{2}$. This reduction is due to the depolarizing effect of the vacuum at the boundary between the metal and the vacuum. If we now consider the effect of a dielectric layer between the metal and vacuum, the surface frequencies are further reduced, because the dielectric exerts an even stronger depolarizing effect. This effect, which was predicted theoretically and demonstrated experimentally many times for higher energy excitations is extended in this section to the long wavelength excitation region.

Let us assume a dielectric layer of thickness τ and dielectric constant $\eta = \eta(\omega) = \eta_1 + i\,\eta_2$ extending infinitely in the x-y plane and bounded by a semi-infinite metal slab on one side and vacuum on the other, as shown in Figure 5c, page 35. The electric fields for the surface plasma wave have the following form

$$\vec{E} = e^{i(\kappa x-\omega t)} \begin{cases} \vec{A}\, e^{-k_1 z} & z > \tau \\ \vec{B}\, e^{-k_2 z} + \vec{C}\, e^{k_2 z} & 0 \leq z \leq \tau \\ \vec{D}\, e^{k_3 z} & z < 0 \end{cases} \tag{49}$$

where

$$k_1 = \sqrt{\kappa^2 - \frac{\omega^2}{c^2}} \qquad k_2 = \sqrt{\kappa^2 - \eta\,\frac{\omega^2}{c^2}} \qquad k_3 = \sqrt{\kappa^2 - \varepsilon\,\frac{\omega^2}{c^2}}\ .$$

Using the same method of solution as before (see Appendix A), the following dispersion relation is obtained

$$\varepsilon = -\eta\,\frac{k_3}{k_2}\,\frac{1 - \gamma'\,e^{-2k_2\tau}}{1 + \gamma'\,e^{-2k_2\tau}} \tag{50}$$

where

$$\gamma' = \frac{\eta\,k_1 - k_2}{\eta\,k_1 + k_2}\ .$$

If retardation is neglected, k_1 , k_2 , and k_3 all approach κ , so that we have

$$\varepsilon = -\,\eta\,\frac{1 - \gamma\,e^{-2\kappa\tau}}{1 - \gamma\,e^{-2\kappa\tau}} \quad \text{where} \quad \gamma = \frac{\eta - 1}{\eta + 1}\ . \tag{51}$$

This is the result that was obtained earlier by Stern and Ferrell (1960). One sees that for either an infinite thickness of dielectric or an infinite κ , Equation (51) becomes

$$\varepsilon = -\,\eta$$

and this, substituted into Equation (30) gives

$$\omega = \frac{\omega_p}{\sqrt{1 + \eta}} \quad .$$

This is the reduced surface plasma frequency. If the dielectric layer is replaced by vacuum, we have $\eta = 1$, so that we arrive at our previous result for the surface plasma frequency,

$$\omega = \omega_p / \sqrt{2} \quad .$$

One encounters some difficulty with the retarded solution, Equation (50), in the long wavelength range because k_2 can become imaginary. We are considering now only the non-radiative plasma wave. This is because for many dielectrics the imaginary part of η is zero and the real part of η is positive in this range, so that for points on the dispersion curve near the light line, $\eta\, \omega^2/c^2 > \kappa^2$. This difficulty is not encountered with k_3 , because for metals the real part of ε is negative and the imaginary part is small. Equation (50) can also be expressed in the following form

$$\varepsilon = -\eta \frac{k_3}{k_2} \frac{\eta\, k_1 \tanh k_2\tau + k_2}{\eta\, k_1 + k_2 \tanh k_2\tau} \quad . \tag{52}$$

If we make the substitution $k_2 \to i\, k_2'$ where $k_2' = \sqrt{\eta\omega^2/c^2 - \kappa^2}$, Equation (52) becomes

$$\varepsilon = -\eta \frac{k_3}{k_2'} \frac{\eta\, k_1 \tan k_2'\tau + k_2'}{\eta\, k_1 - k_2' \tan k_2'\tau} \quad . \tag{53}$$

Equation (53) allows us to extend the dispersion curve as close to the light line as we wish since the imaginary term has been eliminated, which is the interesting part of the above transformation. This means that there is no additional absorptive mechanism introduced by the transformation. The form of k_2' shows that the exponential decay of the surface wave away from the metal surface is replaced by an oscillatory decay. Also, if $\eta\,\omega^2/c^2 > \kappa^2$ the phase velocity of the surface wave is greater than that of light in the dielectric, i.e.,

$$\sqrt{\eta}\,\frac{\omega}{c} > \kappa \quad \text{which leads to } v > \frac{c}{\sqrt{\eta}} \qquad \text{where}$$

$$\frac{c}{\sqrt{\eta}} \quad = \text{speed of light in dielectric}$$

and this corresponds to a radiating wave. But this is only true within the dielectric, and beyond the vacuum-dielectric interface, the wave amplitude again decays exponentially. Thus we may consider the surface wave here as being confined between the metal and vacuum. For the case $\kappa^2 > \eta\,\omega^2/c^2$ the wave is also confined between the metal and vacuum, but the phase velocity in the dielectric is always less than light.

For an infinitely thick dielectric layer, Equation (50) becomes

$$\varepsilon = -\eta\,\frac{k_3}{k_2} = -\eta\,\frac{\sqrt{\kappa^2 - \varepsilon\,\frac{\omega^2}{c^2}}}{\sqrt{\kappa^2 - \eta\,\frac{\omega^2}{c^2}}} \quad \text{and solving for } \kappa$$

we obtain

$$\kappa = \frac{\omega}{c} \left(\frac{\varepsilon \eta}{\varepsilon + \eta} \right)^{1/2} . \tag{54}$$

Metal Layer on a Dielectric-Coated Metal Layer

An extension of the above case that was encountered in this work was the coating of a metal layer over a dielectric-coated metal layer, where both metals are the same as shown in Figure 5d, page 35. The equations for the electric fields are as follows

$$\vec{E} = e^{i(\kappa x - \omega t)} \begin{cases} \vec{A}\, e^{-k_1 z} & z > 0 \\ \vec{B}\, e^{-k_2 z} + \vec{C}\, e^{k_2 z} & -a < z < 0 \\ \vec{D}\, e^{-k_3 z} + \vec{E}\, e^{k_3 z} & -d < z < -a \\ \vec{F}\, e^{k_2 z} & z < -d \end{cases} \tag{55}$$

$$k_1 = \sqrt{\kappa^2 - \frac{\omega^2}{c^2}} \qquad k_2 = \sqrt{\kappa^2 - \varepsilon \frac{\omega^2}{c^2}} \qquad k_3 = \sqrt{\kappa^2 - \eta \frac{\omega^2}{c^2}}$$

and ε and η are the dielectric constants for the metal and dielectric, respectively. The following dispersion relations were obtained

$$\tanh k_3 \tau = \frac{2\eta\, \varepsilon\, k_2\, k_3\, (\varepsilon\, k_1 + k_2)}{(\varepsilon^3 k_1 k_3^2 + \eta^2 k_2^3)(e^{-2k_2 a} - 1) - \varepsilon k_2 (\eta^2 k_1 k_2 + \varepsilon k_3^2)(1 + e^{-2k_2 a})} \tag{56}$$

for $$k_3 = \sqrt{\kappa^2 - \eta \frac{\omega^2}{c^2}}$$

and

$$\tan k_3'\tau = \frac{2\eta\ \varepsilon\ k_2\ k_3'\ (\varepsilon\ k_1 + k_2)}{(-\varepsilon^3 k_1 k_3'^2 + \eta^2 k_2^3)(e^{-2k_2 a} - 1) - \varepsilon k_2(\eta^2 k_1 k_2 - \varepsilon k_3'^2)(1 + e^{-2k_2 a})} \quad (57)$$

for $k_3 \to i\ k_3'$ where $k_3' = \sqrt{\eta \frac{\omega^2}{c^2} - \kappa^2}$

and where a is the overcoating thickness of the metal layer and τ is the thickness of the dielectric layer. Equations (56) and (57) approximate the case of a thin metal foil, except that here we have vacuum on one side and a dielectric-metal layer on the other.

Dielectric-Coated Metal Layer on a Second Dielectric-Coated Metal Layer

The situation encountered in actual practice was to coat Al over an Al_2O_3-coated Al substrate. The top Al coating then oxidized naturally. So in the real case one has a vacuum dielectric-metal-dielectric-metal multilayer as shown in Figure 5e, page 35. The dispersion relation could be obtained by continued application of the method used previously of setting up electric fields for each boundary and expanding the resulting determinant, but for more than three boundaries this becomes quite tedious. An alternate method, especially applicable to multilayers, was developed by Shieh (1968) and involves only 2 x 2 matrices of the recursive type. Through rigorous examination of the boundary and continuity relations for the electric and magnetic fields, Shieh (1968a)

was able to show that the dispersion relation could be obtained by expansion of the matrix equation (see Appendix B)

$$(b_o\, e^{-k_1 d_1} \quad a_o\, e^{k_1 d_1}) \prod_{p=1}^{n-1} M_p \begin{pmatrix} \varepsilon_{n+1}\, k_n - \varepsilon_n\, k_{n+1} \\ \varepsilon_{n+1}\, k_n + \varepsilon_n\, k_{n+1} \end{pmatrix} = 0 \qquad (58)$$

where

$$M_p = \begin{pmatrix} a_p\, e^{-k_{p+1}\, d_{p+1}} & b_p\, e^{k_{p+1}\, d_{p+1}} \\ b_p\, e^{-k_{p+1}\, d_{p+1}} & a_p\, e^{k_{p+1}\, d_{p+1}} \end{pmatrix}$$

and

$$a_p = \varepsilon_{p+1}\, k_p + \varepsilon_p\, k_{p+1} \qquad b_p = \varepsilon_{p+1}\, k_p - \varepsilon_p\, k_{p+1} \quad .$$

Here we are considering n layers with $n+1$ interfaces, and the pth layer has a thickness d_p and a dielectric constant ε_p. Thus for the three layer case, $n = 3$ and p ranges from 1 to 2. The resulting dispersion equation is

$$\begin{aligned} \exp(-2k_2 d) = \{&(A+H)\cosh k_1\tau_1 \sinh k_1\tau_2 + (D+E)\sinh k_1\tau_1 \sinh k_1\tau_2 \\ &+ (B+G)\cosh k_1\tau_1 \cosh k_1\tau_2 + (C+F)\sinh k_1\tau_1 \cosh k_1\tau_2 \\ &+ (B+G)\cosh(k_1\tau_1 + k_1\tau_2) + (C+F)\sinh(k_1\tau_1 + k_1\tau_2)\} \qquad (59) \\ \div \{&(A+H)\cosh k_1\tau_1 \sinh k_1\tau_2 + (D+E)\sinh k_1\tau_1 \sinh k_1\tau_2 \\ &- (B+G)\sinh k_1\tau_1 \sinh k_1\tau_2 - (C+F)\cosh k_1\tau_1 \sinh k_1\tau_2\} \end{aligned}$$

where

$$k_0 = \sqrt{\kappa^2 - \frac{\omega^2}{c^2}} \qquad k_1 = \sqrt{\kappa^2 - \eta\,\frac{\omega^2}{c^2}} \qquad k_2 = \sqrt{\kappa^2 - \varepsilon\,\frac{\omega^2}{c^2}}$$

and

$$A = \eta\,\varepsilon^3\,k_o\,k_1^{\,3} \qquad E = \varepsilon^3\,k_1^{\,4}$$

$$B = \eta^2\,\varepsilon^2\,k_o\,k_1^{\,2}\,k_2 \qquad F = \eta\,\varepsilon^2\,k_1^{\,3}\,k_2$$

$$C = \eta^3\,\varepsilon\,k_o\,k_1\,k_2^{\,2} \qquad G = \eta^2\,\varepsilon\,k_1^{\,2}\,k_2^{\,2}$$

$$D = \eta^4\,k_o\,k_2^{\,3} \qquad H = \eta^3\,k_1\,k_2^{\,3}$$

where

τ_1 = thickness of the dielectric layer next to the substrate

τ_2 = thickness of the dielectric layer next to vacuum

d = thickness of the metal overcoating layer

$\eta = \eta(\omega)$ = dielectric constant of the dielectric

$\varepsilon = \varepsilon(\omega)$ = dielectric constant of the metal

For values near the light line, $k_1 \to i\,k_1'$ where $k_1' = \sqrt{\eta\,\omega^2/c^2 - \kappa^2}$ and Equation (59) is transformed into

$$\begin{aligned}\exp(-2k_2 d) = \{&(A-H)\cos k_1'\tau_1 \sin k_1'\tau_2 - (D+E)\sin k_1'\tau_1 \sin k_1'\tau_2 \\ &- (B+G)\cos k_1'\tau_1 \cos k_1'\tau_2 - (C-F)\sin k_1'\tau_1 \cos k_1'\tau_2 \\ &- (B+G)\cos(k_1'\tau_1 + k_1'\tau_2) - (C-F)\sin(k_1'\tau_1 + k_1'\tau_2)\} \\ \div \{&(A-H)\cos k_1'\tau_1 \sin k_1'\tau_2 - (D+E)\sin k_1'\tau_1 \sin k_1'\tau_2 \\ &- (B+G)\sin k_1'\tau_1 \sin k_1'\tau_2 + (C-F)\cos k_1'\tau_1 \sin k_1'\tau_2\}\end{aligned} \tag{60}$$

where k_1 in terms A through H is replaced by k_1'. We note that here, as well as with the single dielectric layer [Equation (57)], the dispersion relation near the light line comes out to be real, (if only real parameters are used). And as with Equations (56) and (57) both normal and tangential modes are excited, except that the modes on the outer dielectric interface are relaxed from their vacuum-interface values.

We now consider a thin metal foil bounded on either side by unequal thicknesses of dielectric. This configuration, shown in Figure 5f, page 35, when analyzed by the previous methods yields

$$\varepsilon^2 + \varepsilon\eta \coth (k_2 a) \left[F'(k_3 \tau_1) + F'(k_3 \tau_2)\right]$$

$$+ \eta^2 \frac{k_2^2}{k_3^2} F'(k_3 \tau_1) F'(k_3 \tau_2) = 0 \qquad (61)$$

where

$$F'(x) = \frac{1 - \gamma' e^{-2x}}{1 + \gamma' e^{-2x}} \qquad \gamma' = \frac{\eta k_1 - k_3}{\eta k_1 + k_3}$$

and

$$k_1 = \sqrt{\kappa^2 - \frac{\omega^2}{c^2}} \qquad k_2 = \sqrt{\kappa^2 - \varepsilon\frac{\omega^2}{c^2}} \qquad k_3 = \sqrt{\kappa^2 - \eta\frac{\omega^2}{c^2}}$$

and ε and η have the same meaning as before. The thicknesses of the metal foil and the dielectric layers are a and τ, respectively. Near the light line, where $k_3 \to i\, k_3'$, we have

$$\varepsilon^2 + \varepsilon\eta \coth (k_2 a) [F' (k_3' \tau_1) + F' (k_3' \tau_2)]$$

$$- \eta^2 \frac{k_2^2}{k_3'^2} F' (k_3' \tau_1) F' (k_3' \tau_2) = 0 \qquad (62)$$

where

$$F' (k_3' \tau) = \frac{\eta k_1 \tan k_3' \tau + k_3'}{\eta k_1 - k_3' \tan k_3' \tau}$$

and

$$k_3' = \sqrt{\eta \frac{\omega^2}{c^2} - \kappa^2} \quad .$$

Metal Substrate Coated with a Double Dielectric Layer

The situation often encountered in this work was that of a contaminant, such as diffusion pump oil, adhering to the surface of a dielectric-coated metal substrate, such as Al_2O_3 on Al. In this case, the dispersion properties of the surface plasma waves are affected not only by one but by two dielectric layers, each having a different dielectric constant. This configuration, as shown in Figure 5g, page 35, was analyzed by the method of Equation (58) and the following dispersion relation was obtained

$$\tanh k_1 a = \frac{-(A+H) - (D+ E) \tanh k_2 d}{(C+F) + (B+G) \tanh k_2 d} \qquad (63)$$

where

a = thickness of dielectric adjacent to vacuum [with dielectric constant $\nu = \nu(\omega)$]

d = thickness of dielectric adjacent to metal substrate [with dielectric constant $\eta = \eta(\omega)$]

$$A = \eta\nu\varepsilon\, k_o\, k_1\, k_2 \qquad E = \eta^2\nu\, k_o\, k_1\, k_3 \qquad k_o = \sqrt{\kappa^2 - \frac{\omega^2}{c^2}}$$

$$B = \nu^2\varepsilon\, k_o\, k_2^2 \qquad F = \nu^2\eta\, k_o\, k_2\, k_3 \qquad k_1 = \sqrt{\kappa^2 - \nu\frac{\omega^2}{c^2}}$$

$$C = \eta\varepsilon\, k_1^2\, k_2 \qquad G = \eta^2\, k_1^2\, k_3 \qquad k_2 = \sqrt{\kappa^2 - \eta\frac{\omega^2}{c^2}}$$

$$D = \nu\,\varepsilon\, k_1\, k_2^2 \qquad H = \nu\,\eta\, k_1\, k_2\, k_3 \qquad k_3 = \sqrt{\kappa^2 - \varepsilon\frac{\omega^2}{c^2}}$$

$\varepsilon = \varepsilon(\omega)$ = dielectric constant of metal substrate

When Equation (63) is extended close to the light line, either one or both of the values k_1 or k_2 can become imaginary, so that three other forms of this equation are obtained:

$$\tan k_1' a = \frac{(A + H) - (D - E)\tan k_2' d}{(C - F) + (B + G)\tan k_2' d} \tag{64}$$

where

$$k_1 \to i\, k_1' \qquad k_2 \to i\, k_2' \qquad k_1' = \sqrt{\nu\frac{\omega^2}{c^2} - \kappa^2}$$

$$k_2' = \sqrt{\eta\frac{\omega^2}{c^2} - \kappa^2}$$

$$\tan k_1' a = \frac{-(A + H) - (D + E) \tanh k_2 d}{(-C + F) + (B - G) \tanh k_2 d} \quad k_1 \to i k_1' \tag{65}$$

$$\tanh k_1 a = \frac{-(A + H) + (D - E) \tan k_2' d}{(C + F) + (-B + G) \tan k_2' d} \quad k_2 \to i k_2' . \tag{66}$$

In quantities A through H in these equations, k_1 and k_2 are replaced by k_1' and k_2' where appropriate. Note that here again all the dispersion equations come out to be real (assuming one uses real parameters).

III. QUANTUM MECHANICAL CONSIDERATIONS

The previous calculations have been concerned with the properties of surface plasma waves, as derived from Maxwell's equations, under different boundary conditions. These dispersion relations describe the propagation of the surface waves but do not say anything about how such waves are excited. Previous classical electromagnetic theories, such as those of Fano (1941) and Hessel and Oliner (1965) show that the surface waves can be produced by resonant excitation. Their analyses,which were applied to grating surfaces, showed that coupling between the incident free-space electromagnetic waves and the surface waves was made possible because of the periodic roughness of the grating structure. What we wish to do in this section is to show how the excitation of the non-radiative surface waves can be described quantum-mechanically in a second-order interaction between the quantized photon

and plasmon fields, and how this leads to a description of the intensities involved. We shall also discuss the radiative mode excitation of a first order coupling between the photon and plasmon fields and the intensities for the thin foil (non-retarded) case.

Volume and Surface Plasmons

We have previously derived the volume (bulk) plasma frequency, ω_p , as the frequency at which collective oscillations of the electron gas of the metal occur, and that the energy of the plasmon was given by

$$E = \hbar\,\omega_p = \hbar\left(\frac{4\pi\, ne^2}{m_{eff}}\right)^{1/2} .$$

We showed also that the surface plasmon energy is given by

$$E = \hbar\,\omega_p = \hbar\,\frac{\omega_p}{\sqrt{2}}$$

for the pure metal in the limit of large κ . However, we have seen that surface plasmons can occur at many energies depending on the surface plasmon dispersion, where the frequencies are those of the surface plasma waves.

In the discussion to follow we shall refer to the "photon," "plasmon," and "surface plasmon" as the quanta of the elementary excitations of the quantized electromagnetic field, the volume plasma field, and the surface plasma field, respectively.

The Quantum Hydrodynamical Model

A method of treating in a quantum-mechanical way the interactions between electromagnetic and particle radiation and the electron plasma of a metal is the quantum hydrodynamical model first used by Bloch (1933, 1934). This model was extended by Ritchie (1957) to an investigation of the surface modes and by Wilems and Ritchie (1967, 1968) and Ritchie and Wilems (1969) to studies of non-linear interactions in quantum plasmas. This model is appropriate because field perturbation techniques can be easily used, and the resonances of the atomic system are emphasized. Non-linear effects can also be treated easily since the hydrodynamical equations themselves are nonlinear.

The total Hamiltonian of the system is obtained in the usual way from a Lagrangian which yields the hydrodynamical equations of motion. This Hamiltonian is divided into parts corresponding to the non-interacting fields, which for our case are the radiation and plasma fields, and terms describing the interaction between them. The radiation and plasma fields are then quantized into the photon and plasmon fields, and the interaction terms are described utilizing the potential operators of each quantized field. When the equations of motion are obtained, they are linearized in the standard way so that they may be treated analytically.

The linearized hydrodynamical (Bloch) equations found by the procedure above for an electron gas have been obtained by Wilems and Ritchie and are given below (in 1st order)

$$\frac{\partial \psi_1}{\partial t} = - \frac{e}{m} \phi_1 + \frac{\beta^2}{n_o} n_1 \tag{67}$$

$$\nabla^2 \phi_1 = 4\pi e \, n_1$$

$$\frac{\partial n_1}{\partial t} = \nabla \cdot [n_o \nabla \psi_1]$$

$$[\nabla^2 - \frac{1}{c^2} (\frac{\partial^2}{\partial t^2} + \omega_p{}^2)] \vec{A}_1 = \frac{1}{c} \nabla \frac{\partial \phi_1}{\partial t} - \frac{4\pi e \, n_o}{c} \nabla \psi_1$$

where one assumes that the electronic density, the electromagnetic scalar potential, the plasma velocity potential and the vector potential may be expanded as

$$n(\vec{r}, t) = n_o (\vec{r}) + n_1 (\vec{r}, t) + n_2 (\vec{r}, t) + \ldots \tag{68}$$

$$\phi(\vec{r}, t) = \phi_o(\vec{r}) + \phi_1(\vec{r}, t) + \ldots$$

$$\psi(\vec{r}, t) = \psi_1(\vec{r}, t) + \psi_2(\vec{r}, t) + \ldots$$

$$\vec{A}(\vec{r}, t) = \vec{A}_1 (\vec{r}, t) + \vec{A}_2 (\vec{r}, t) + \ldots$$

$\beta = v_f/\sqrt{3}$ is the hydrodynamic velocity, where v_f is the Fermi velocity.

The total Hamiltonian for the electron gas is

$$H = H_R + H_P + H_{RP} \tag{69}$$

where the subscripts refer to the radiation, plasmon, and interaction terms, respectively. The energy, H_R , of the radiation field is given as

$$H_R = \frac{1}{8\pi c^2} \int [(\frac{\partial \vec{A}}{\partial t})^2 + c^2 (\nabla \times \vec{A})^2] \, d\tau \tag{70}$$

and that of the plasmon field, H_P , as

$$H_P = \int [\frac{m}{2} n_o (\nabla\psi_1 - \frac{e}{mc} \vec{A}_1)^2 - \frac{e}{2} n_1 \phi_1 + \frac{m}{2n_o} \beta^2 n_1] \, d\tau \quad . \tag{71}$$

When retardation is neglected, the term $(e/mc) \vec{A}_1$ is dropped from H_P . This is done in the following equations, and only the radiative mode is considered.

<u>The Radiative Mode</u>

The interaction term, H_{RP} , may be ordered in powers of A ; i.e.,

$$H_{RP} = H_{RP}^{(1)} + H_{RP}^{(2)} \quad \text{, where}$$

$$H_{RP}^{(1)} = - \frac{e}{c} \vec{A} \cdot \nabla \psi \, n \, d\tau \tag{72}$$

$$H_{RP}^{(2)} = \frac{e^2}{2mc} \int \vec{A}^2 \, n \, d\tau \tag{73}$$

When the radiation and the plasma fields are quantized by the usual methods, Equations (70) and (71) become

$$H_R = \sum_{\vec{k},\lambda} \hbar\, \omega_k \; \hat{c}^{+}_{\vec{k},\lambda} \; \hat{c}_{\vec{k},\lambda} \tag{74}$$

where the summation is over the k momentum states of the photon, and λ is a polarization index extending over the values 1 and 2 for transverse waves, and

$$H_P = \sum_{\vec{\kappa}} \hbar\, \omega_\kappa \; \hat{b}^{+}_{\vec{\kappa}} \; \hat{b}_{\vec{\kappa}} \tag{75}$$

where the summation is over the κ momentum states, $\hbar\kappa$, of the kth normal mode of the electronic motion. The creation and destruction operators for the photon and plasmon fields are $\hat{c}^{+}_{\vec{k},\lambda}$ and $\hat{c}_{\vec{k},\lambda}$ and $\hat{b}^{+}_{\vec{\kappa}}$ and $\hat{b}_{\vec{\kappa}}$, respectively.

If one is dealing with an imperfect plasma, that is, where there are structural irregularities, phonons, impurities, surface roughness, etc., the interaction terms may be altered to account for these static density variations (SDV). If we expand the density, n , as

$$n = n_o(\vec{r}) + n_1(\vec{r}, t) + \delta\, n_o(\vec{r})$$

where n_o is the constant electron density deep in the interior of the metal, n_1 is a small time-dependent term, and δn_o is a small static density term that accounts for the SDV, and we define $f(\vec{r}) = \delta n_o/n_o$, the interaction terms (72) and (73) are split into

$$H_{RP}^{(1)} = \frac{e}{c} n_o \int \vec{A} \cdot \nabla \psi_1 \, d\tau \tag{76}$$

and

$$H_{RP}^{(2)} = \frac{\omega_p^2}{8\pi c^2} \int \vec{A} \cdot \vec{A} \, d\tau + \frac{\omega_p}{8\pi c^2 n_o} \int \vec{A} \cdot \vec{A} \, n_1 \, d\tau$$

both of which ignore the effects of the SDV, and

$$H_{RP-SDV}^{(1)} = \frac{e}{c} n_o \int \vec{A} \cdot \nabla\psi_1 \, f(\vec{r}) \, d\tau \tag{77}$$

and

$$H_{RP-SDV}^{(2)} = \frac{\omega_p^2}{8\pi c^2} \int \vec{A} \cdot \vec{A} \, f(\vec{r}) \, d\tau$$

which includes these effects. The photon and volume plasmon fields do not couple in first order [Equation (76a)] because the photon field is transverse and the volume plasmon field is longitudinal, i. e., $\vec{A} \cdot \nabla \psi = 0$. However, in the presence of the SDV, first order coupling can occur [Equation (77)]. In fact many different coupling mechanisms arise when the proper operators are substituted into the total Hamiltonian, Equation (69), and these have been elucidated in some detail by Wilems and Ritchie. What we are interested in here is the particular mechanism that applies to grating-type metal surfaces. When we observe anomalies in grating diffraction, we are observing light (except for specular reflection) that has a different angle of emission

than incidence. This is a situation similar to PREL radiation, where the light is emitted in a direction other than the reflected beam.

The light that is emitted from thin foils at a frequency near the plasma frequency can be interpreted, according to Wilems and Ritchie, as the decay of the radiative mode surface plasmon through coupling of photons and surface plasmons via the SDV in the metal surface. With the SDV interaction, one need not conserve momentum parallel to the boundary, so the emitted light can leave the surface in some direction other than the reflected beam. The interactions that might be involved are shown in Figure 6 (a - e).

The transition rate for this process may be written as

$$w_{fi} = \frac{2\pi}{\hbar^4} \left| I + II + III + IV + V \right|^2 \delta(\omega - \omega') \tag{78}$$

where ω and ω' are the frequencies of the incident and emitted photons, and the numerals correspond to the most probable processes in the diagram, which are 6a, 6b, 6c, and two time orderings of 6c. The predominant contribution is that corresponding to diagram 6c:

$$III = \sum_{\vec{\kappa}'} \sum_{\vec{\kappa}} \frac{\langle f | H^{(1)}_{RNP} | I' \rangle \langle I' | H_{NP-NP-SDV} | I \rangle \langle I | H^{(1)}_{RNP} | i \rangle}{(\omega - \omega_p + i \frac{\gamma'}{2})} \tag{79}$$

where the summations are over the intermediate surface plasmon states, I , between the initial and final photon states, i and f, $H^{(1)}_{RNP}$ is the interaction Hamiltonian between the radiation field and the normal

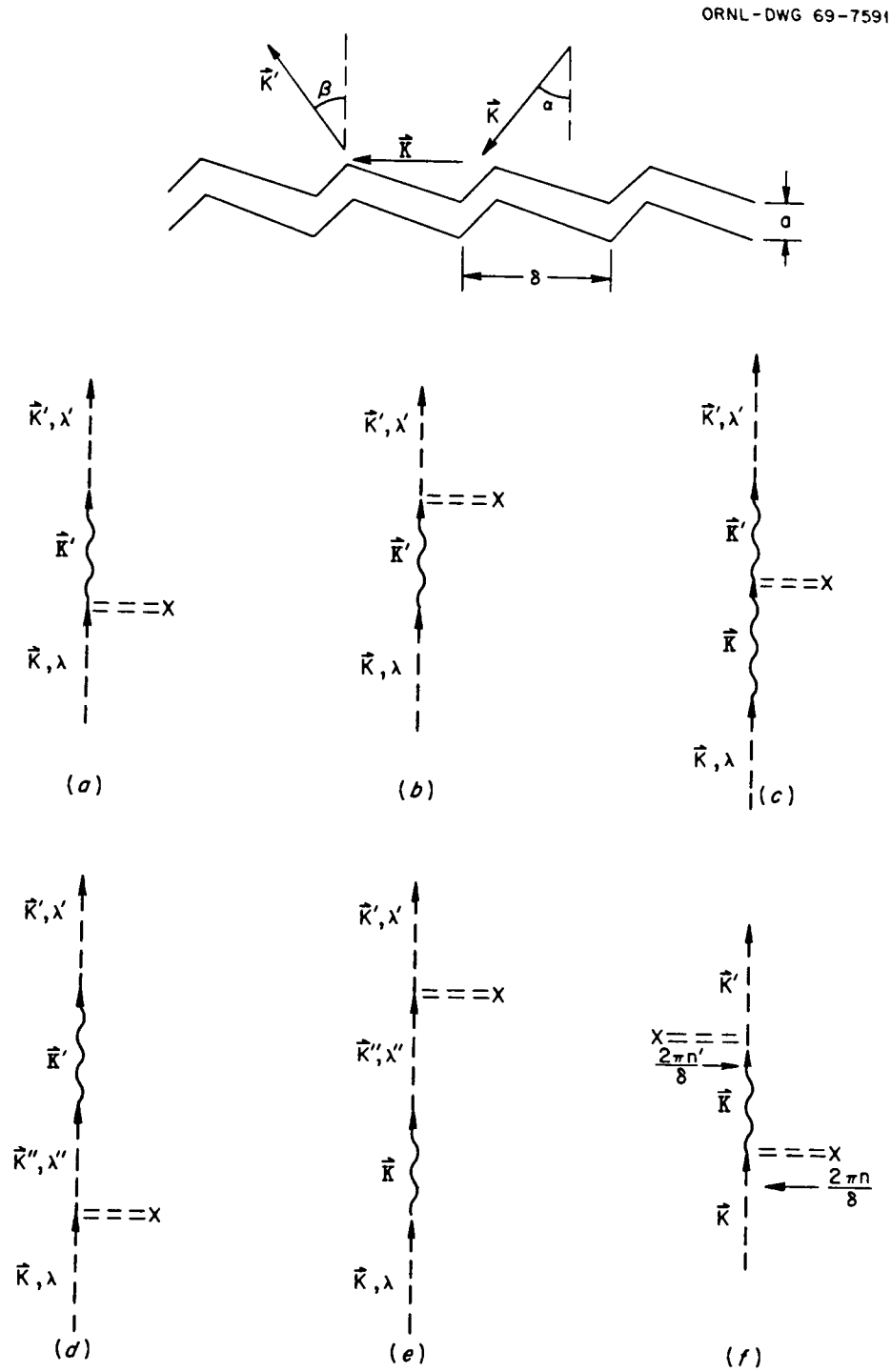

Figure 6. (a) - (e) Photon-radiative surface plasmon interactions in thin grating foils (f) photon- non-radiative surface plasmon interaction on semi-infinite metal substrate.

mode surface plasmon, and $H_{NP-NP-SDV}$ is the interaction Hamiltonian between the normal mode surface plasmons and the SDV, and $\gamma = \gamma_R + \gamma_d$ is the surface plasmon damping rate, which includes contributions from radiative and electronic damping. These special Hamiltonians result from the substitution of the proper potential operators for these modes into Equations (76) and (77). When one carries out the summations, the factor $(\hat{e}_{\vec{k},\lambda} \cdot \hat{z})$ appears, which tells us that only photons with a component of their polarization vectors in the z-direction, i.e., p-polarized light, are able to participate in the process. (See Appendix C.) When one carries out all the processes in Equation (78), obtains a transition rate, and then sums over the possible states of the emitted photon, one has the differential emission probability per unit solid angle for p-polarized light

$$\frac{dP_p}{d\Omega_f} = \frac{\pi^2 a^2}{16\lambda_p^4} \frac{\omega_p^2 [\omega_p^2 + 49 (\gamma + \gamma')^2/16]}{[(\omega - \omega_p)^2 + (\frac{\gamma}{2})^2][(\omega - \omega_p)^2 + (\frac{\gamma'}{2})^2]} \tag{80}$$

$$\times \frac{\sin^2\alpha \ \sin^2\beta}{|\cos \alpha|} G(\vec{k}_\rho - \vec{k}'_\rho)$$

where

$$\gamma = \gamma_d + \eta \tan \alpha \sin \alpha \tag{81}$$

$$\gamma' = \gamma_d + \eta \tan \beta \sin \beta \quad ,$$

a is the foil thickness. γ_d is the electronic damping rate of the plasmon, $\eta = \omega_p^2 a/2c$, and (α , β) is the angle of the (incident, emitted) photon relative to the foil normal. The terms in η , α and β account for radiation damping. The quantity $G(\vec{k}_\rho - \vec{k}'_\rho)$ is the Fourier transform of the autocorrelation function for the SDV in the plasma.

Although s-polarized photons are excluded from the process above, they do participate by elastic scatter. Using Fermi's Golden Rule the transition probability for this process is

$$w_{fi} = \frac{2\pi}{\hbar^2} \left|\langle f \left|H^{(2)}_{RP-SDV}\right| i\rangle\right|^2 \delta(\omega - \omega') \tag{82}$$

which by the same analysis as above leads to the differential probability per unit solid angle for s-polarized scatter on SDV

$$\frac{dP_s}{d\Omega'} = \left(\frac{\pi a}{\lambda_p}\right)^2 \frac{\cos^2 \psi}{|\cos \alpha|} G(\vec{k}_\rho - \vec{k}'_\rho) \tag{83}$$

where ψ is the angle between the unit polarization vectors of the incident and emitted photons.

The probability distributions, Equations (80) and (83), are for a thin foil where the surface roughness is incorporated into the autocorrelation function, $G(\vec{k}_\rho - \vec{k}'_\rho)$. If we have instead a grating foil the surface roughness is regular, and the function $G(\vec{k}_\rho - \vec{k}'_\rho)$ may be

calculated directly. The SDV function may be assumed periodic in x and may be expanded in the Fourier series

$$f(\vec{r}) = f(x, z) = \sum_{n=-\infty}^{\infty} f_n(z)\, e^{2\pi i n x/\delta} \tag{84}$$

where

$$f_n(z) = \frac{1}{\delta} \int_{-\delta/2}^{\delta/2} e^{-2\pi i n x/\delta}\, f(x,z)dx$$

and δ is the distance between adjacent rulings. Defining $\vec{k}_\rho = k_x \hat{x} + k_y \hat{y}$ where $\hat{x}$ and $\hat{y}$ are unit vectors along the x- and y- axes, one finds

$$G(\vec{k}_\rho) = (2\pi)^2\, \delta(k_y) \sum_n \overline{f}_n^{\,2}\, \delta(k_x + \frac{2\pi n}{\delta}) \tag{85}$$

where $\overline{f}_n$ is the average of $f_n(z)$ over the depth of the slab. Substituting (85) into (80) and (83) and integrating over all directions of the emitted photon, one finds the probability of nth order diffraction for p- and s- polarized light per incident photon to be

$$P_{pn} = \left(\frac{\pi a}{4\lambda_p}\right)^2 \frac{\sin^2\alpha\ \sin^2\beta}{|\cos\alpha||\cos\beta|}\, \overline{f}_n^{\,2} \times \frac{\omega_p^{\,2}\,[\omega_p^{\,2} + 49\,(\gamma + \gamma')^2/16]}{[(\omega - \omega_p)^2 + (\frac{\gamma}{2})^2][(\omega - \omega_p)^2 + (\frac{\gamma'}{2})^2} \tag{86}$$

$$P_{sn} = \left(\frac{\pi a}{\lambda_p} \right)^2 \frac{\cos^2 \psi}{|\cos \alpha||\cos \beta|} \bar{f}_n^{\,2} \tag{87}$$

where the diffraction condition $(\frac{\omega_p}{c}) \sin \beta = (\frac{\omega_p}{c}) \sin \alpha + \frac{2\pi n}{\delta}$ must be satisfied. If we take the ratio of these equations, the result is independent of the density term, f_n ,

$$\frac{P_{pn}}{P_{sn}} = \frac{1}{16} \frac{\sin^2 \alpha \sin^2 \beta \cos^2 \psi \, \omega_p^{\,2} \, [\omega_p^{\,2} + 49 \, (\gamma + \gamma')^2/16]}{[(\omega - \omega_p)^2 + (\frac{\gamma}{2})^2][(\omega - \omega_p)^2 + (\frac{\gamma'}{2})^2]} \tag{88}$$

which in this form allows direct comparison with experiment without knowledge of details of the surface density variations. Let us recall that Equation (88) is for the radiative mode excitation in thin grating foils for $\kappa \to 0$ and neglecting retardation.

The Non-Radiative Modes

When we investigate the non-radiative modes in the long wavelength region we must include retardation and we wish to consider semi-infinite grating surfaces as well as thin foils. The transition probabilities have not been worked out for the retarded case as they have for the non-retarded case considered above, but some qualitative assumptions can be made on the nature of the interaction involved and the form that the transition probability would take in this case [Ritchie, Arakawa, Cowan, Hamm (1968)].

We assume first that the surface plasmon is only slightly perturbed by the presence of density variations due to the grating structure.

For example, we assume that the dispersion curve of the plasmon on a grating surface will not be greatly different from that of a plasmon on a plane surface of the same material, at least in the long wavelength region. In this view, the anomalous resonances observed in the first-order diffraction spectrum may be interpreted in terms of the Feynman diagram shown in Figure 6f, page 65, in which we depict a second-order process. Here a photon of wave vector k in the region outside of the grating is incident upon the grating surface, which if perfectly plane would only specularly reflect the photon; a surface plasmon could not be excited under these conditions. Because there is a periodic denisity variation in the region of the surface, the grating may absorb momentum in a direction normal to the rulings and in multiples of $2\pi\hbar/\delta$ where δ is the distance between rulings. We shall assume that the average grating surface lies in the x-y plane, that the gratings are parallel to the y-axis, and that the wave vector k lies in the x-z plane. Thus at the lower vertex in the graph in Figure 6f a surface plasmon with x momentum equal to $2\pi\hbar n/\delta$ plus the x component of the momentum of the incident photon may be created. Here n is a positive or negative integer. Note the similarity between the momentum transfer processes considered here and the momentum conserving delta function in Equation (85) resulting from the Fourier transform of the SDV function. One sees that the qualitative interpretation of momentum processes arises naturally from the mathematical interpretation based on Fourier transforms.

The interaction Hamiltonian giving rise to this process is

$$H = -\frac{\omega_p^{\,2}}{4\pi c^2} \int \vec{A}_{ph} \cdot \vec{A}_{sp}\, f(\vec{r})\, d\tau$$

where the integration is over the half space containing the grating. $\vec{A}_{ph}$ is the vector potential operator of the photon, $\vec{A}_{sp}$ is the vector potential operator of the plasmon, and $f(\vec{r})$ is the fractional variation due to the grating structure of the conduction-electron density from its value n_o deep in the metal. As with the thin foil case, $f(\vec{r})$ can be expanded in the Fourier series, Equation (84).

In order for this effect to be observed in the first-order diffraction spectrum, the plasmon must, in general, get rid of some of the x momentum which it acquired from the grating by making a second encounter, indicated by the top vertex, (Figure 6f, page 65) in which a photon of wave vector k' is emitted. The compound process proceeds through an intermediate surface plasmon state. As we saw for the thin foil case, when the energy of an intermediate quantum state is nearly the same as that of the initial state, a resonance in the cross section for the compound process will occur. Thus we would expect that the probability, P_n, for the process under discussion would have the typical Lorentzian form

$$P_n \sim \frac{|F_n\, F_{n\pm 1}|^2}{[\omega_k - \Omega(\kappa_n)]^2 + [\frac{\gamma(\kappa_n)}{2}]^2} \tag{89}$$

which is valid in the neighborhood of the frequency for which the denominator has its minimum. We are neglecting here interference with the ordinary first-order diffracted beam. In this expression $\omega_k = c|\vec{k}|$, $\Omega(|\vec{\kappa}|)$, and $\gamma(|\vec{\kappa}|)$ are the eigenfrequency and damping rate, respectively, of a surface plasmon of wave vector $\vec{\kappa}$, and F_n is proportional to a certain average of the nth Fourier coefficient of the electronic density variation in the neighborhood of the grating surface. The momentum transfer relation is expressed by

$$\kappa_n = k_x + \frac{2\pi n}{\delta} \tag{90}$$

where κ_n is the absolute value of the surface plasmon wave vector, and k_x is the component of the incident photon wave vector parallel to the x-axis. There may also arise possible higher order processes giving rise to a probability function containing a product of several resonance denominators, as was found for the thin foil case.

In obtaining the probability relation, P_n, we expect terms of the type $(\hat{e} \cdot \hat{z})$ to arise, indicating that only p-polarized light participates in this process. This may be seen qualitatively from Figure 6, page 65, where a component of p-polarized light intersects the rulings and thus sees the density variations, while the components of s-polarized light are parallel to the grooves and thus do not see these variations.

The condition for intermediate state resonance is that the energy of the virtual surface plasmon should be equal to the energy of the incoming photon, i.e.,

$$\omega_k = \Omega(\kappa_n) \; ;$$

dropping the subscript on ω_k ,

$$\omega = \Omega(|(\frac{\omega}{c}) \sin \alpha + \frac{2\pi n}{\delta}|) \tag{91}$$

where α is the angle between $\vec{k}$ and the normal to the grating surface. Thus if the wavelength corresponding to the center of a resonance of given order n is measured as a function of the angle of incidence α , the dispersion curve Ω vs. κ may be constructed.

The angle of incidence α is given as a function of the angle θ by the grating equation

$$\alpha = \theta + \sin^{-1} \{ \frac{\pi \, n' \, c}{\delta \, \omega \cos \theta} \} \tag{92}$$

where n' is the order of the diffracted light. Using this in Equation (90), one obtains the dispersion relation

$$\kappa_n = \frac{\pi}{\delta} (2n + n') + \frac{\omega}{c} \sin \theta \sqrt{1 - (\frac{\pi \, c}{\delta \, \omega \cos \theta})^2} \; . \tag{93}$$

This is the equation that one uses to plot the experimental values, as shall be shown in Chapter V.

Surface Plasmon Self Energy

When consideration is made of the second-order self-energy of the surface plasmons, some very interesting results are obtained. This

self-energy involves the excitation of virtual plasmons with momenta differing from the momentum of the plasmon under consideration by multiples of $2\pi\hbar/\delta$. Mathematically we may express the self-energy as

$$\Delta E = \sum_I \frac{|\langle\kappa_I| H' |\kappa\rangle|^2}{E_p - E_I} \tag{94}$$

where E_p and E_I are the energies of the initial and intermediate states, respectively, and H' is the Hamiltonian describing the interaction between states κ and κ_I , where $\kappa_I = \kappa - \frac{2\pi n}{\delta}$. Near the light line we have $\omega = c|\vec{\kappa}|$ so the energy, $E \simeq \hbar c|\vec{\kappa}|$. If we now let $\kappa = \frac{\pi n}{\delta} + \Delta k$ we have

$$\Delta E = \sum_I \frac{|\langle\kappa_I| H' |\kappa\rangle|^2}{\hbar c\,[|\kappa| - |\kappa - \frac{2\pi n}{\delta}|]}$$

$$= \sum_I \frac{|\langle\kappa_I| H' |\kappa\rangle|^2}{\hbar c\,[\,|\frac{\pi n}{\delta} + \Delta k| - |-\frac{\pi n}{\delta} + \Delta k|\,]}$$

$$= \frac{1}{\hbar c} \sum_I \frac{|\langle\kappa_I| H' |\kappa\rangle|^2}{2\,\Delta k} .$$

This shows a discontinuity at vanishing Δk , which means that there will be discontinuities, or zone gaps, in the dispersion relation at values of κ equal to integer multiples of π/δ .

CHAPTER III

EXPERIMENTAL APPARATUS

In this study measurements were required of the diffraction spectra in different orders from concave reflecting-type gratings and from thin grating foils in a wavelength region extending from about 500 A° in the vacuum ultraviolet to about 14000 A° in the infrared. One of the first requisites was for a vacuum system that would prevent absorption of light in the short wavelength region and would enable vacuum evaporations to be made onto the grating surfaces in their operating positions. Other necessary components were light sources, polarizers, and detectors applicable for the wavelength regions studied, and the associated amplification and recording devices.

In the basic system light passes from a source through an entrance slit and is incident on the concave grating. Light diffracted from the grating is then focused through the exit slit to a detector, if the grating itself is under study. If the grating is used as a monochromator, the detector is replaced by a reflectance chamber, and light from the exit slit passes to the object under study (usually, a grating foil) and from there to a detector within the chamber. Two variations of the basic system were used in this study: one, operated at high vacuum in the wavelength region from 500 A° through 7000 A° and having the angle between the entrance and exit slits fixed at the Seya geometry is illustrated in Figure 7. The other, operated at atmospheric

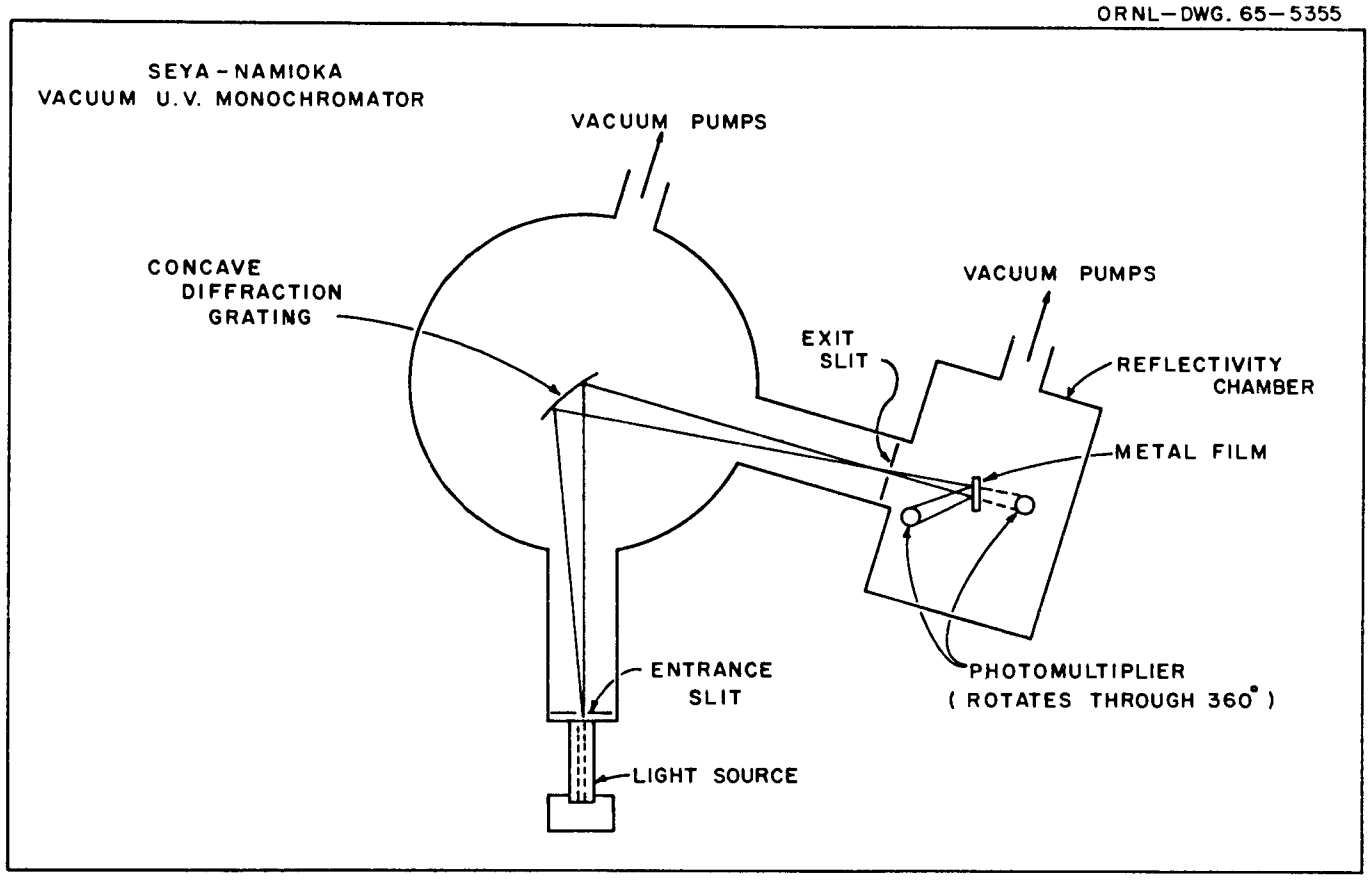

Figure 7. Schematic diagram of light source, spectrometer, and reflectance chamber.

pressure for wavelengths above about 2500 A°, had a variable angle between the source and detector, as shown in Figure 8. In each system polarizers could be placed at either the entrance or exit slits, but only the first system was used as a monochromator.

I. PRINCIPAL COMPONENTS

Light Sources

Several different light sources were used in this study, each applicable to a particular wavelength range. There is little difficulty in finding adequate sources of fairly high intensity above about 2000 A°. As one goes to shorter wavelengths problems of light stability and intensity over a continuous spectrum of wavelengths become more acute.

Commercially available lamps were used in the wavelength region above 2500 A°. An ordinary tungsten lamp was used in the visible and infrared range (4000-14000 A°) and from 2500-4000 A° , a Beckman hydrogen discharge lamp and a high pressure, high intensity xenon lamp (Oriel C-72-50) were used. The tungsten lamp provided a continuous, high intensity spectrum from 3500 A° to the upper limits of the present study. The Beckman lamp provided a comparatively lower intensity, and the spectrum was continuous from about 2500 to 3500 A°. The xenon lamp spectrum was continuous from about 2000 to 4000 A°, but of much higher intensity than either the Beckman or tungsten lamps. The intensity of this spectrum increases with increasing wavelength up to 4000 A°. Line

ORNL-DWG 69-6850

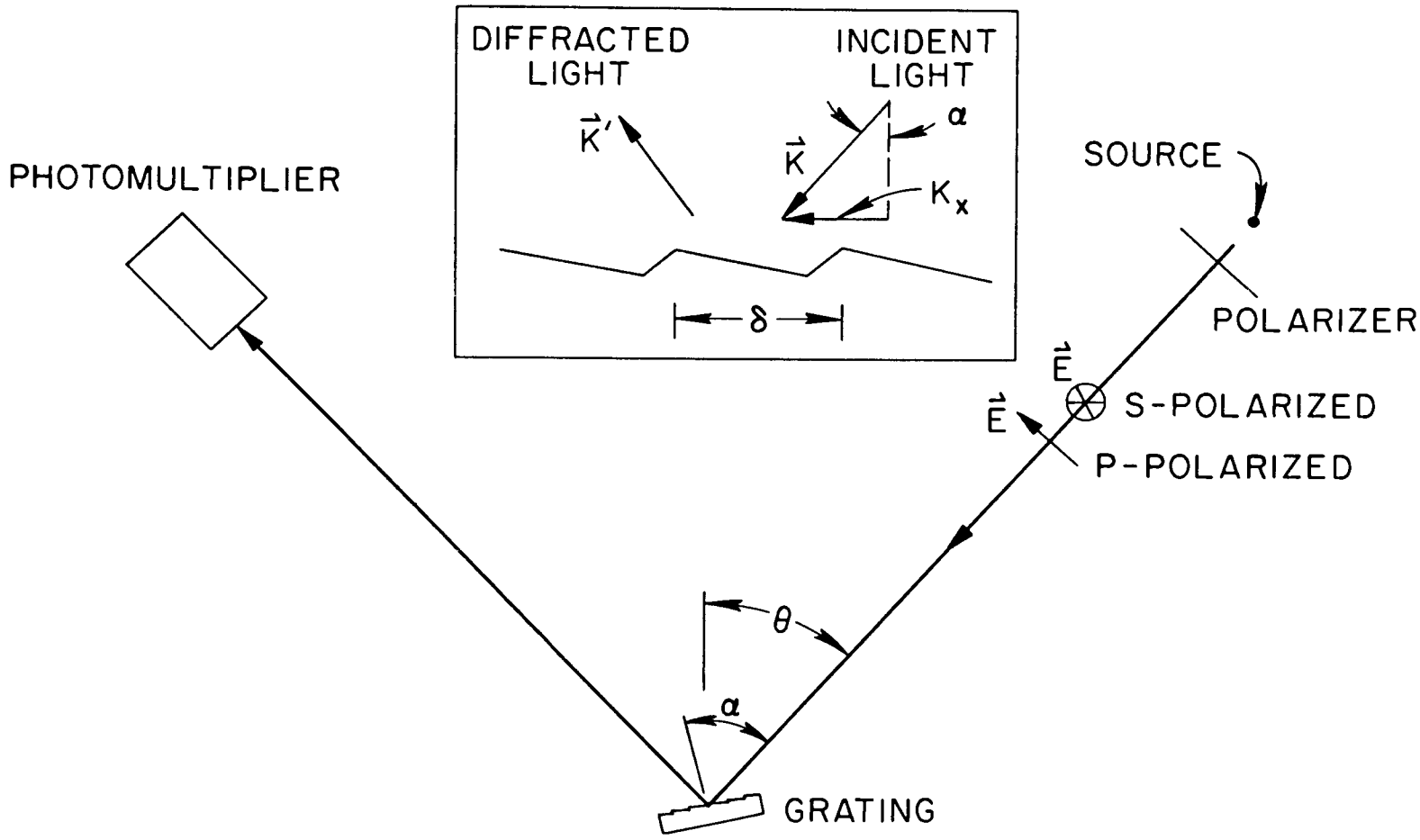

Figure 8. Schematic diagram of variable-angle apparatus. θ is the half-angle between the source and detector and α is the angle of incidence to the grating surface.

spectra superimposed on the background appeared in the Beckman and Xe lamp spectra at wavelengths longer than the continua for each. A prism monochromator was available for use with the Xe lamp with a wavelength drive and a minimum bandwidth of 10 A°.

For wavelengths shorter than about 3000 A°, a capillary discharge source was used. With this light source, a gas, such as air, hydrogen, helium, or argon, is injected at low pressure into a narrow capillary aligned along the optic axis. A high voltage applied between the ends of the capillary will cause, under appropriate conditions, a glow discharge to occur in what is essentially a gaseous plasma. These conditions for the creation and stability of the discharge depend on the gas pressure, the distance between the electrodes, and the voltage. The capillary can be either a glass or quartz tube with a water cooling jacket or a boron nitride cylinder, as depicted in Figure 9. Additional cooling is provided by the water jackets at the brass electrodes. The capillary fits into a receptacle on the monochromator, and a vacuum seal is provided by O-rings. The boron nitride capillary is about 8 cm long with an inner bore of 0.125 inches diameter, while the glass and pyrex capillaries are usually 7 cm long with a slightly larger diameter bore.

For wavelengths above 1000 A° the source was operated in the constant-voltage, or d-c mode, the high voltage being obtained from a commercial power supply (Consolidated Vacuum LC-031). For a stable, relatively high-intensity line spectrum, the typical operating conditions

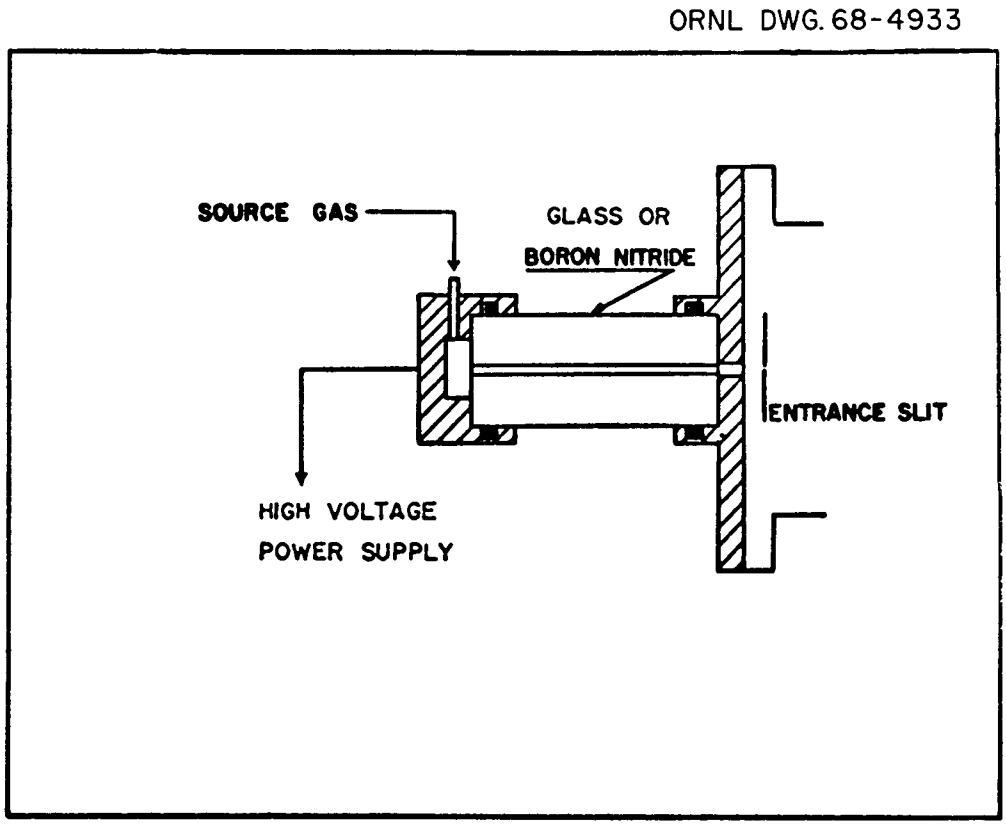

Figure 9. Configuration of the light source capillary tube.

were a current of 250 milliamperes at 1000 volts with a gas pressure of 1000 microns. The gas flow was regulated by a needle valve and the vacuum maintained by a 1/4-inch diameter tube leading from the capillary to the forepump, the pressure being read on a thermocouple gauge (Hastings DV-4DM).

To obtain wavelengths shorter than 1000 A°, the voltage supply must be operated in the spark, or intermittent, discharge mode. In this mode the power supply was connected to a large capacitor (0.1 microfarads) which was discharged at a constant rate (56 pulses per second) through the source by a rotating spark gap. The high voltages and the high peak currents through the gas excited line spectra down to 500 A°. Typical operating conditions for this mode were an average current of 100 ma at 5000 volts with a source pressure of 250 microns. Stability of the spark mode was improved by insuring that the gap between electrodes, which were made of 1/4-inch diameter tungsten rod, was just large enough for clearance in the conducting position.

Of the different gases used, air was found to be most effective in the 500-1200 A° region and above 1800 A° both for stability and the abundance of closely-spaced spectral lines (not more than 50 A° apart). For the same reasons hydrogen was the most effective from 1000-1800 A°.

Vacuum Monochromator System

The monochromator system was designed and built at the Oak Ridge National Laboratory to accommodate a concave diffraction grating having a radius of curvature of 50 cm and with the entrance and exit slits set

at the Seya geometry (70.1° apart). A third arm of the same size was also connected to the chamber halfway between the other two (35° from either the entrance or exit slit). The slit widths could be adjusted from a closed position to 6 mm by a micrometer screw attached directly to the slit assembly. The slit assemblies could be moved in or out of their respective arms for focusing purposes, the vacuum seal being maintained by O-rings. A vacuum-tight slide valve was also located on each slit assembly and it could be used to isolate the slits from the vacuum chamber.

The entrance slit assembly was equipped with ultraviolet filters to prevent light of certain wavelengths from reaching the grating and causing unwanted second-order light to appear in the spectrum. The LiF quartz, and glass filters, were mounted on a vacuum-tight metal slide that could be controlled from a movable rod outside the assembly. LiF stops transmitting below about 1100 A°; quartz at 1550 A°; and glass at 2500 A°. Below 1100 A°, no filter was used, the slide being moved to an "open" position. With the slide in this position, the entrance slit was open to the vacuum chamber and a pressure differential existed from one side of the slit which was at a few hundred microns pressure to the other which was in the range of 10^{-6} Torr. A small magnet was placed just inside the vacuum chamber to sweep any charged gas particles out of the optical path.

Vacuum System

Initial pumpdown was accomplished by a rotary forepump (Welsh model 1397) and final evacuation, by a six-inch diffusion pump (National Research Corporation model VHS6) having a pumping speed of 2400 liters per second at 10^{-6} Torr and using Dow-Corning No. 704 pump oil. The diffusion pump, which was backed by the forepump and had a water cooled baffle between the pump and the vacuum chamber to prevent backstreaming of the oil vapor into the vacuum chamber, could achieve an operating pressure between 10^{-6} and 10^{-7} Torr. The forepump pressure was measured with a thermocouple gauge (Hastings DV-4DM) and the vacuum chamber pressure with an ionization gauge (Veeco RG 75K).

The reflectance chamber had a similar vacuum system, but it was not used in this study since reflectance chamber measurements were made only at atmospheric pressure.

Variable-Angle Optical System

It was necessary in this work to measure the diffraction spectra of a given grating for several different angles between the source and detector, and thus the vacuum monochromator system described above was unsuitable, but since the measurements were made at wavelengths longer than 2500 A°, no vacuum system was necessary. Only the tungsten, Beckman, and xenon lamps were used for these measurements. The drive mechanism of a grating calibrator that is used to rotate gratings at a constant rate was adapted for this work by attaching it to an optical bench. A slit assembly consisting of an adjustable width slit and a

tube several cm long and of 3/4-inch diameter could be clamped to a ringstand and placed at various distances from the grating in front of the source or detector. A protractor attached to the axis of the grating drive mechanism permitted the angle between the source and detector to be measured to within 5 minutes.

Polarizers

In the vacuum- and near-ultraviolet spectral region (500-3000 A°) a triple-reflection polarizer developed at the Oak Ridge National Laboratory was used [Hamm, MacRae, and Arakawa (1965)]. With this polarizer a beam of light is reflected at large oblique angles (60° to 80°) from three gold mirrors in succession, and emerges in a direction parallel to the incident beam. Light passing through this polarizer is from 90 to 98 per cent plane polarized.

For wavelengths greater than 2700 A°, a sheet polarizer (Polaroid HN-22) was found to be the most effective, producing light that is highly plane polarized for wavelengths from the near ultraviolet through the infrared. This polarizer is opaque to wavelengths shorter than about 2700 A°.

Both polarizers could be mounted in assemblies attached to the entrance or exit slits of the vacuum monochromator and rotated by a crank mechanism from the outside.

Detection and Amplification System

Light intensities were detected in the 500 to 7500 A° spectral region by photomultiplier tubes and above 7500 A° by a PbS detector.

The photomultiplier attached directly to the monochromator and also used in the variable-angle apparatus was an EMI 9558 BQ operated at about 1000 volts and the one used in the reflectance chamber was an RCA 1P28 operated at about 550 volts. The window of each photomultiplier was coated with a layer of sodium salicylate to increase the quantum efficiency in the far ultraviolet. Photocurrents in the range of 10^{-7} to 10^{-11} amperes were measured with a picoammeter (Keithley model 409) and recorded by a chart recorder (Minneapolis-Honeywell Brown, 10 millivolt). The PbS detector was used with the picoammeter and with the a-c amplifier described below.

When one has a weak signal superimposed on a large background intensity, it is convenient to use different amplification methods from the one described above. If the weak signal is alternating periodically, then this a-c signal can be isolated from the large d-c background and amplified by a lock-in amplifier. In this amplifier an internal oscillator or a "reference signal" is tuned to the same frequency as the signal, that is, is "locked-into" it, and all other signals are blocked by a filter capacitor. Then the signal is amplified and can be fed into a recorder. In this study the signal is the difference in the intensity of spectral light excited by incident p and s polarized light. If the sheet polarizer that is located in either the incident or diffracted beams is rotated at a known rate an alternating signal will reach the detector that is proportional to this difference. Since the polarization is changed twice for each revolution, the amplifier must be tuned

to twice this frequency. In our case the polarizer was mounted on a bearing that was driven at 30 revolutions per second by a synchronous motor, and the lock-in amplifier (Princeton Applied Research HR-8) was tuned to 60 cycles per second. With the photomultiplier as the detector, the output was branched into two parts, one going to the input signal terminal and the other to the reference signal terminal of the lock-in amplifier. With the PbS detector the operating power was obtained from a 90 volt battery that was connected in series with the detector and with a 10,000 ohm load resistor. The a-c output signal was taken from either side of the load resistor and fed into the amplifier as described above. When used with the d-c output, the PbS detector was connected directly to the picoammeter.

Vacuum Evaporator

Vacuum evaporations could be performed directly onto the grating surfaces in their operating positions by an evaporator connected to the central arm of the vacuum monochromator. Two brass electrodes, each 25 cm long and 1/2-inch in diameter were attached through O-ring sealed holes to a 1/2-inch thick Lucite plate that was bolted to the flange on the central arm. Evaporation filaments could be attached to the ends of the electrodes about 25 cm from the grating surface. The filaments were heated by step-down transformers operating through high-current rheostats that drew currents on the order of 200 amperes.

Reflectance Chamber

The reflectance chamber was a stainless steel cylinder 16 inches long and 8-1/2 inches in diameter that could be attached directly to the exit slit flange on the vacuum monochromator. The sample holder could accommodate thin foils and was capable of being lifted vertically or rotated mechanically from the outside through 360 degrees. The photomultiplier tube could be rotated in a similar manner around the axis of the sample holder. Large glass viewing ports could be sealed so that the chamber was light-tight. Angles could be measured to within 0.5° by a vernier scale attached to an angle doubler outside the chamber.

Film Thickness Monitor

The thicknesses of the films evaporated in the vacuum system could be measured at the time of deposition by a film thickness monitor (Edwards High Vacuum, Ltd., model FTM-1). This instrument utilizes a quartz crystal that is placed near the substrate so that it is coated with the same thickness of evaporated material as is the substrate. The principle of operation has been described by Garber, et al. (1969). The crystal used was masked by a metal shield except for a 0.5 cm diameter opening in the center. The two lead-in wires were connected to vacuum-sealed electrodes in the Lucite port containing the evaporator electrodes.

Anodic Oxidation Apparatus

It was found that an effective method of producing oxide coatings on the aluminum grating substrates was the anodic oxidation method

described by Hass (1949). In this method one uses an electrolyte that contains a three per cent ammonium tartarate solution by weight and sufficient ammonium hydroxide to produce a pH value of 5.5. A sheet of pure aluminum is connected to the cathode and the aluminum surface to be oxidized is connected to the anode. If a voltage is applied an oxide layer forms whose thickness is proportional to the voltage. In this study the voltage source was a 300-volt regulated power supply that had less than 0.1 volt ripple in the output.

Diffraction Gratings

The diffraction gratings investigated in this work included the Bausch and Lomb concave replica gratings and plastic replica grating foils. The concave replicas had Al and MgF_2-coated Al surfaces with 600 lines/mm and blazed for 1500 A°, and Au and Pt surfaces with 1200 lines/mm and blazed for 700 A°. For details on replica gratings in general, see Bausch and Lomb (1967). The plastic replicas consisted of thin plastic sheets with a 600 line/mm grating surface on one side and were available either uncoated or with a 300 A° overcoating layer of Al (Edmunds Scientific Co.). The only surfaces, however, that exhibited anomalies were the 600 line/mm concave replicas.

If the grating grooves are cut in such a manner that the maximum intensity of light falls at a particular wavelength, the grating is said to be blazed for that wavelength, and the groove face angle is called the blaze angle. The blaze angle and the blaze wavelength can be calculated by assuming that the angle of incident light is the same as

the angle of diffraction. In this case the grating equation reduces to

$$n\lambda = 2\delta \sin \beta \ .$$

When β is equal to the blaze angle θ the first order blaze wavelength, λ_β, is given by

$$\lambda_\beta = 2\delta \sin \theta \ .$$

Thus we find that a 600 line per mm grating blazed for 1500 A° has a blaze angle of 2°35' (See Figure 1, page 3).

The above calculation is for a flat surface. If the surface is curved then ideally the blaze angle should vary slightly from one edge of the grating to the other, but practically it is difficult to fabricate a grating in this way. On concave gratings a compromise is reached by ruling the grating in three areas, a middle portion and two edges, with each one having a constant blaze angle. The middle portion is blazed with the value calculated above. The blaze angles of the edges are only slightly different from this value.

CHAPTER IV

EXPERIMENTAL PROCEDURES

Measurements of polarization effects in diffraction spectra are not inherently difficult in the pressure range used in this study. The primary concerns are those of source stability and intensity at short wavelengths, the reduction of scattered light that contributes to the background intensity, the proper optical alignment and wavelength calibration procedures, and, what is probably the most difficult in this work, the preparation of reasonably high-quality metal and dielectric grating surfaces on thick substrates and thin foils.

This chapter includes first a discussion on the preparation of the different grating surfaces used. This is followed by a description of the various techniques of alignment and measurement with the vacuum monochromator, reflectance chamber, and variable-angle apparatus.

I. PREPARATION OF GRATING SURFACES

In cases where vacuum evaporation techniques are used to measure, for example, the optical constants of a given metal, the substrate onto which the metal is evaporated must be thoroughly cleaned by some rather stringent methods to remove any impurities from the surface. Often these substrates are glass slides that are not damaged when subjected to heat and acid exposure. In this study, however, the substrates were grating surfaces of metal or dielectric materials that were extremely

sensitive to any outside agent. Great care had to be exercised in handling these surfaces since a slight alteration of the periodic surface structure such as rubbing off the tops of the grooves, or scratching or pitting the surface, or causing undue roughness of the surface, could result in spurious scattering effects and unwanted broadening and loss of intensity of the anomalous polarization peaks.

The surfaces that were used most often as substrates were the aluminized concave 600 line per mm gratings blazed for 1500 A°. Two methods were found that were reasonably effective in cleaning this surface. The first method was to rinse the grating in a slowly running stream of distilled water for about 15 minutes, and then to remove residual water droplets by rapid evaporation using a warm-air blower. Small dust-like particles that adhere to the grating either from short exposure to air or from evaporant contamination from the evaporation system could be removed in this way. Vacuum system contamination was not common, but could result from repeated evaporations where the small metal evaporated particles would not adhere to the chamber walls and could be stirred up when the system is opened to atmospheric pressure. The second, and more effective method, was to coat the grating with a thick layer of metal, usually 1500 A° to one micron of aluminum, and then to remove this layer with Scotch Tape. This method, which has been described by Hass and McFarland (1950) does not harm the grating in any way and the impurities are removed along with the evaporated metal and the tape. This method was also found to be effective in removing

diffusion pump oil contamination, which adheres in molecular layers to the surface after the grating has been in the vacuum system for weeks and months. In some cases several evaporations were made in succession onto the grating without exposing the system to atmospheric pressure, and the chance of surface contamination was believed to be less severe than if the vacuum were broken down and the grating were cleaned after each evaporation. Care must also be taken when multiple evaporations have been made because in cleaning by the stripping operation, the tape often removes all evaporated layers down to the bare substrate.

The plastic replica gratings that were also used in this work were even more susceptible to surface damage than the concave replicas. No attempt was made to clean these surfaces as above, but they were stored in dust-tight containers until ready for use.

Vacuum Evaporation

The grating substrates were coated with layers of metal that condensed onto the surface after being vacuum evaporated from a heated tungsten filament. The metals used were aluminum, gold, and silver, and each had a purity of over 99.99 per cent and was in wire form of about 20 mil diameter. The metal to be evaporated was inserted into or wrapped around the tungsten filament, which was made of three woven strands of 25 mil diameter wire fashioned into a helix about one inch long and 0.25 inches in diameter and had about a half-inch of straight wire on each end. This filament could be attached to the evaporation electrodes that were connected through the Lucite window.

The preliminary procedure was to position the concave grating to be coated in its holder and rotate the grating table until the surface was parallel to the filament to prevent any metal from striking the surface obliquely. The thickness monitor crystal was positioned in a holder on one side of the grating and a clean glass slide on the other side, both being at the same distance, 25 cm, from the filament as was the grating. A shutter between the filament and the grating was attached to the lid of the monochromator and could be swung out of the way from outside the vacuum chamber.

After charging the filament with the desired amount of metal, the system was closed and pumpdown begun, first with the roughing pump and finally with the diffusion pump. The system reached a vacuum of about 4×10^{-6} Torr in about 2 hours, but usually it was allowed to pump for 12 to 24 hours, when it reached about 1×10^{-6} Torr. The entrance and exit slits were isolated from the vacuum chamber by the slide valves and the thickness monitor gauge was set to the null position. Current was then applied to the filament, melting the metal enough so that outgassing could occur. After a few seconds of outgassing, the shutter was opened, and the current was increased enough to evaporate at about a rate of 200 A° per second. It was desirable to make the evaporation as fast as possible, since Holland (1961) has shown that this produces a much smoother film than a slow evaporation, especially for layers up to 300 A° thick.

If a substrate other than the concave grating were to be coated, e.g., the plastic replica grating, the same procedure was followed, except that the grating holder was removed and the new substrate placed into its position.

The reading on the thickness monitor had been calibrated to read 14.4×10^{-8} gram of metal evaporated per square centimeter per scale division by interferometry techniques. This thickness value could be checked in this work by comparing with the thickness of metal evaporated onto the glass slide, which was done by measuring the per cent of light transmitted at a given wavelength through the metal and comparing with transmittance-thickness charts obtained previously for this metal. The procedure here was to use the xenon lamp set for the green mercury wavelength (5461 A°) by the prism monochromator to measure transmission through the metal-coated glass slide and then through a (similar) glass slide with no metal, the ratio of these readings giving the transmission through the metal alone.

One might ask, in analyzing the evaporation process on a grating surface, whether or not the grooves are filled up by the evaporated metal. It has been shown by several investigators that this, in fact, does not happen and that the evaporated layers adhere to a uniform thickness across the whole surface, regardless of the structural irregularities [Emerson, et al. (1963), Teng and Stern (1967), Hass and McFarland (1950), Anderson, et al. (1965)].

Anodic Oxidation Technique

The preparation of dielectric films such as Al_2O_3 and MgF_2 on a substrate is difficult to do by vacuum evaporation since high filament temperatures are required and often special evaporation boats and techniques must be used to insure an even, high-quality layer free of clumps and globules of evaporated dielectric. Since we are interested in investigating Al_2O_3 dielectric layers, these problems could be bypassed by the use of the anodic oxidation apparatus described in the previous chapter for the production of non-porous oxide films on aluminum substrates. This method was convenient to use in this study because of the concave gratings being originally provided with aluminum substrates. The grating surface itself is rectangular (3 × 5 cm) and is mounted by epoxy cement to the concave surface of a plano-concave glass blank one cm thick and 6 cm in diameter, and the rest of the concave surface not covered by the grating is coated with a thick layer of aluminum. Thus the whole concave surface is conducting. A thin aluminum strip was clamped on one end to the aluminum non-grating part of the concave surface and on the other end to the anode of the anodization apparatus. The grating blank was then placed in the electrolyte until one-third or 2/3 of the grating surface was immersed, depending on which portion of the surface anodization was desired (Figure 10). According to Hass (1949) the voltage-thickness relation is linear, the layer thickness being 13.5 A° per volt for an anodization time of over two minutes. For thicknesses of less than 200 A°, however, the relation has been shown to be non-linear, as given in Figure 11.

ORNL-DWG 69-7580

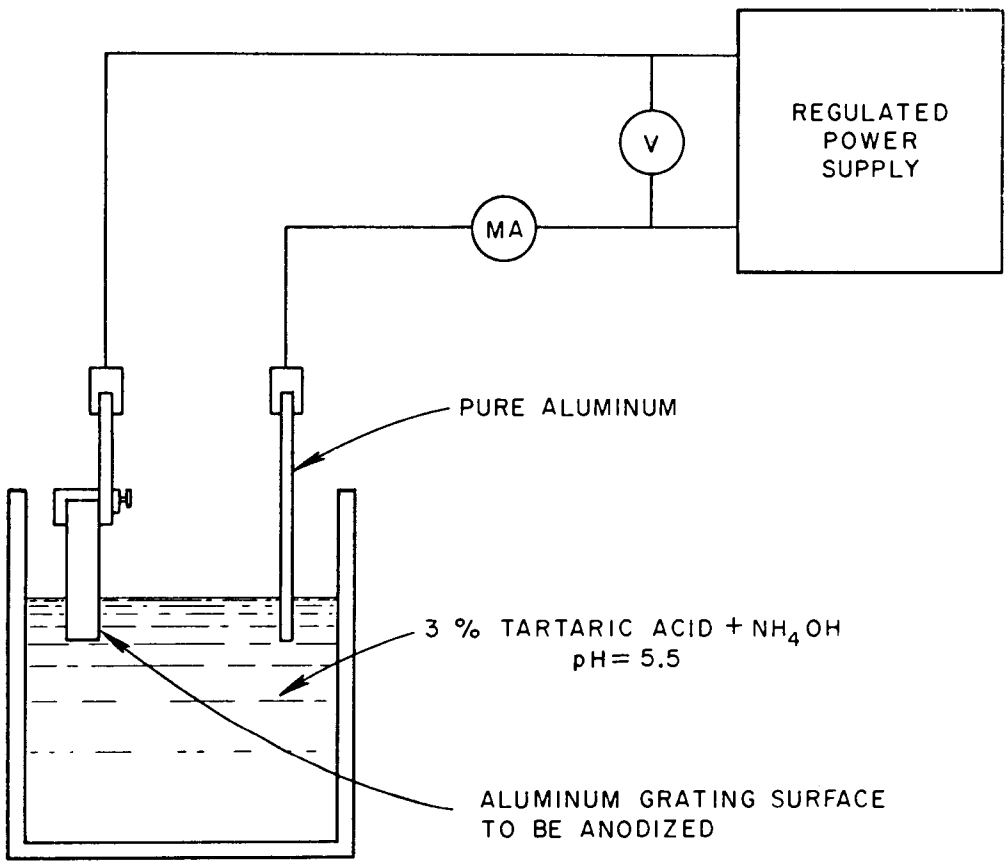

Figure 10. Anodic oxidation apparatus.

ORNL DWG 65-4270

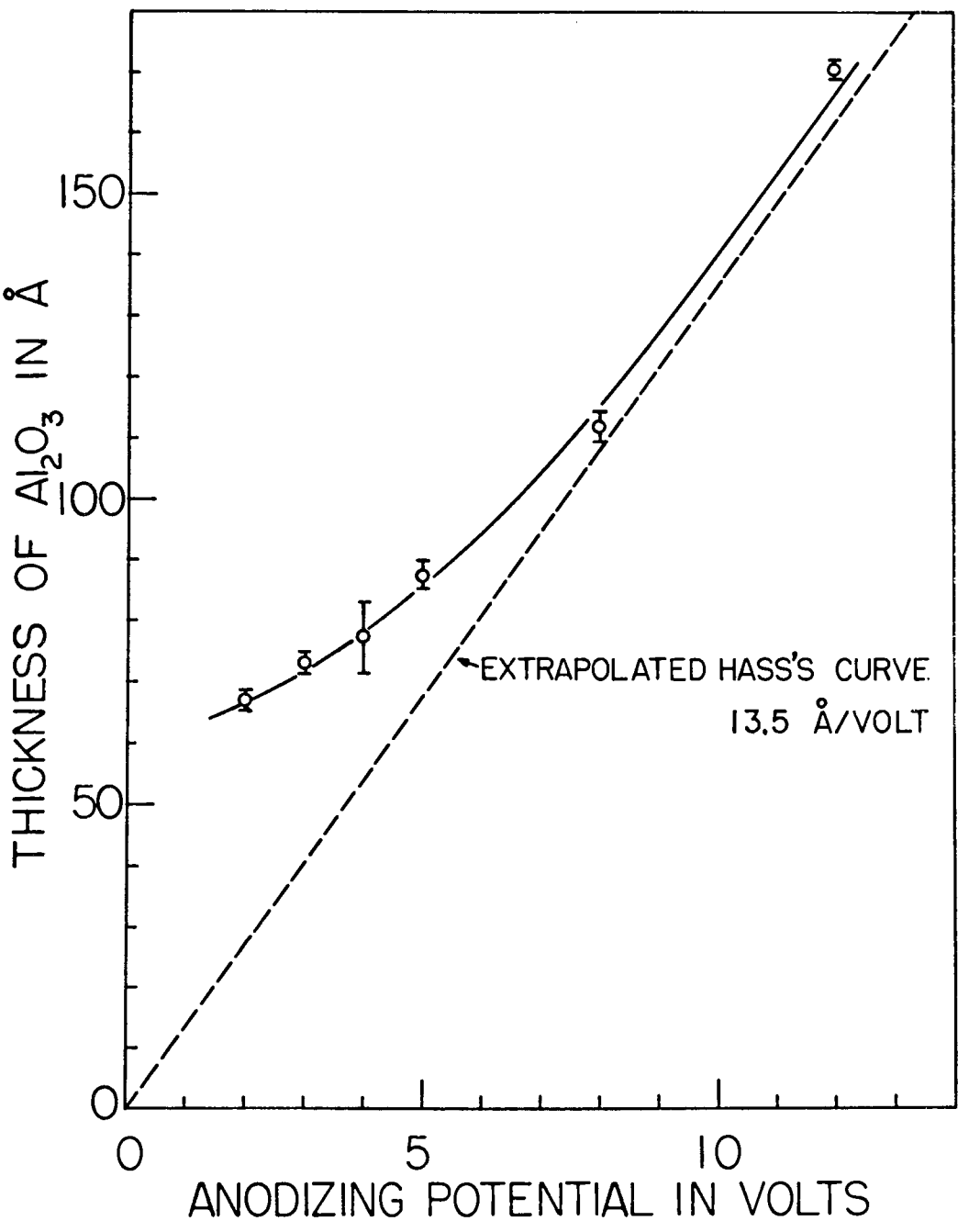

Figure 11. Oxide thickness versus applied voltage.

The validity of this curve has been questioned, some authors holding the view that the thickness values should be one-half what they are given here [Garber, et al. (1969), Aisenberg (1967)].

The anodization technique was useful only on the original grating substrate, because when one attempted to anodize an aluminum layer of several hundred A° thickness that had been evaporated onto the substrate, the surface layer deteriorated by peeling and the formation of bubbles. The probable reason for this behavior is that this method requires an exceptionally clean surface, and because of the problems mentioned earlier, it is difficult to evaporate onto a substrate entirely free of impurities.

Grating Foils

In the usual method of preparing thin self-supported metal foils one evaporates a desired thickness of metal onto a glass slide previously coated with a wetting agent. If one immerses the slide in water the foil separates and floats on the surface where it can be picked up by a foil holder. This procedure was not successful, however, when applied to a grating surface as the layer adhered to the substrate and did not separate under water. This is probably because the adhesion between the evaporated metal and the substrate (either Al or Al_2O_3) was large, even in the presence of the wetting agent, and also because the surface was not smooth. So other methods had to be used to make grating foils.

It was found that if the aluminized plastic replicas (Al thickness - about 300 A°) were subjected to the anodization process, the

aluminum layer would separate from the plastic substrate and could be floated off in the electrolyte. These self-supporting foils (of total thickness - about 300 A°) had thicknesses of Al and Al_2O_3 that depended on the applied voltage and they appeared to maintain their grating shape and uniformity even for this small thickness. When the clear plastic replicas,on the other hand,were coated in the vacuum system and then anodized the surface deteriorated as before.

When it was not necessary to have a self-supporting foil, such as with Ag, one could mount the foil on a thick dielectric substrate. It was found that the best method for making foils of this type was the same as that used to clean the substrate. For example, a Ag grating foil was made by coating the original aluminized surface of the concave grating with 300 A° of Ag, pressing a strip of Scotch Tape onto this, and then slowly stripping off the tape. The entire Ag layer adhered to the tape, the 300 A° thickness being verified by transmission measurements, and the grating surface was of reasonably high quality. One could make electron micrographs to check the surface quality, but usually one could determine this visually simply by observing the brightness and resolution of the diffraction spectrum of the grating foil.

An attempt was made to produce a grating foil by the method described by Hass and McFarland (1950), where one coats a grating with a thick Al layer, removes it with tape, anodizes the layer on the tape, and then separates the tape from the anodized layer. When this was tried with about 2000 A° of Al, it was found that the Al layer cracked

upon removal into many small areas on the tape and would not conduct when connected to the anode. Hass used a much larger thickness than this, however, (about one micron), and it may be that the cracking problem will not arise with a thicker Al layer. Hass also used a thin Mg layer between the tape and the Al layer which we did not use, but this should have had no effect on the cracking problem.

A special type of grating foil could be made very easily by coating onto a fairly thick (several hundred A°) anodized Al_2O_3 layer on the concave grating a metal layer of desired thickness. This type of "foil" has the advantage of being a high quality grating surface that can focus the diffracted light without distortion and of exhibiting thin foil behavior with the exception that the air boundary is replaced by an Al_2O_3 layer and a metal substrate (see Chapter II).

A method was used to prepare a thin metal grating "foil" on a dielectric substrate that is similar to that used for making replica concave gratings [Jarrell and Stroke (1964)]. The concave grating substrate is coated with a vacuum evaporated layer of metal, and this is coated with a thin epoxy resin layer. Immediately a large glass convex (lens) surface of similar radius of curvature is pressed against this, and the epoxy is allowed to set for 24 hours. The surfaces can then be separated by wedging a thin knife edge between them. The thin metal layer adheres more to the epoxy than to the substrate and is thus removed with it. A very good grating surface is formed in this way and one may study it in this geometry; however, with a convex surface one needs an

additional lens for focusing. The process can be continued by coating the convex surface with another vacuum evaporated metal layer, applying an epoxy layer to it, pressing this against a glass plano-concave grating blank, and separating as above. One now has a thin metal layer on a concave surface bounded effectively by semi-infinite glass and air layers on either side. This method has the advantage of producing grating surfaces almost as good as the original, but it is time consuming and it is often difficult to separate the epoxy treated layers.

One last method was to vacuum evaporate metal layers onto the clear plastic replica gratings or simply to observe the aluminized plastic replicas, but as pointed out earlier, these gratings did not show anomalous polarization effects.

It may be added that the only one of these methods useful for Al foils in the vacuum ultraviolet is the direct coating of the dielectric concave layer, since with the other methods the vacuum must be broken down and the foil exposed to air before measurements can be made.

II. THE VACUUM MONOCHROMATOR SYSTEM

Optical Alignment

To align the optical system of the vacuum monochromator one opens the system to atmospheric pressure, places the concave grating in position, and replaces the capillary light source with a tungsten bulb. The reflectance box is detached from the monochromator and a frosted glass slide is taped over the exit slit. With the entrance and exit

slits set at their usual operating widths of 150 microns, the grating is rotated until the central specular reflected image is focused on the exit slit. Vertical positioning of the image and fine focusing can be accomplished with the entrance and exit slit assemblies by rotating them or by moving them in or out of their respective arms and observing the position and sharpness of the image on the glass slide. For still finer adjustments the glass slide can be replaced with a magnifier. The grating is adjusted so that the grooves are perpendicular to the plane of incidence, which is that plane formed by the incident and diffracted beams. The fore and aft tilt of the grating is also adjusted so that the diffracted orders also are focused at the same position on the exit slit as is the central image. Baffles are placed in the entrance arm so that the light striking the grating is confined to a given area of the ruled surface, and in the exit arm so that only the exit slit is illuminated. Then with the system closed and the photomultiplier connected to the exit slit assembly, the grating is rotated to the central image position until the photocurrent is maximum, and then the wavelength register is set to zero. Calibration is done by replacing the tungsten bulb with a Hg lamp and comparing the register readings with the known wavelengths of certain lines in the Hg spectrum.

Resolution

The resolution of the monochromator system depends on the radius of curvature and line spacing of the grating, the distance between the grating and the exit slit, and the width of the exit slit. If we assume

a 600 line per mm grating and an angle of incidence of 35°, we obtain from the grating equation [Equation (1)] a diffraction angle of 41.5° for 1500 A° and 74.5° for 6500 A°, giving a 5000 A° spread over 33°. If the distance from the grating to the exit slit is 40 cm, then the grating dispersion is 22 A° per mm. For an exit slit width of 150 microns, the resolution is thus 3.3 A°. For a 1200 line per mm grating the spectrum is spread over an angle twice as large and the resolution is twice as good at 1.6 A°.

Polarization Measurements

Once the optical alignment of the system has been completed the triple polarizer assembly can be clamped into position at the exit slit. The central image of the tungsten bulb that diverges from the exit slit is reduced by tape baffles at the slit to a spot of light about 2 mm square at the exit side of the polarizer, and is observed on a frosted glass slide taped to it. The assembly is then adjusted up or down or from side to side so that when the polarizer is rotated the beam stays in the center. This is necessary because if the beam wanders over a large area of the phototube the response may be different due to possible non-uniformity in the sodium salicylate coating.

With the phototube in position at the exit side of the polarizer the system is pumped down and allowed to stabilize at 1 to 2 × 10^{-6} Torr. Evaporations onto the grating surface can be made at this time, if necessary, according to the procedures mentioned in the previous section.

Intensity measurements can then be made for two orientations of the polarizer; one, I_p , with the planes of incidence of the polarizer and grating perpendicular to each other, and the other, I_s , with the polarizer and grating having a common plane of incidence.

The plane of incidence of the grating or the polarizer is that plane formed by the incident and reflected (or diffracted) beams, and light whose electric vector is parallel and perpendicular to this plane is p- and s-polarized light, respectively. If we define the reflectances of the grating and polarizer for p- and s-polarized light as (R_p, R_s) and (r_p, r_s), respectively, then we may express the degree of polarization introduced by each by the polarization ratios

$$P = \frac{R_p}{R_s} \qquad \text{for the grating, and}$$

$$\rho = \frac{r_p}{r_s} \qquad \text{for the polarizer .}$$

For incident unpolarized light of intensity I_o , the measured intensities may be expressed as

$$I_s = \frac{1}{2} I_o (R_s r_s + R_p r_p) = (\frac{1}{2} I_o R_s r_s)(1 + P\rho)$$

$$I_p = \frac{1}{2} I_o (R_s r_p + R_p r_s) = (\frac{1}{2} I_o R_s r_s)(\rho + P) .$$

Solving for P we obtain

$$P = \frac{I_p - I_s \rho}{I_s - I_p \rho} .$$

The ratio, ρ , has been calculated from Fresnel's equations using published values of n and k for gold [Canfield, Hass and Hunter (1964)] and the known incidence angles (75°-60°-75°) of the triple polarizer and is given in Figure 12 for the vacuum ultraviolet region.

The general procedure is to pick a strong spectral line in the wavelength region desired and obtain at least two readings for each p and s orientation of the polarizer. This is repeated for other lines, preferably not more than 50 A° apart. Then the background intensity, which is due to unwanted scattered light, must be subtracted. This can be done by slowly scanning the spectrum, with and without the ultraviolet filters, and measuring the p and s intensities in regions where there are no spectral lines. Usually the background has a low and constant value but may often increase in the short wavelength region near the central image, or for measurements made at spectral lines that are weak. The I_p and I_s values are those measured above the background intensity.

When using the Polaroid sheet polarizer assembly for measurements at longer wavelengths, the adjustment requirements are much easier, since the beam is not deflected as with the triple polarizer, and the grating polarization, P , can be obtained simply from the ratio I_p/I_s , since the Polaroid is so highly polarizing in a given plane.

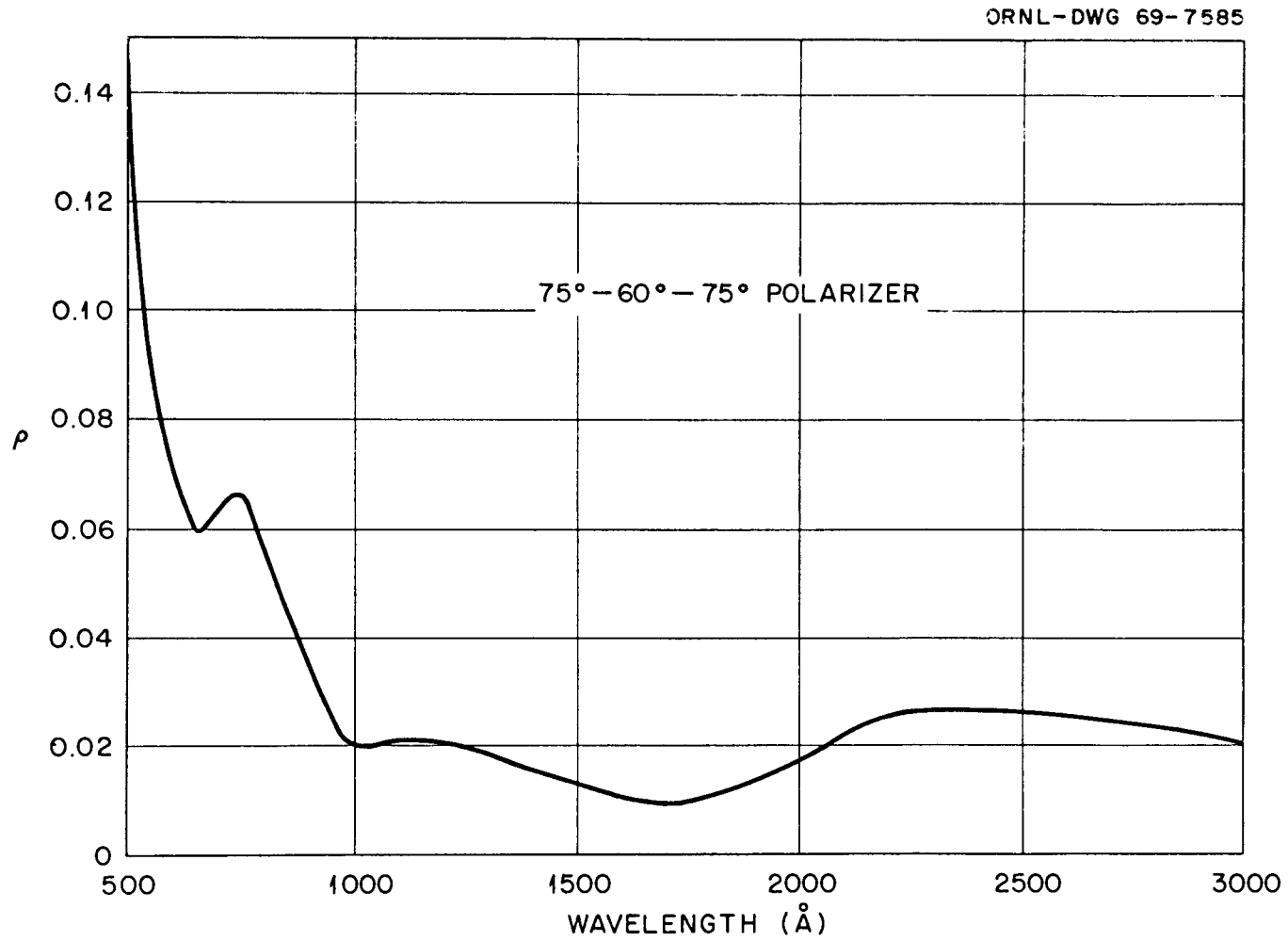

Figure 12. Polarization parameter, $\rho = r_p/r_s$, versus wavelength for triple polarizer.

III. THE REFLECTANCE CHAMBER

Once the vacuum monochromator system has been aligned the reflectance chamber can be simply bolted to the exit slit assembly. With tape baffles placed at the exit slit, the divergent beam produces a spot of light about 3 mm square at the foil holder at the center of the chamber. With a grating foil placed in this holder, a piece of sheet Polaroid could be positioned either in the entrance beam or across the one cm square opening to the phototube. Then with the incidence and diffraction angles fixed, a scan of the spectrum could be run with the grating monochromator. Usually in this region the spectral intensity was continuous so the polarizer did not have to be rotated at each measured wavelength as in the vacuum ultraviolet.

The concave diffraction grating could be observed under monochromatic light by raising the foil holder and positioning the grating at the center of the chamber and carrying out the measurements as above.

Care was taken in these measurements to use a grating for a monochromator having a different coating from the grating being investigated. This was to prevent anomalies that might be present in one from showing up in the other. For example, a 1200 line/mm gold coated grating known to exhibit no anomalies in its 1st order spectrum was always used with aluminum grating foils and aluminized concave gratings.

IV. THE VARIABLE-ANGLE APPARATUS

The procedure with this apparatus was to fix the angle 2θ between the source and the detector and scan the spectrum by varying

the angle of incidence, α , at a constant rate. The angle θ could be varied from 2 to 40 degrees.

Whenever the angle between the source and detector is changed, the grating dispersion changes accordingly, and as a result a new calibration of the grating drive register is required. With the variable-angle apparatus it was found easier to disregard the register and calibrate each spectrum directly at the time it was being run by superimposing discrete lines from a known Hg spectrum onto the grating spectrum. This was done by positioning a half-silvered mirror at the entrance slit at an angle of 45° with the optic axis so that the light from the Hg lamp positioned perpendicular to this axis could be reflected into the entrance slit. This mirror was made by vacuum evaporating different layers of Ag onto a glass slide and then using the one that resulted in diffracted Hg lines appearing with the same general magnitude as the spectra being investigated. This was effective when used with the tungsten bulb since the greater intensity of the Hg lamp could be reduced by this reflection technique. The polarization of the source light was hardly affected since the mirror (about 150 A° of Ag) transmitted over 90 per cent of this light, which was always on the optic axis. The technique was not as effective with the Xe lamp as the source, since the light from this lamp was so intense that it cracked the mirror. Calibration could be accomplished by running separate Hg and Xe spectra and also by comparing with the tungsten lamp spectra made at the same source-detector angle.

The half-angle, θ, between the source and the detector was measured by focusing the reflected (zero-order) beam first on the entrance slit and then on the exit slit and recording the angle through which the grating was rotated. This gives θ directly since rotating the grating an angle θ produces a reflected beam rotated through the source-detector angle, 2θ.

The entrance slit width could be varied by a micrometer screw attached to a slit assembly and was set at about 150 A°. The exit slit was made by tape attached directly to the window of the phototube or PbS detector and the width fixed at 150 A°. Optical alignment was accomplished by setting the source-to-grating distance at about 50 cm and moving the detector until the image was in focus. When operated at close to the Seya geometry ($\theta \approx 35°$), focusing the central image at the exit slit insured that the diffracted wavelengths, at least through the 1st order, would be in focus as well, since this is the principal advantage of this geometry. For smaller values of θ the diffracted light is in focus only over a smaller range of wavelengths [Fisher, Fujita, and Weissler (1966)], unless, of course, the detector is moved along the Rowland circle, which was not feasible to do in this experiment. A reasonable compromise was reached by using the Hg lamp and focusing on either the green line (5461 A°) or the yellow doublet (5770 A°). Since these lines are effectively in the middle of the typical wavelength region scanned (about 4000 A° to 8000 A°), the amount of defocusing at either end of the spectrum is small.

In making a spectral scan the room lights were darkened and scattered light was reduced by long tube baffles aligned along the optic axis and placed between the grating and the entrance and exit slits and covered by black cloth. The sources used in this arrangement were usually of such intensity that the background intensity from scattered light was negligible.

The Polaroid rotation apparatus could be placed in front of the tube leading either to the exit or entrance slit. To obtain the $|p - s|$ difference spectrum the Polaroid was rotated at a constant rate. To obtain the d-c spectrum, it was not rotated, but placed so that either the p- or s- polarized light would be transmitted to the detector.

In experiments where the prism monochromator was used with the Xe lamp, the grating drive mechanism was replaced with a table onto which a grating foil could be placed, and the exit slit was replaced with a one square cm opening at the detector. Both the reflected and transmitted diffracted spectra could be observed with this arrangement.

CHAPTER V

RESULTS AND DISCUSSION

In this chapter we present as a primary result of this study the dispersion curves obtained from the analysis of the anomalous peaks in the first order on-blaze spectra for the various metal and dielectric coatings on concave gratings. This is followed with results for some of the other diffracted orders, such as the zero order and 1st order off-blaze spectra, and some discussion of the intensities of the various anomalous spectra, and of the measurements with thin grating foils.

I. NON-RADIATIVE SURFACE PLASMON DISPERSION

Metal Layers on Metal Substrates - Visible and Near-Ultraviolet

The 600 line/mm concave grating blazed for 1500 A° was coated with about 300 A° of vacuum evaporated aluminum, and the spectra obtained for different values of θ for incident p-polarized light in the spectral region from 4000 to 14000 A° are shown in Figure 13. If the light is s-polarized the spectra vary smoothly with wavelength for all angles of incidence. The same results are obtained if the polarizer is placed in the exit beam, but this is to be expected since the p- and s- components of light reflected from a metal surface are not changed in magnitude and are changed in phase only if incident plane-polarized light is oblique to the plane of incidence [Jenkins and White (1957)]. Note that the anomalous polarization peaks evident in Figure 13 appear

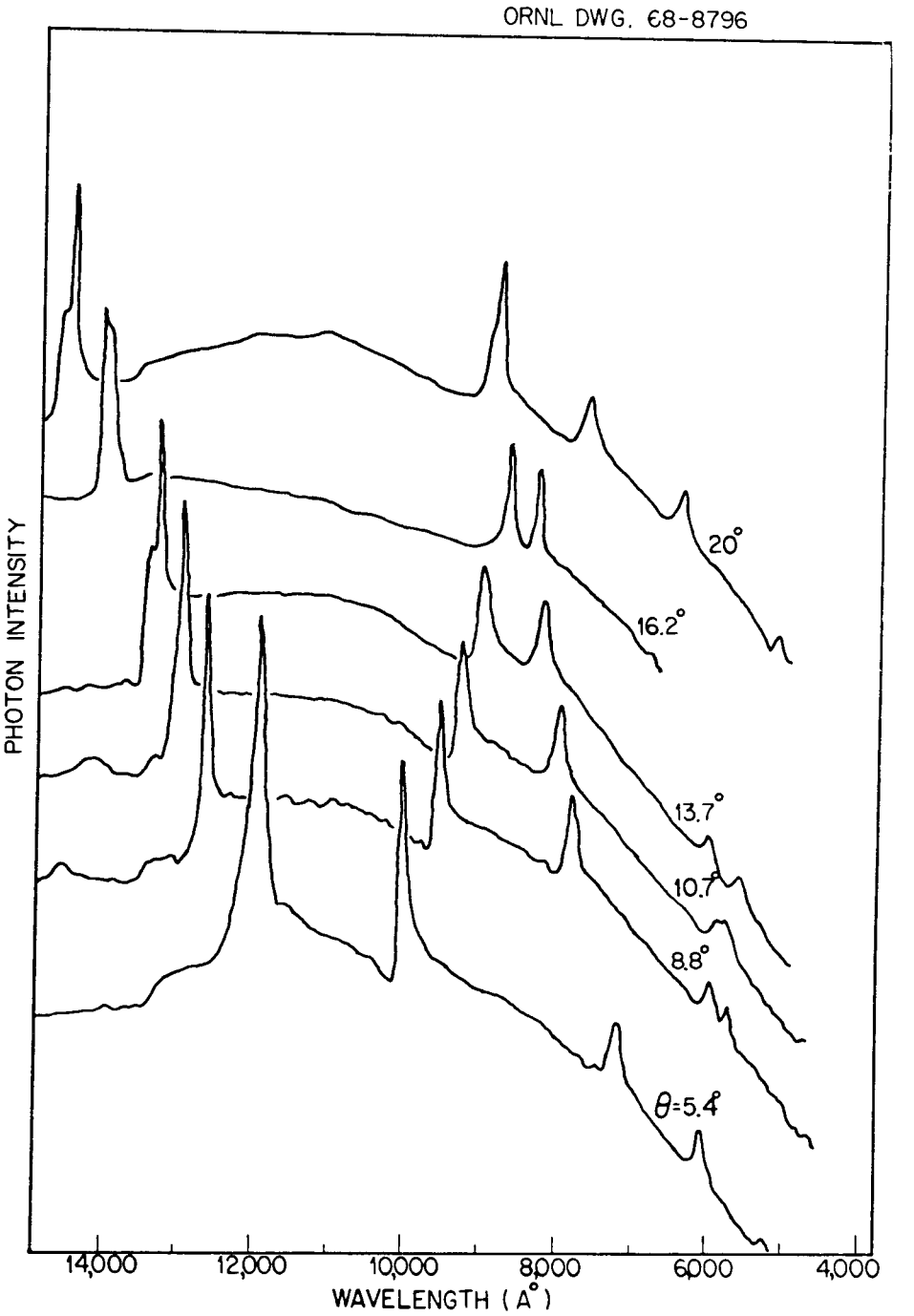

Figure 13. Anomalous polarization peaks in p-polarized spectra for Al-coated grating.

to change in wavelength in a regular fashion as θ is changed. A quantitative knowledge of this dependence can be gained by plotting the photon energy corresponding to the wavelength at the center of an anomalous peak as a function of angle θ as in Figure 14. One sees from this figure that definite branches appear to be formed in the data suggesting a functional relationship between angle and energy. Also included in this figure are data taken in exactly the same manner after 500 A° of gold had been vacuum evaporated over the aluminum layer. Similar branching behavior is seen here too except that corresponding branches are shifted to lower energies in the short wavelength region. One notes also that where a branch sloping to the left approaches one sloping to the right, the two branches appear to "repel" each other instead of intersecting. This behavior is more apparent for gold than for aluminum. These gaps in the energy-angle plot are comparable to similar observations made by Stewart and Galloway (1962) in their studies of the zero-order spectra with aluminized gratings. We see also that a gap between two branches at a small value of θ is found at exactly the same photon energy as a second gap between two different branches at a larger value of θ.

To construct the dispersion curve from the data of Figure 14, we utilize the dispersion relation, Equation (93)

$$\kappa_n = \frac{\pi}{\delta}(2n + 1) + \frac{E}{\hbar c} \sin\theta \sqrt{1 - \left(\frac{\pi c\hbar}{\delta E \cos\theta}\right)^2}$$

where the frequency is expressed in terms of the photon energy, $E = \hbar\omega$,

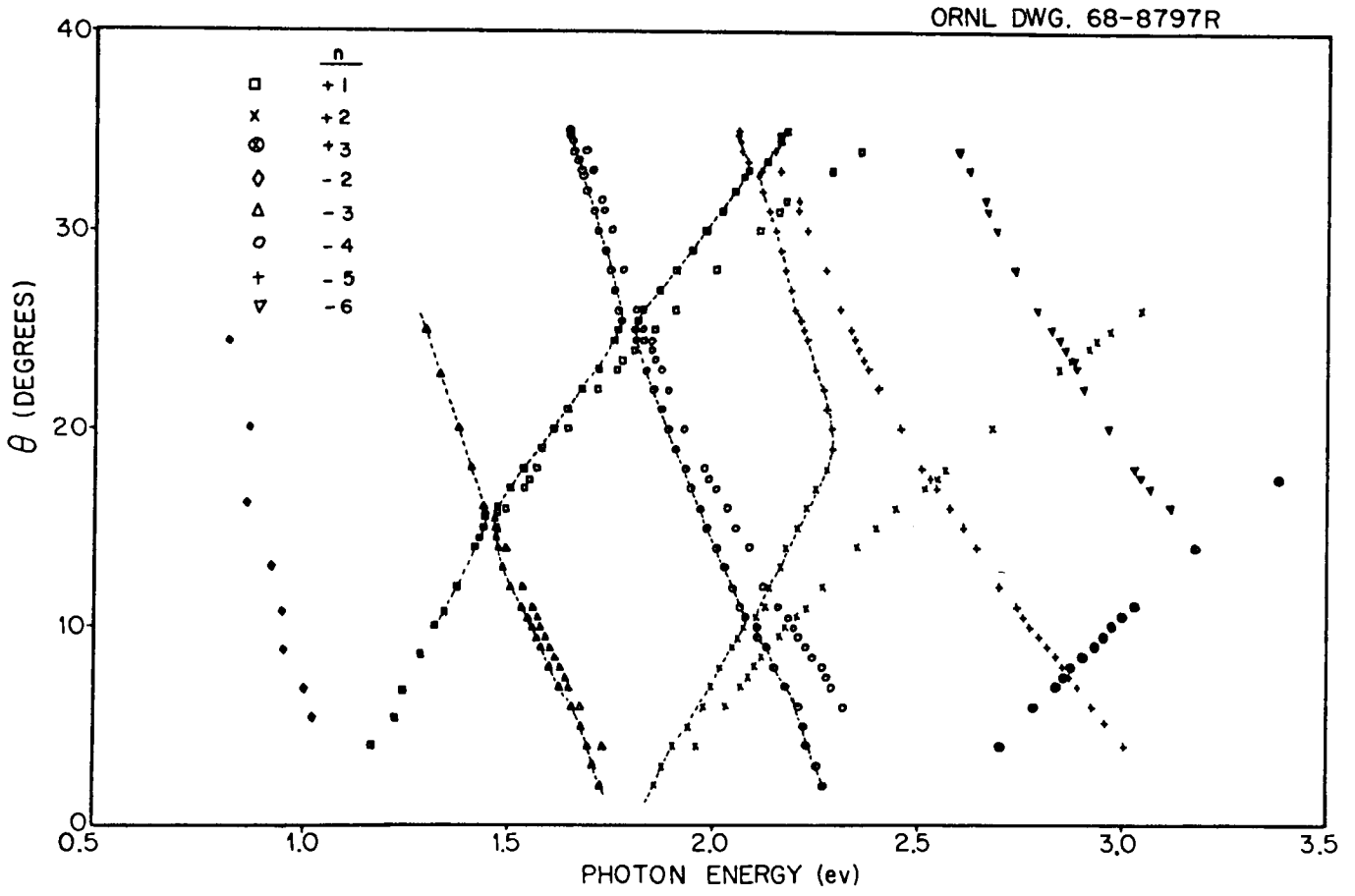

Figure 14. Photon energy of anomalous peaks versus half-angle, θ , between source and detector for Au (dotted lines) and Al (no dotted lines) layers on grating surface.

and the order of the diffracted light, n', is given the value +1. This is because in the variable-angle apparatus the 1st order diffracted beam we are investigating is between the reflected and incident beams. Since the photon energy, $\hbar\omega$, is equal to the surface plasmon energy, $\hbar\Omega$, at resonance (Equation (91), the surface plasmon dispersion curve is obtained by evaluating $|\kappa_n|$ as a function of the photon energy. For a given point in the experimental data, the angle, θ, the photon energy, $\hbar\omega$, and the grating spacing, δ, are known, and only n needs to be determined. This is done by assuming a positive or negative value for n, solving for κ_n and then finding the best fit of $|\kappa_n|$ to the dispersion curve, which, for example, in the low frequency region we expect to be very close to the light line. It is found that each n value corresponds to a given branch of the experimental data of Figure 14, the positive values being for branches sloping to the right and negative values for those sloping to the left, the higher n values being found for higher energy photons. Once an n for a given branch is found, the others follow in sequence. These assignments are shown by the symbols on the figure.

Figure 15 shows the anomalous spectra at selected values of θ when the same grating had been coated with an additional layer of silver (~500 A° in thickness). The relationship between photon energy and angle is given in Figure 16 and the aluminum data of Figure 14 are included for comparison. One notes the same general behavior as in Figure 14 except that the peaks for silver are not shifted toward lower energies to the same degree as are those for gold.

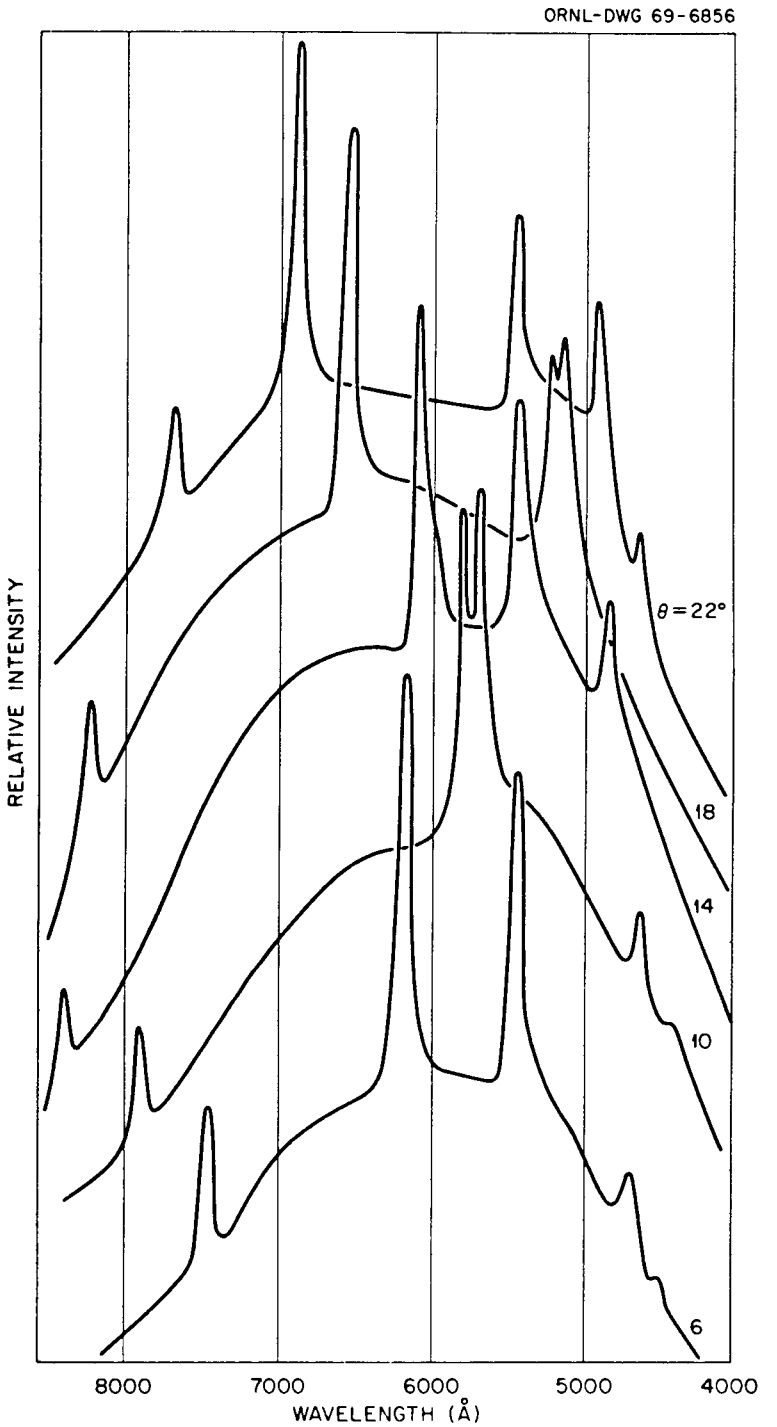

Figure 15. Anomalous polarization peaks in |p - s| difference spectra for Ag-coated concave grating.

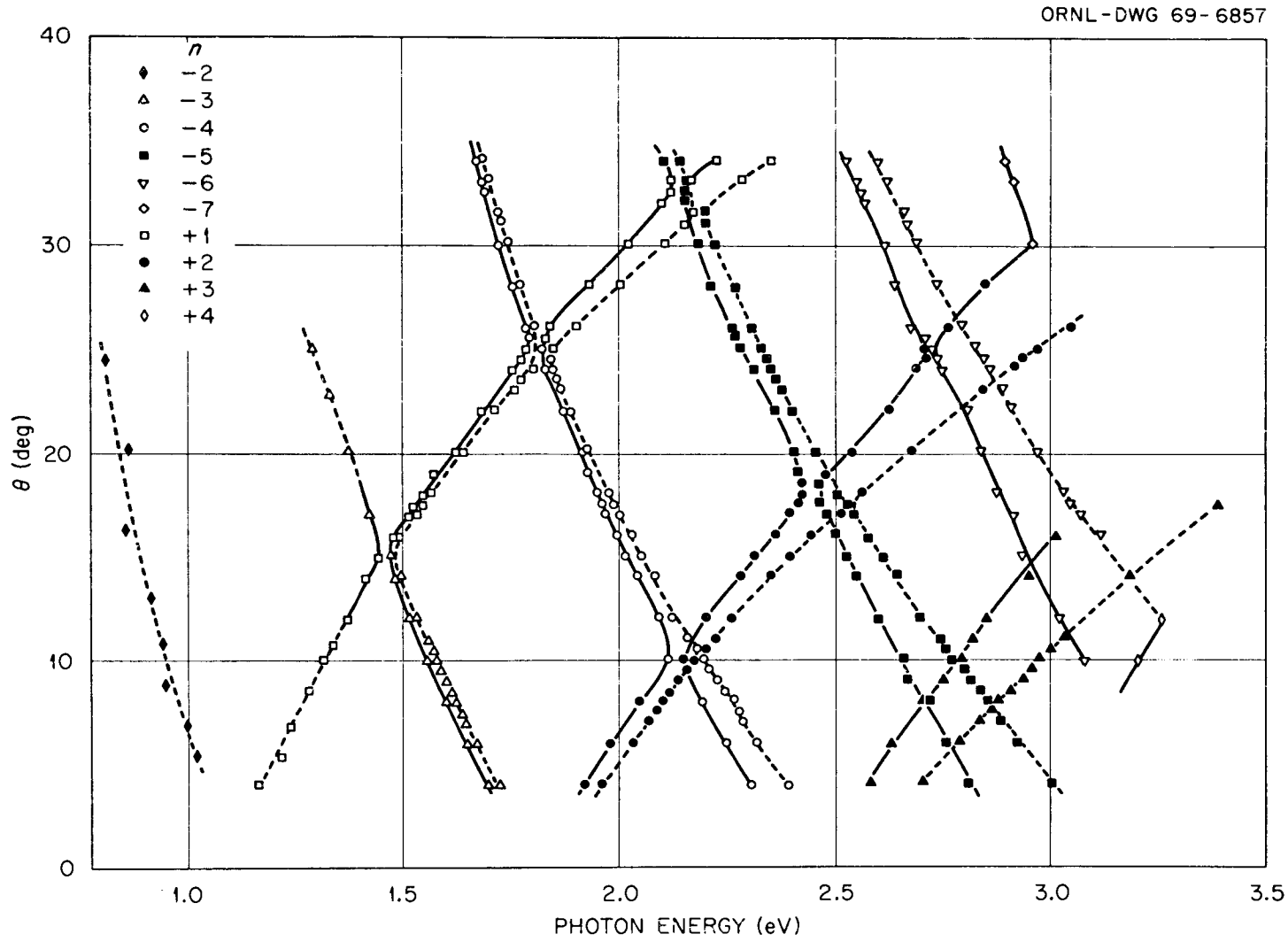

Figure 16. Photon energy of anomalous peaks versus half-angle, θ , between source and detector for Ag (solid lines) and Al (dotted lines) layers on grating surface.

Equation (93) was evaluated for each of the experimental points in Figures 14, page 114, and 16 using the proper n value for each, and the resulting dispersion curves for Al, Ag, and Au are given in Figure 17. The Feynman diagram for this process is also included. Note that the parameters n' and k' for the diffracted beam have not entered directly into the calculations, but they are implicitly related to n and k through the diffraction equation. The dotted lines in Figure 17 are the classical dispersion curves obtained from Equation (41) for a surface plasma wave propagating at a metal-vacuum interface using $\varepsilon(\omega) = \varepsilon_1 = n^2 - k^2$, the real part of the dielectric constants of Al, Au, and Ag from the data of Ehrenreich , Philipp, and Segall (1963), Schultz (1954), and Schultz and Tangherlini (1954), where n is the index of refraction and k is the extinction coefficient. The agreement is seen to be excellent for all values except for slight deviations for Al at higher energies. It is shown later in this chapter that this can be explained by the oxide layer that forms on Al and not on the other two metals.

These curves should approach ideally the surface plasma wavelengths for these metals, which for Al, Ag, and Au are 1170 A° (10.5 ev), 3500 A° (3.54 ev), and 5500 A° (2.25 ev), respectively. In the region studied here above 2700 A°, it was found that the higher energy peaks for Ag and Au decreased in intensity and became broader. This is to be expected since the imaginary part, ε_2 , of the dielectric constant of these metals, while small, does increase with respect to ε_1 as the

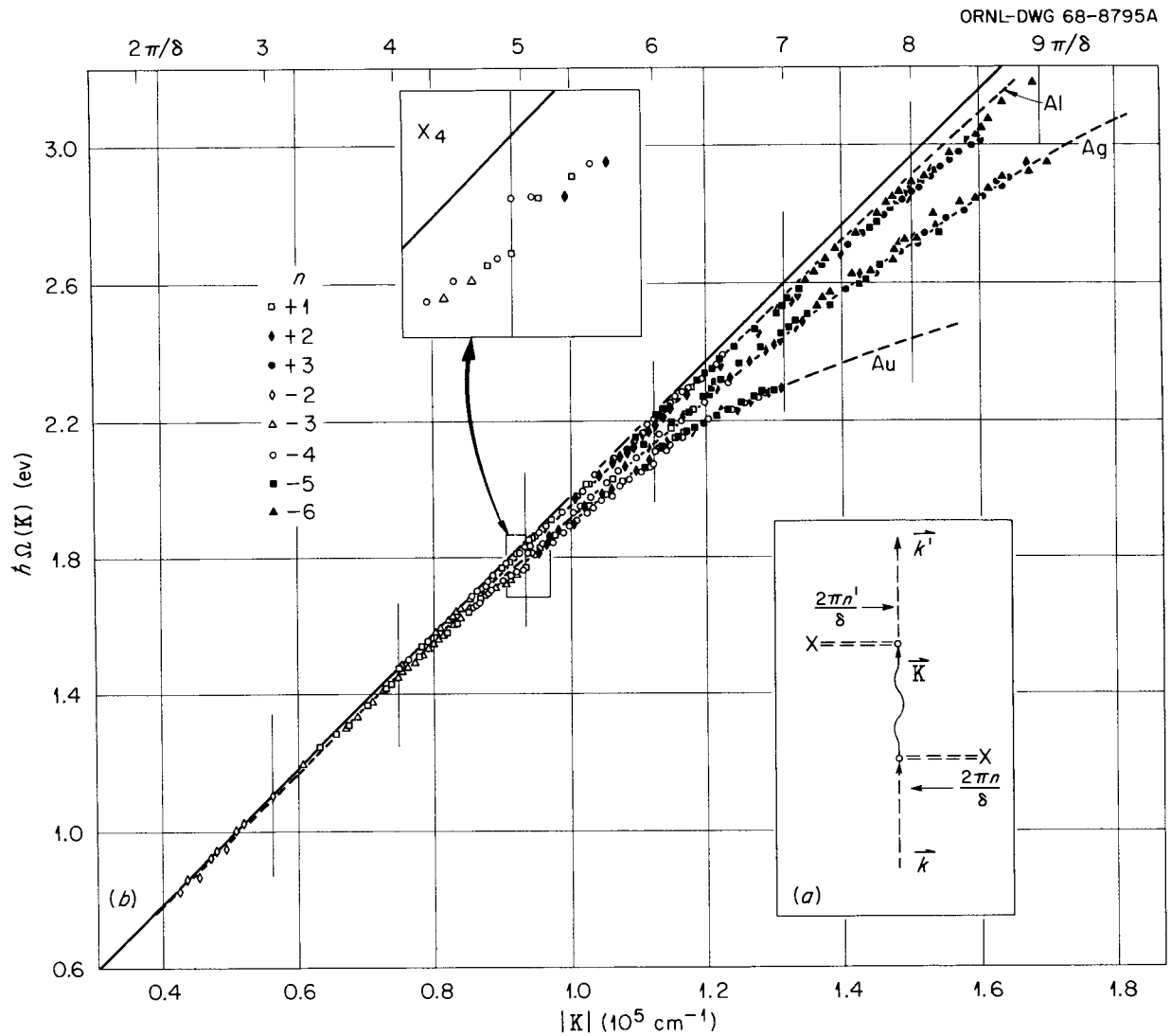

Figure 17. (a) Feynman diagram for photon - non-radiative surface plasmon interaction (b) surface plasmon dispersion relation for Al, Ag, and Au coatings on grating. Dotted lines - theoretical curves.

energy is increased. It is however small enough so that one is still justified in using only ε_1 in Equation (41) to obtain the classical dispersion curve.

A feature noted on the experimental dispersion curves is the discontinuity that appears at multiples of π/δ . This is in accordance with the self-energy picture of the surface plasmon developed in Chapter II. These gaps result from the regular grating structure and, of course, are not predicted by the classical dispersion theory, which applies only to surface plasma wave propagation on a flat surface. The gaps correspond to the gaps in Figures 14, page 114, and 16, page 117, where a branch having a positive value of n makes its closest approach to one having a negative n value. We may qualitatively regard the phenomenon here as the interaction of surface plasmons having the same momentum but propagating in opposite directions and forming standing waves in the periodic electronic density of the grating surface. This is analogous to the well-known formation of Brillouin zone gaps in crystalline solids [Kittel (1966)].

To gain a clearer understanding of the meaning of the n values, it is instructive to see the relationship of the anomalous polarization peaks to the Rayleigh wavelengths. For example, at $\theta = 20^\circ$ the anomalous wavelengths for the Al-coated grating appeared at the values shown in Table I. The diffraction order was $n' = +1$, and the angle of incidence, α , was calculated from Equation (92). The values of the passing-off diffraction order, m , were obtained from the Rayleigh

Table I. Anomalous wavelengths for $\theta = 20°$. Rayleigh passing-off orders, m, are compared with branch values, n

n'	λ(A)	E(ev)	α(°)	$m=\delta(\sin\alpha + 1)/\lambda$	n	$m=\delta(\sin\alpha - 1)/\lambda$	n
+1	4180	2.97	27.7	5.84	-6	-2.13	
	4630	2.68	28.5	5.31		-1.93	+2
	5050	2.46	29.3	4.92	-5	-1.68	
	6430	1.93	31.8	3.97	-4	-1.22	
	7750	1.60	33.9	3.44		-0.98	+1
-1	4180		12.3	4.84	-5	-3.14	
	4630		11.5	4.32		-2.88	+3
	5050	"	10.7	3.92	-4	-2.68	
	6430		8.2	2.97	-3	-2.22	
	7750		6.1	2.45		-1.99	+2

wavelength equation, (1), $m = \delta(\sin\alpha \pm 1)/\lambda$ and are given in the table. In the last column of this table are the values of n obtained by the method described previously. One sees that to the nearest whole number, the m and n values agree except that the sign is different. This is in agreement with the sign convention that has been adopted, because a negative m value is for a diffracted order moving across the grating in essentially the same direction as the incident light, while a positive n value applies to momentum transfer also in the same direction as the incident light [Equation (90)]. Positive m and negative n values, conversely, are for motion in the opposite direction. The larger the order number, n, the larger are the number of grooves participating in the momentum transfer process.

If we observe the 1st order diffracted light on the opposite side of the reflected beam, so that the reflected beam is between the incident and diffracted beams, the order number, n', is -1. This changes the first term in Equation (93) from $2n + 1$ to $2n - 1$. The anomalous peaks appear at the same wavelengths but at different angles of incidence, as calculated from Equation (92). This gives m values that are changed in magnitude by unity, but as it turns out, the n values, in being fit to the dispersion curve, are also changed by the same amount. This is evident from Table I. Table II shows the calculations for $|\kappa_n|$ for this grating also at $\theta = 20°$.

We expect the anomalies to occur near the Rayleigh wavelengths as long as the dispersion curve is near the light line, as we have here,

Table II. Calculation of $|\kappa_n|$ for $\theta = 20°$ using anomalous wavelengths and Equation (93)

n'	λ(A)	E(ev)	n	$(\pi/\delta)(2n+1)$	$\frac{E}{\hbar c}\sin\theta\sqrt{1-(\frac{\pi\hbar c}{E\cos\theta})^2}$	$\lvert\kappa_n\rvert(10^5\ cm^{-1})$
+1	4180	2.97	-6	-2.0745	.5105	1.5630
	4630	2.68	+2	+ .9425	.4599	1.4024
	5050	2.46	-5	-1.6965	.4208	1.2757
	6430	1.93	-4	-1.3195	.3275	.9920
	7750	1.60	+1	+ .5655	.2706	.8361

but discrepancies are expected for low velocity surface plasmons described by a dispersion curve far removed from this line.

The validity of Equation (41) in calculating the dispersion curves of Ag and Au may be questioned since it applies to wave propagation on a semi-infinite metal surface, while in reality the metals were only a few hundred A° thick on an effectively semi-infinite Al substrate. This could be checked from Equation (50), which is the dispersion relation for a dielectric layer on a metal substrate, by substituting the real part of the dielectric constant of either Ag or Au in place of that of the dielectric and using ε_1 of Al for the substrate. With these dielectric constants, Equation (50) becomes the dispersion relation for a metal layer bounded on one side by a metal substrate and on the other by vacuum and solutions are obtained for the normal and tangential modes. The equation was solved on the CDC 1604-A computer and the results of the tangential mode solution for a few selected thicknesses are shown in Figure 18. It can be seen that significant deviations from the semi-infinite curves occur only for very thin layers, and that there is essentially no difference for the 500 to 600 A° layer thicknesses that were used in this experiment.

The validity of Equation (93) may also be questioned since the square root term becomes imaginary whenever $\delta \hbar\omega \cos\theta < \pi c\hbar$, or in terms of photon energy, whenever $\hbar\omega$ (ev) $< .371/\cos\theta$. Considering an extreme case where $\theta = 45°$, we obtain $\hbar\omega < .525$ ev. Since in this experiment the photon energy was never less than 0.8 ev, no difficulties were encountered in using this equation.

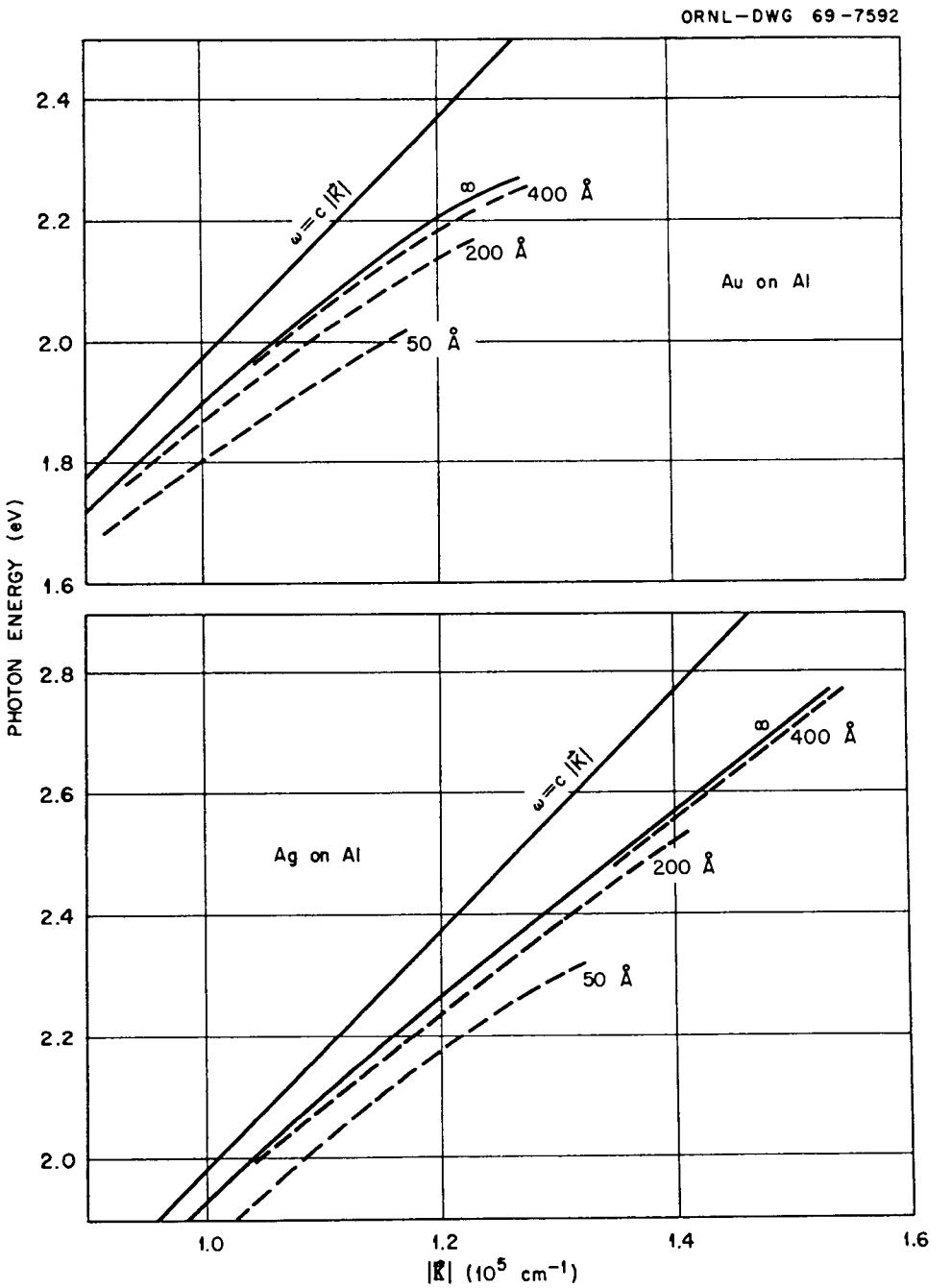

Figure 18. Theoretical tangential mode surface plasmon dispersion curves for various thicknesses of Al and Au on an Al substrate.

Dielectric Layers on Aluminum Substrates - Visible and Near Ultraviolet Regions, Al_2O_3 and Diffusion Pump Oil

The theoretical dispersion curve obtained in the previous section for aluminum is for the ideal case of a pure metal surface. In reality an oxide layer several A° thick forms naturally on aluminum and the thickness of this layer depends on the smoothness and purity of the substrate. For example, Berning, Hass, and Madden (1960) report that with 99.99 per cent pure Al layers 500 to 600 A° thick vacuum evaporated in 1 to 2 sec, the oxide film formed after one hour is 10-12 A° thick, reaches 15 A° after 1 day, about 20 A° after 10 days, and a maximum of 22 A° after one month, after which any further growth ceases. Walkenhorst (1941), and Hass (1947) on the other hand, report maximum oxide thicknesses of 40 A° or more forming on thick, vacuum evaporated Al layers after about a month's exposure to air. Berning, Hass and Madden attribute the difference to the fact that they used super-pure aluminum and faster evaporation times which reduced aggregation and formed smoother films.

Because concave gratings are often operated in the vacuum system for weeks and months, molecular layers of diffusion pump oil can adhere to the grating surface. This was not the case for the grating (B and L No. 2243-32) investigated in the previous section, since it was exposed to air within hours after the evaporation. Other gratings, however, had to be analyzed for this additional dielectric layer.

The effects of the dielectrics on aluminum substrates were investigated in several different ways; one, by cleaning and evaporating

new layers onto the surface, two, by anodizing additional oxide layers, and three, by analyzing the dispersion properties of the naturally formed layers.

Grating 2243-32 was coated with 200 A° of aluminum (evaporation time = 2 sec) and measurements taken in the vacuum monochromator immediately after evaporation and later after exposure to air at atmospheric pressure. The results are shown in Table III where the first column gives the anomalous wavelengths for the freshly evaporated layer at a pressure of 10^{-6} Torr and the second after exposure to air for 10 hours, A definite shift to longer wavelengths is noted for the exposed surface and is attributed to the formation of an oxide layer.

The original aluminized surface of a second grating (B and L No. 2406-22-1-5) that had been operated in the vacuum system for seven months was also analyzed for anomalous wavelengths, and the results after two months exposure are shown in Figure 19. This shift is believed due entirely to pump oil because this surface had been exposed to air for almost two months before being installed in the vacuum system. Two verifying experiments were made: (1) when the edge of the grating not normally exposed to the incident beam in the monochromator was cleaned by the process mentioned in Chapter III, the anomalous peaks shifted back to the values they would have had for the normal oxide layer. The edge was used here because Berning, Hass, and Madden have shown that direct ultraviolet radiation on an aluminum surface can increase the natural oxide thickness by as much as 15 A°; (2) coating the uncleaned

Table III. Wavelengths of anomalous peaks at $\theta = 35^{\circ}$ for a layer of Al: (a) freshly vacuum-evaporated at 10^{-6} Torr; (b) the same layer exposed to air for 10 hours

Vacuum	Exposed to Air
5826	5863
4823	4843
4107	4132

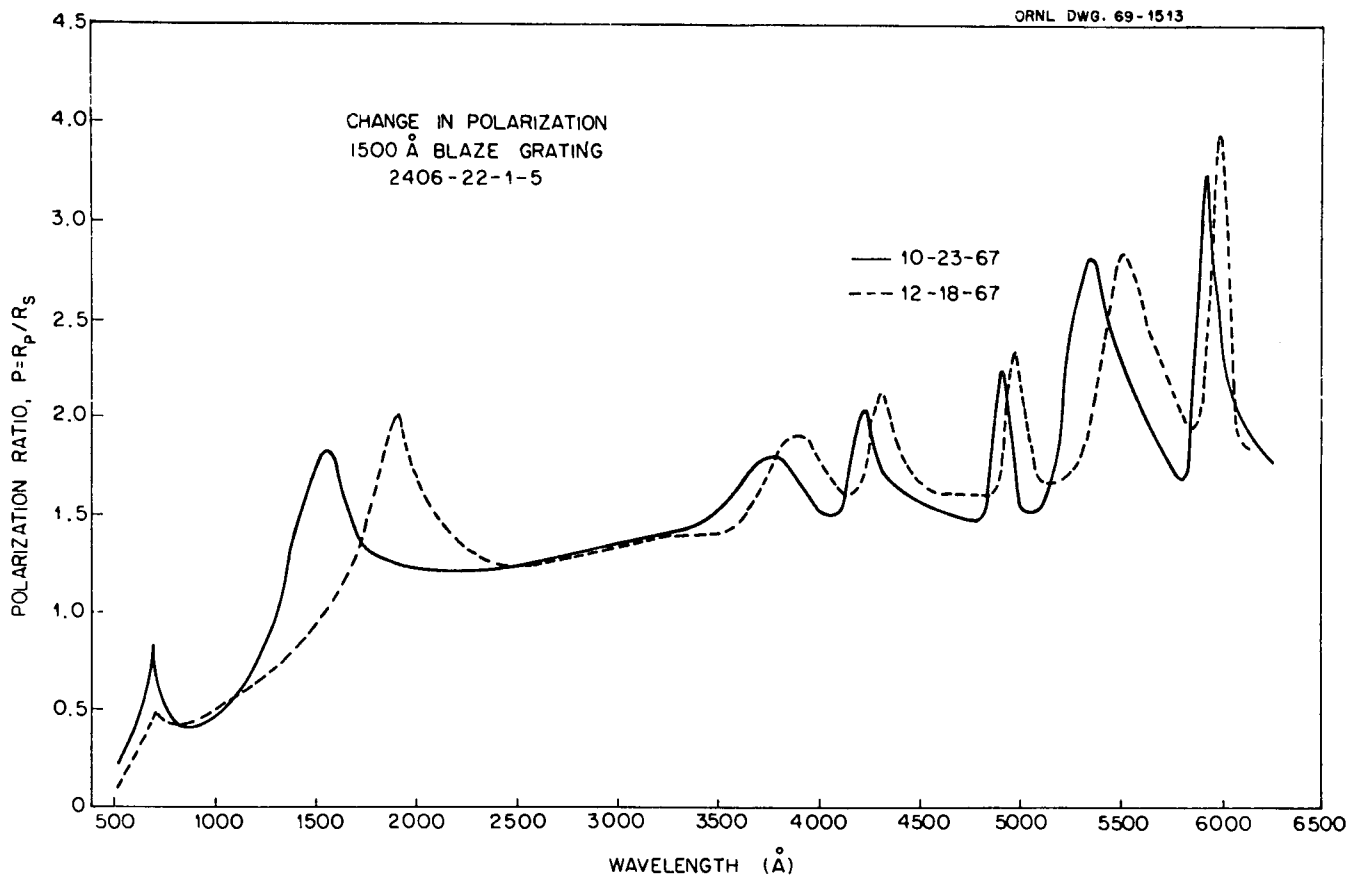

Figure 19. Anomalous polarization peaks for concave grating after two month exposure in vacuum system.

surface with a vacuum evaporated layer of Al (600 A°) and exposing to air for 24 hours produced a shift to wavelengths characteristic of the oxide layer (Table IV).

The same grating (2406-22-1-5) was subjected to further study by anodizing additional oxide layers with the anodic oxide apparatus described previously. With θ fixed at 25.7° one edge of the grating constituting one-third of the total grating surface was cleaned and oxide layers were obtained for 6 v. (75 A°), 9 v. (125 A°), 18 v. (243 A°), 40 v. (540 A°), and 60 v. (810 A°). The measured shift of the anomalous polarization peaks to longer wavelengths for some of these thicknesses are shown in Figure 20. The opposite edge was then anodized at 40 v. (540 A°) with θ again fixed at 25.7°. A final anodization was done, also at 40 v., on the center section, but at several different values of θ. All of the anomalous wavelengths obtained were evaluated by Equation (93), and the resulting points in the dispersion diagram are shown in Figure 21. The solid lines are theoretical dispersion curves obtained from Equations (52) and (53). Since the extinction coefficient of Al_2O_3 is effectively zero in this wavelength region, $\eta(\omega) \approx \eta_1 = n^2$, where the index of refraction, n, for anodized Al_2O_3 ranges from 1.62 at 6000 A° to 1.67 at 3000 A° [Hass (1949)]. We also use in these equations $\varepsilon(\omega) = \varepsilon_1$, the real part of the dielectric constant of Al.

That there are discrepancies between theory and experiment is evident from Figure 21, and could be due to several factors: (1) The relation between thickness and voltage, which was derived for a flat

Table IV. Wavelengths of anomalous peaks at $\theta = 25.7°$ for an Al-coated grating (a) used in a monochromator for seven months and coated with diffusion oil; (b) same surface with the oil removed; (c) the surface coated with 600 A° Al and exposed to air for 24 hours

Oil	Cleaned	Al(600 A°)
4530	4480	4480
5450	5400	5400
6670	6580	6550
6940	6870	6870

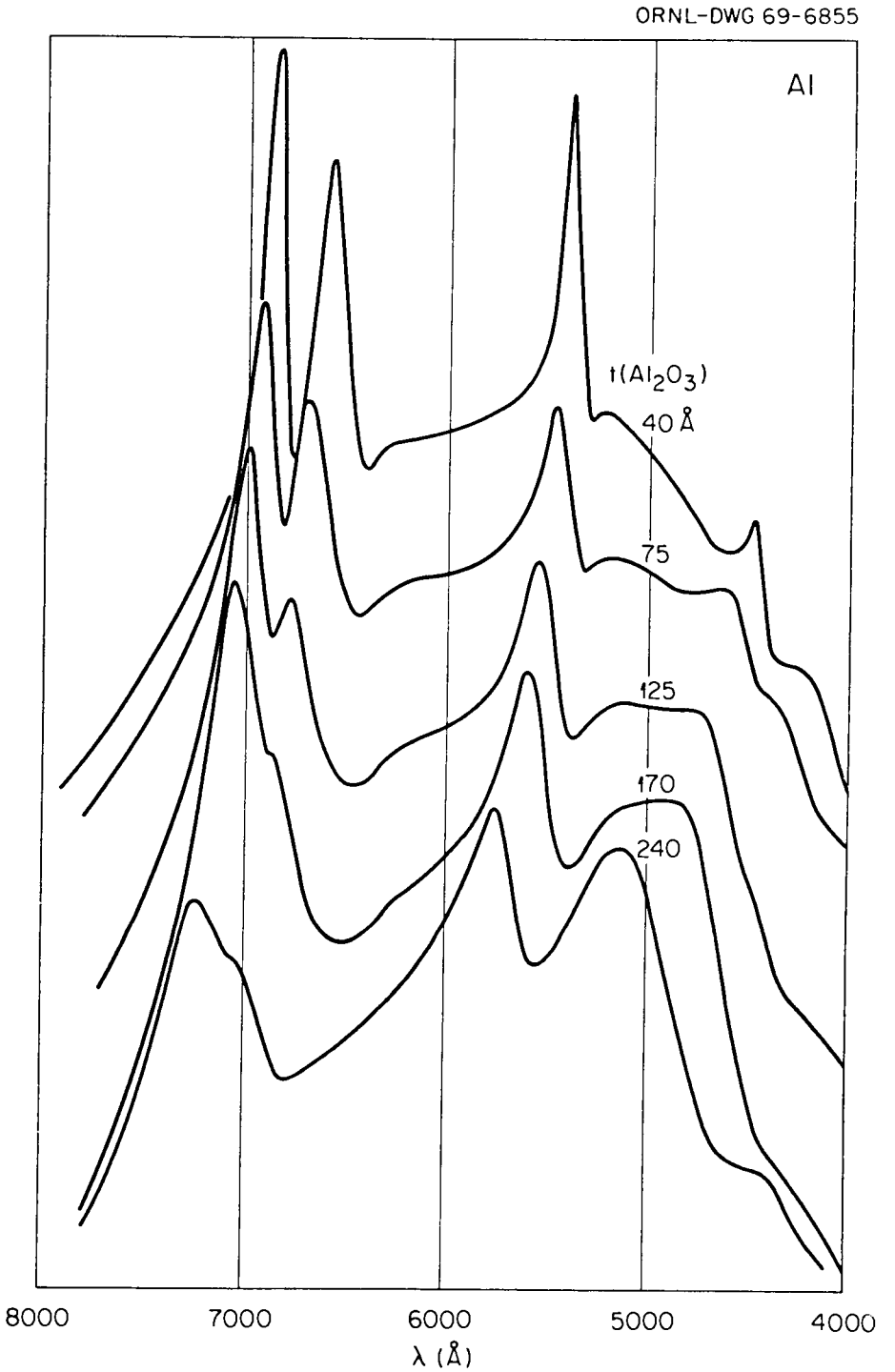

Figure 20. Anomalous polarization peaks for Al (grating) substrate coated with various thicknesses of anodized Al_2O_3.

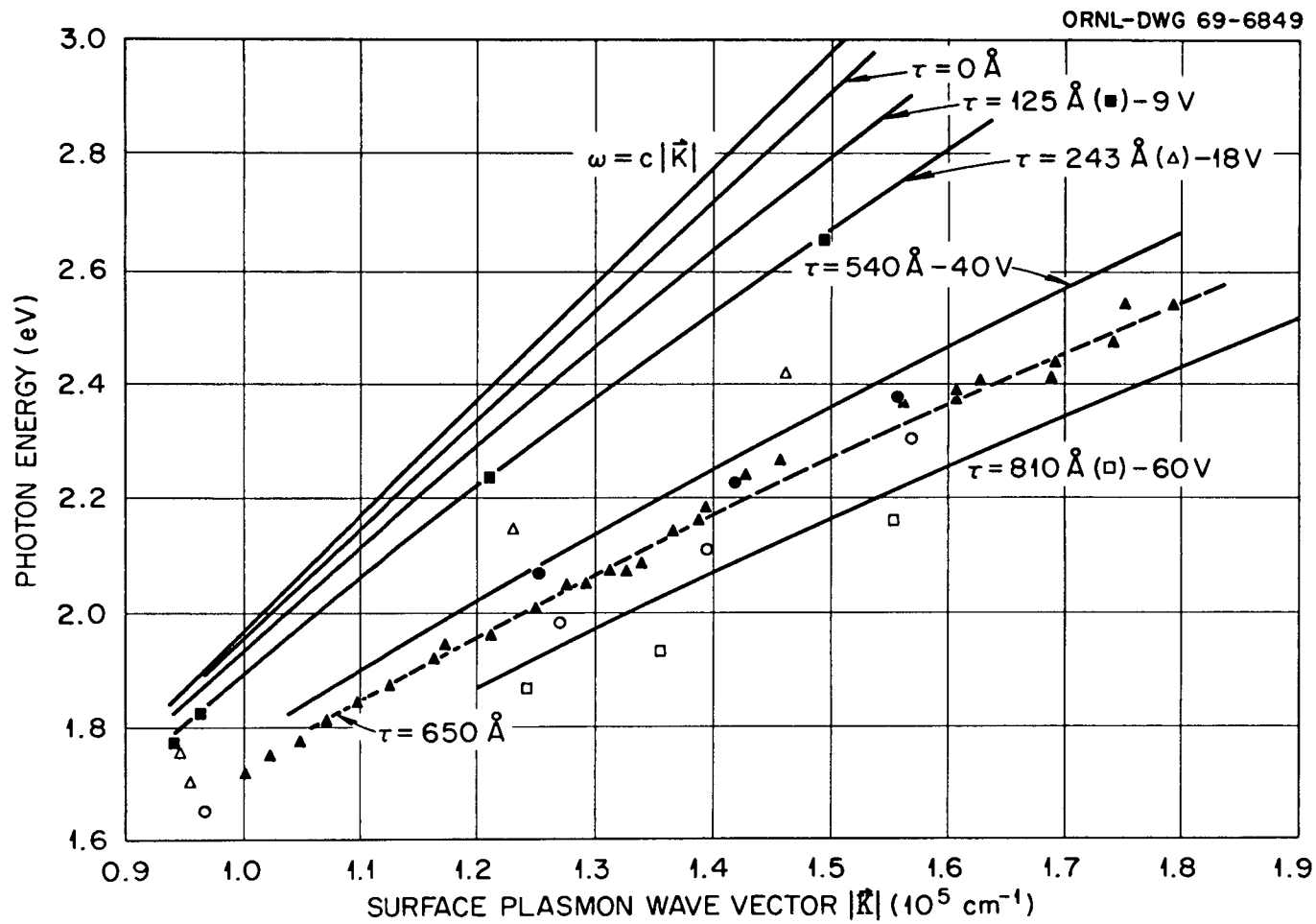

Figure 21. Surface plasmon dispersion curves for different anodized Al_2O_3 thicknesses on concave grating. ● - left edge, 0 - right edge, ▲ - center.

surface, might be different for a grating surface, (2) The polarization peaks for anodized surfaces are broader and not as well-defined as for the unanodized case, thus introducing an error in reading the wavelengths, (3) The voltage-thickness curve itself may be in error (see Chapter IV), and (4) Equal voltages applied to similar grating surfaces might not always produce the same thicknesses. One notes, for example, the large spread in values, all obtained at the same voltage, for three sections of the same grating. Equally evident is the spread in values that were obtained with the center section alone. The dotted line is the theoretical curve that appears to match these values the best, and is for a thickness of 650 A°. We further observe, however, that some points of the center section, and notably those from the second edge of the grating to be anodized, are very close to the original value of 540 A°.

When Equations (52) and (53) were applied to the experimental dispersion curve obtained earlier with grating 2243-32 (Figure 17, page 119), a very good fit was obtained assuming an oxide thickness of 50 A°. Since the substrate could not be made perfectly clean because of the difficulties mentioned earlier, the evaporated Al layer may have had more surface roughness than a layer prepared under more ideal conditions, and thus a 50 A° thickness seems reasonable.

The original aluminized surface of the other grating (2406-22-1-5), being prepared under more exacting conditions, was assumed to have developed an oxide layer of only 20 A° after long exposure to air. The experimentally determined dispersion curve for this grating after

several weeks exposure in the vacuum system was very similar to that obtained above for grating 2243-32. One finds that the theoretical curve giving the best fit in this case is for an assumed oil thickness of 20 A° on top of the 20 A° oxide layer using Equations (63) - (66) for a double dielectric layer on a metal substrate. This, as well as all subsequent dispersion curves discussed in this work, was evaluated on the CDC 1604-A computer. We use here the optical constants of anodized Al_2O_3 as above. Those for the pump oil (DC-705) were obtained from reflectance measurements made in this laboratory. For wavelengths greater than 2400 A°, the extinction coefficient, k, is zero, and the index of refraction, n, can be taken as constant at $n = 1.74$. The pump oil used in our vacuum system was DC-706, but the difference in the optical constants between this and DC-704 are not believed appreciable. However, there may be some variation due to the fact that these are bulk values rather than those for thin films.

Magnesium Fluoride

A third Bausch and Lomb concave grating was analyzed that had the same line spacing and blaze (600 lines/mm; 1500 A° blaze) as the other two, but with its aluminum substrate coated with 350 A° of MgF_2. (This thickness value was verified by personal correspondence with the Bausch and Lomb Corp.) A typical spectrum of the $|p-s|$ difference signal extended into the near ultraviolet is shown in Figure 22. Note that the anomalous peaks get closer together, appearing to approach a continuum as expected, and also less intense and broader. The photon

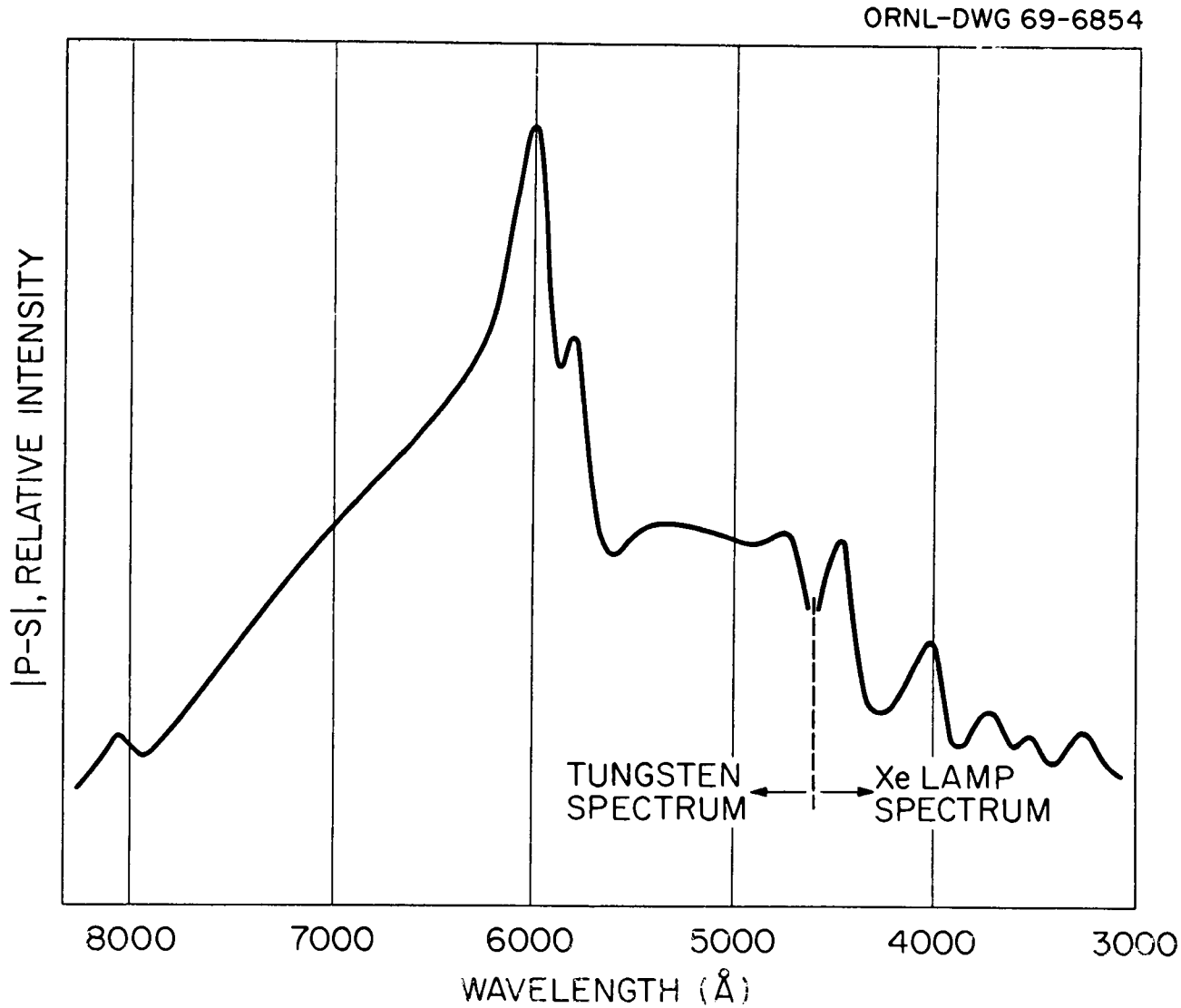

Figure 22. Anomalous polarization peaks in |p - s| difference spectra for 350 A° MgF_2-coated concave grating.

energy at which the peaks occur as a function of angle θ is given in Figure 23 where it can be seen that the gap spacing is larger than for the other aluminized grating that was uncoated. That this could be due to the dielectric alone is not conclusive, however, since two different gratings are involved. The gold data obtained previously is included for comparison, and one can see the similarity between the gap spacing for the two different coatings. That this might be due to both dispersion curves being farther removed from the light line than those for either pure Al or Ag is also questionable, since here, again, two different gratings are involved.

The experimental dispersion curve obtained from Equation (93) for the MgF_2 coated grating is given in Figure 24. The dotted line is Equation (52) and (53) using $\eta(\omega) = \eta_1 = n^2$, where here, the extinction coefficient, k, is effectively zero, and the index of refraction, n, for MgF_2 varies from 1.382 at 7000 A° to 1.390 at 4000 A° [Duncanson and Stevenson (1958)]. The Al data are also included in Figure 24. Note that there is excellent agreement between theory and experiment.

Dielectric Layers on Metal Substrates-Vacuum Ultraviolet Region

Time studies of the polarization ratio (R_p/R_s) were made in the vacuum ultraviolet with the aluminized grating 2243-32 after vacuum evaporating layers of aluminum, silver, and gold. The results are given in Figure 25. Note that the peak appearing at 1580 A° for a layer of aluminum (115 A°) decreases only slightly after remaining in vacuum (10-6 Torr) for several days, but after exposure to air for a few hours

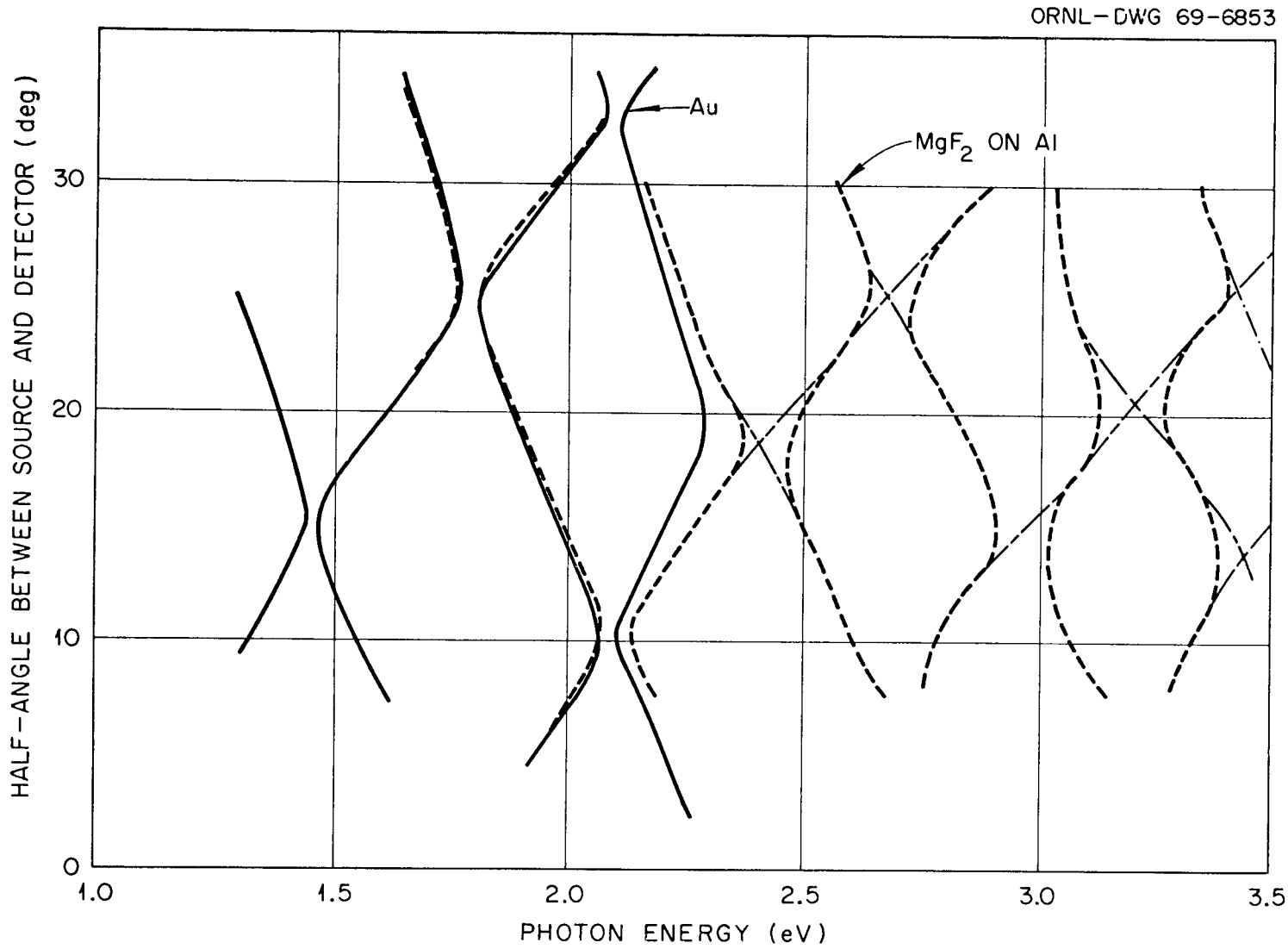

Figure 23. Energy of anomalous peaks versus angle. Solid lines, Au; dotted lines, MgF_2.

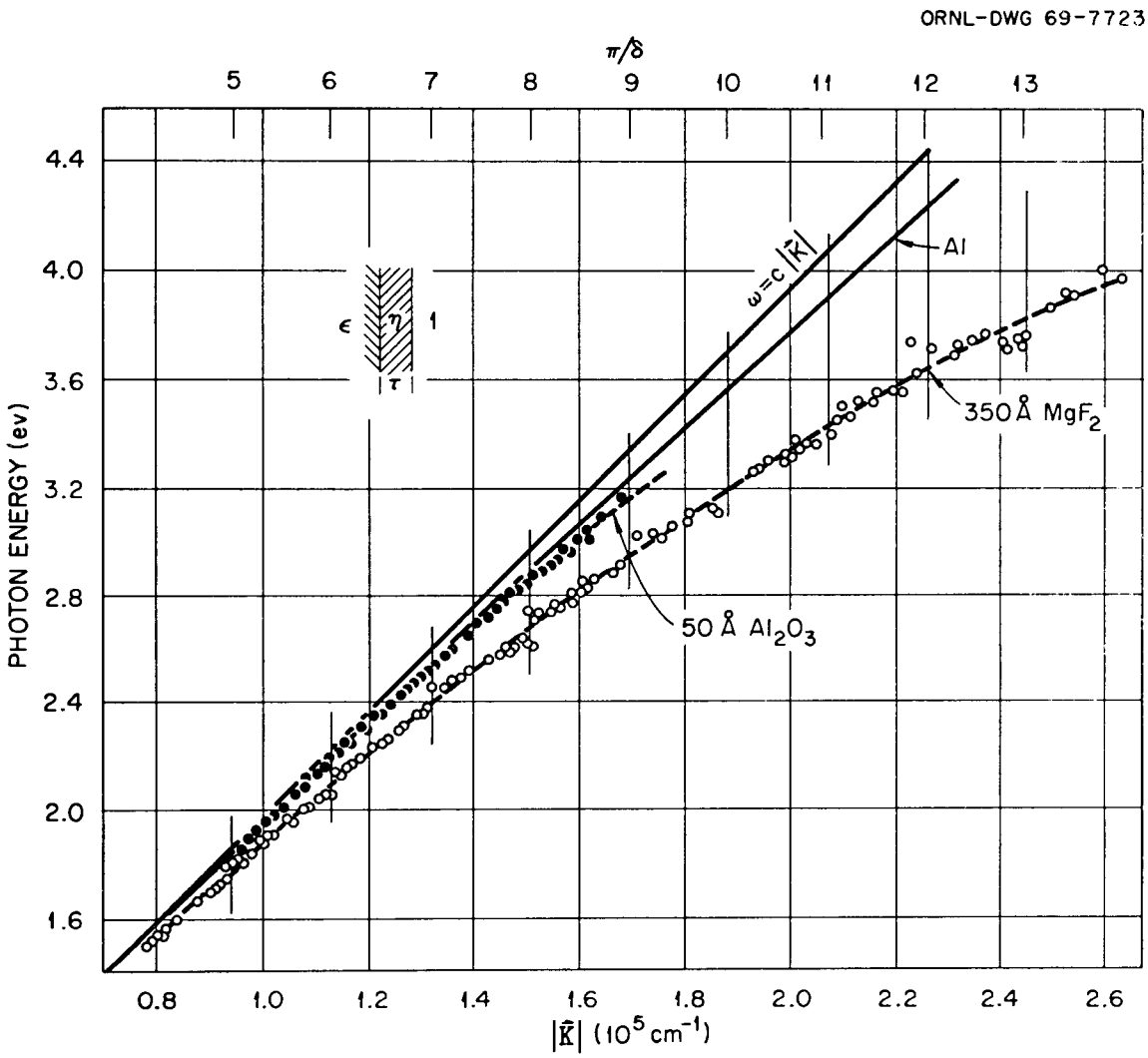

Figure 24. Surface plasmon dispersion curves for (a) 50 A° Al_2O_3 and (b) 350 A° MgF_2 on Al substrate. Dotted lines - theoretical curves.

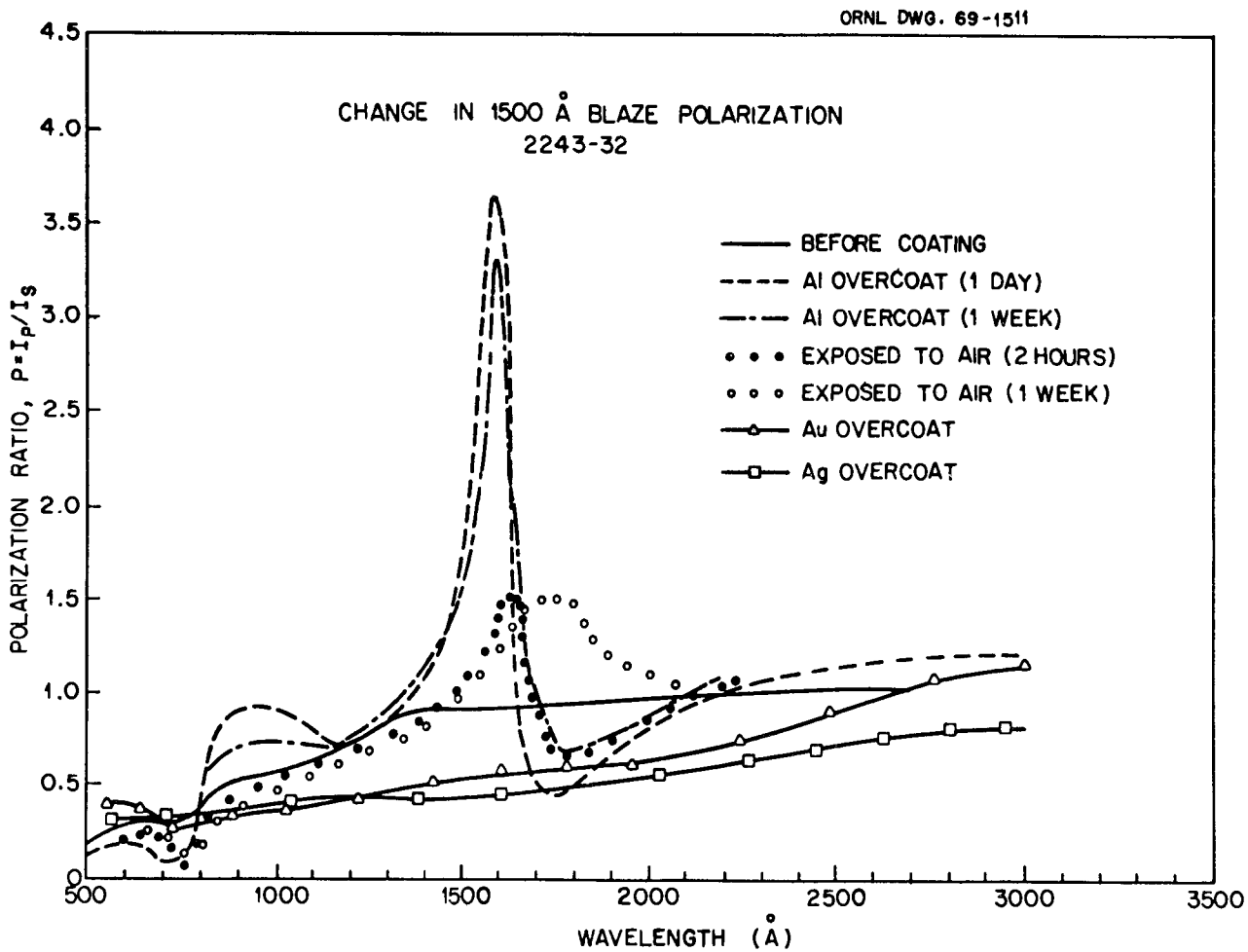

Figure 25. Change in polarization ratio, R_p/R_s , with time for vacuum evaporated Ag, Au, and Al coatings on concave grating.

its intensity decreases and shifts to longer wavelengths (1750 A° at maximum). The peak was shifted back to 1580 A° by recoating with a fresh layer of Al (90 A°) and the shift to longer wavelengths observed by re-exposing to air. This peak has been identified as the surface plasma wavelength in Al modified by the presence of an Al_2O_3 coating. The 1580 A° peak occurs at a longer wavelength than the surface plasma peak in Al (1170 A°), but this is believed due to the small oxide layer that forms at 10^{-6} Torr.

Using the dispersion relation, Equation (53) and (54), extended into the vacuum ultraviolet energy region, we obtain the set of curves (Fig. 26) for different thicknesses of Al_2O_3 on the aluminum substrate. One sees that for large $|\vec{\kappa}|$ these curves approach the same asymptotic value, 7.0 ev, corresponding to a wavelength of 1770 A°, but for smaller $|\vec{\kappa}|$ the maxima of these curves have different values. Since our analysis of the observed peaks is based on the idea that momentum transfer occurs at the grating surface, we would expect peaks to occur at those energies that have the greatest "density of states." That is, for $|\vec{\kappa}|$ far removed from the light line, even though the contribution to the intensity from each state may be small, the total transition probability is large if many states having the same or similar energy are involved. From Figure 26 we see that the greatest density of states occurs in a region slightly below where these curves have their maxima, so the observed peaks should occur at the corresponding energies. Note that an energy-angle plot, as in Figures 14, page 114, 16, page 117, or 23,

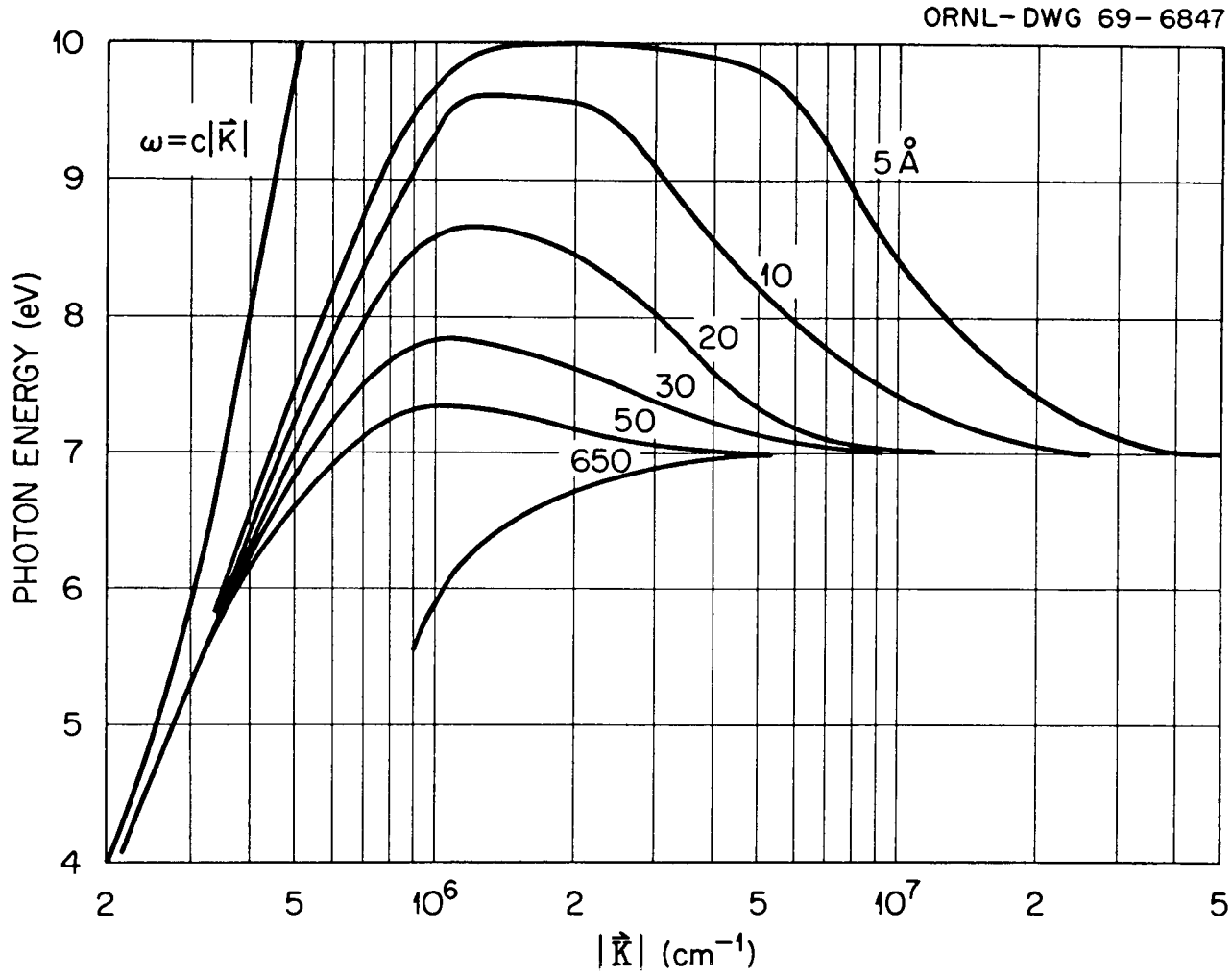

Figure 26. Theoretical surface plasmon dispersion curves for various thicknesses of Al_2O_3 on an Al substrate. Uses $\eta(\omega) = \eta_1$ for Al_2O_3 and $\varepsilon(\omega) = \varepsilon_1$ for Al.

page 137, is not appropriate, since for large energies (and large n), as we have here, the branches become so close together that they are indistinguishable. We are using ε_1 for Al from the data of Hass and Waylonis (1950) and of Hunter (1964). The values of η_1 used in the dispersion relation were calculated from the optical constants n and k for anodized films of Al_2O_3 measured in this laboratory for wavelengths shorter than 3000 A°. Here $\eta_1 = n^2 - k^2$ and $\eta_2 = 2nk$. The imaginary part, η_2, is not small in this region and, in fact, its inclusion in Equations (53) and (54) shifts the maxima of the dispersion curves to lower energies. The dispersion curves using $\eta(\omega)$ for several thicknesses are shown in Figure 27. It is seen that the curve [using $\eta(\omega)$] having its maximum density of states at 7.85 ev (the 1580 A° peak observed at 10^{-6} Torr) is for an oxide thickness of about 20 A°, and the peak of 1700 A° resulting from exposure to air for 24 hours corresponds to an oxide thickness of 45 to 50 A°. While these values seem somewhat high for a perfectly smooth surface, they may be reasonable for the surface used here. If we use η_1 only (Figure 26), the calculated thicknesses are larger, being about 30 A° and 50 to 55 A°, respectively. Note that both sets of dispersion curves (using either η or η_1) approach the same asymptotic value of 7.0 ev.

When we use a complex dielectric constant, η, in the dispersion equation we are assuming that the imaginary parts of the other parameters, such as ε, κ, and ω, are small and are therefore neglected. What we are trying to find here is the effect of the imaginary part, η_2, of the dielectric constant on the real part of the dispersion relation. In

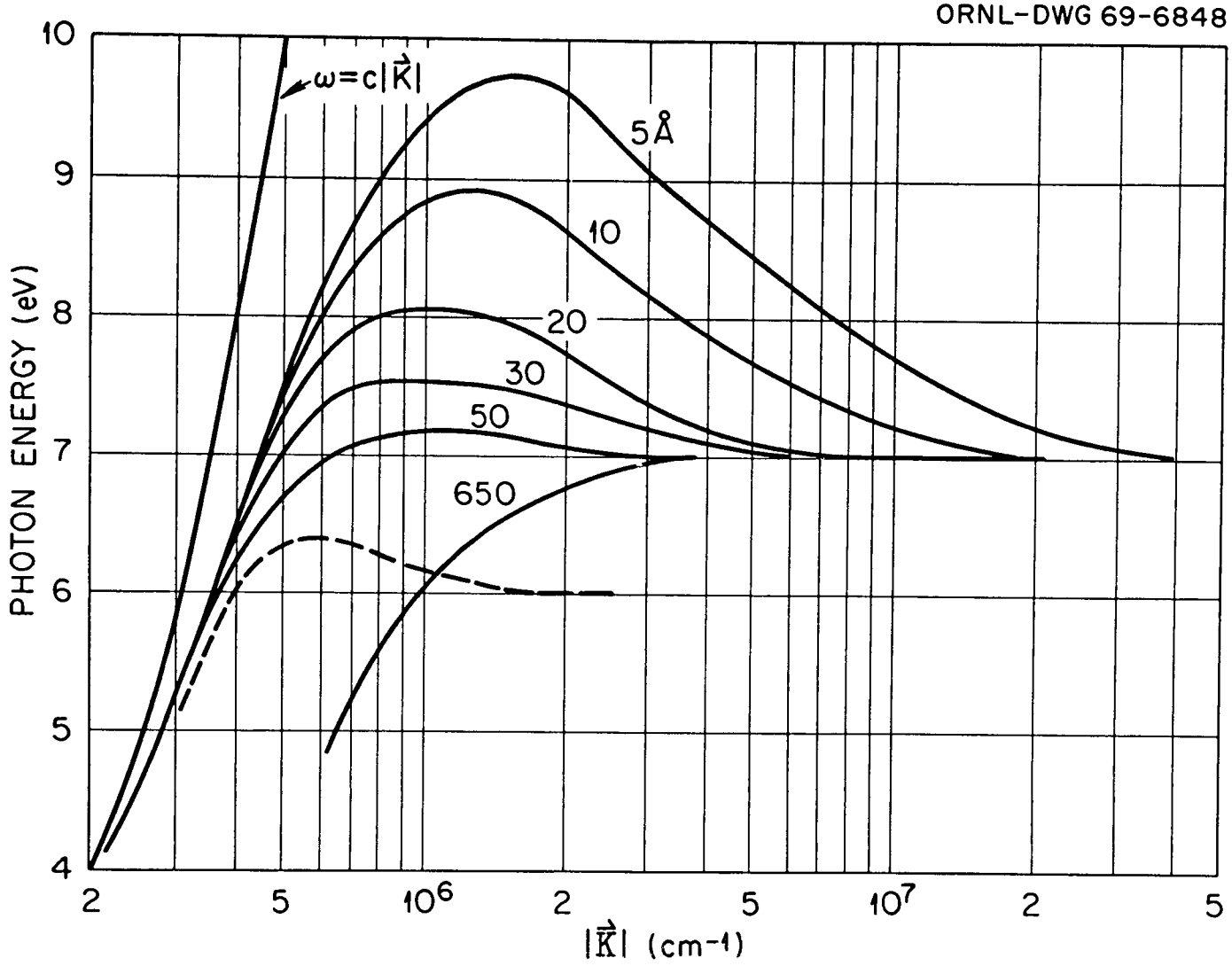

Figure 27. Theoretical surface plasmon dispersion curves for various thicknesses of Al_2O_3 on an Al substrate. Uses $\eta = \eta_1 + \eta_2$ for Al_2O_3 and $\varepsilon = \varepsilon_1$ for Al. Dotted line-20 A° Al_2O_3 and 20 A° pump oil on Al substrate.

the computer program for this situation the imaginary parts were retained through the final solution, and the thickness printed out with a real and an imaginary part (see Appendix A). We used only the real part in plotting the dispersion curves.

The peak around 850 A° is identified as the volume plasma peak in Al (λ_p = 830 A°). The wavelength of this peak does not shift in time although its intensity decreases. Since this behavior is related to the radiative mode in aluminum, a more detailed discussion shall be given later in this chapter.

Coating this surface with either Ag or Au causes both the volume and surface peaks to disappear. This is to be expected, since the plasma wavelengths of Ag and Au do not lie in the vacuum ultraviolet (3300 A° for Ag and 5200 A° for Au).

Similar time studies have been made on a fourth 600 line/mm, 1500 A° blaze grating (B and L No. 2406-22-1-9) having a new, aluminized surface [Painter, Birkhoff, and Arakawa (1968)]. The results of the polarization measurements made while the grating was in the vacuum system for 27 days are given in Figure 28. This grating had been exposed to air for about three months before being installed in the monochromator, and had already developed an Al_2O_3 coating of about 20 A°, if we assume a high-quality surface. Thus the shift to longer wavelengths of the peak at 1400 A° was attributed to diffusion pump oil condensing onto the surface rather than to an additional oxide layer. The 1400 A° peak is believed to be the surface plasma peak in Al shifted by the assumed 20 A°

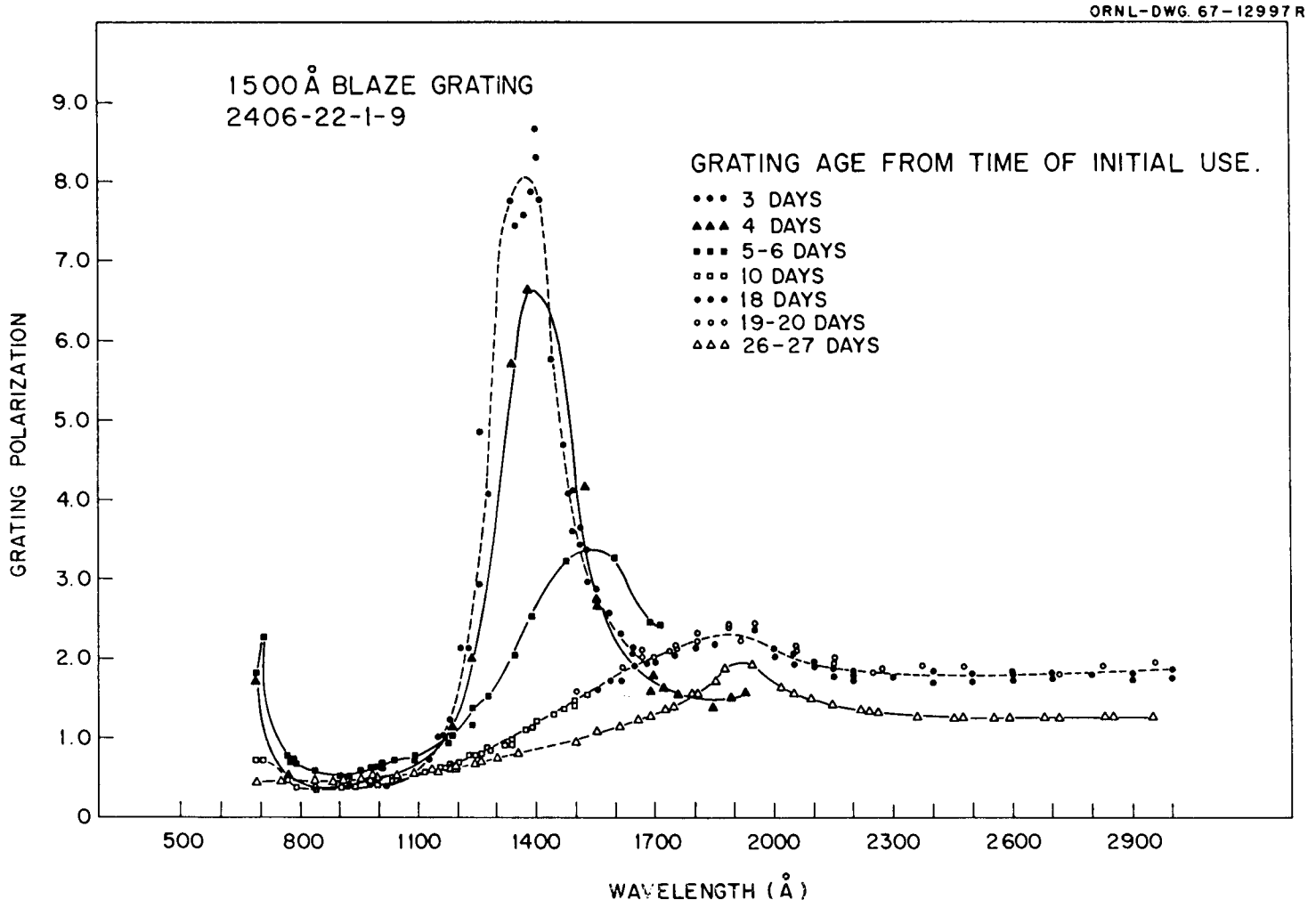

Figure 28. Change in polarization ratio, R_p/R_s , with time for a new diffraction grating.

oxide layer. The applicable dispersion curves (Figures 26, page 141, and 27, page 143) show that for the photon energy at 1400 A° (8.85 ev), the corresponding oxide thicknesses are about 12 A° [using $\eta(\omega)$] and 18 A° (using η_1). The rather good fit for 18 A° and the poorer fit for 12 A° indicates that perhaps the measured value of η_2 is slightly larger than it should be or perhaps that the actual oxide layer is thinner than 20 A°, although this possibility is believed small.

The extension into the vacuum ultraviolet region of Equations (63)-(66), which apply to the double dielectric layer on a metal substrate, is shown in Figure 27 assuming a 20 A° pump oil layer on top of the 20 A° oxide layer and using η_1 for the oxide and $\nu(\omega)$ for the oil. The dispersion curve gives a maximum density of states at 6.40 ev, which is 0.6 ev less than that for an infinite oxide layer. The wavelength corresponding to 6.40 ev is 1938 A°, and is in excellent agreement with the 1930 A° peak observed after a 27 day exposure in the vacuum system. We are justified in using η_1 instead of $\eta(\omega)$ for the oxide here because η_2 is very small around 6.50 ev.

The large width of the peak at 1938 A° is probably due to the large value of ν_2, the imaginary part of the dielectric constant of pump oil. In fact, from 1800 A° to 2000 A°, ν_2 is larger than ν_1, which means that because of the resulting short lifetime the surface plasmon is almost out of the range of being regarded a collective oscillation. In Equation (45) the half-width is given approximately by

$$\frac{\Delta\omega}{\omega} = \frac{\Delta(\hbar\omega)}{\hbar\omega} = \frac{\nu_2}{\nu_1^2 + \nu_1^2} .$$

At 1950 A°, we have $\nu_2 = 2.95$ and $\nu_1 = 0.93$, so that $\Delta\omega/\omega = .309$. Thus at 6.40 ev the half-width is 1.98 ev. From Figure 28, page 145, the peak at half-maximum extends from about 1600 A° (7.74 ev) to 2300 A° (5.62 ev), giving a half-width of 1.92 ev.

The peak at 700 A° is believed due to the radiative mode and will be discussed later in this chapter.

Grating 2406-22-1-5 with its 650 A° anodized Al_2O_3 coating was investigated in the vacuum ultraviolet and the results of the polarization measurement are shown in Figure 29. The observed peak at 1750 A° is in good agreement with the theoretical value of 1770 A° (7.0 ev) obtained from the dispersion curve (Figures 26 and 27, pages 141 and 143), using either η_1 or $\eta(\omega)$ for this thickness of dielectric. The volume peak is not observed here because of the absorption of light due to the extinction coefficient, k, becoming large at wavelengths shorter than 1700 A°.

II. INTENSITY CONSIDERATIONS

The previous analyses have been concerned with the positions of the anomalous peaks in the 1st order diffraction spectrum and their relation to the theoretical dispersion curves. No comparable consideration has been given to the intensities of these non-radiative surface plasmons because the transition probability, Equation (89), is not precisely known at this time. We present in this section some of the experimental results on the intensity measurements made with the

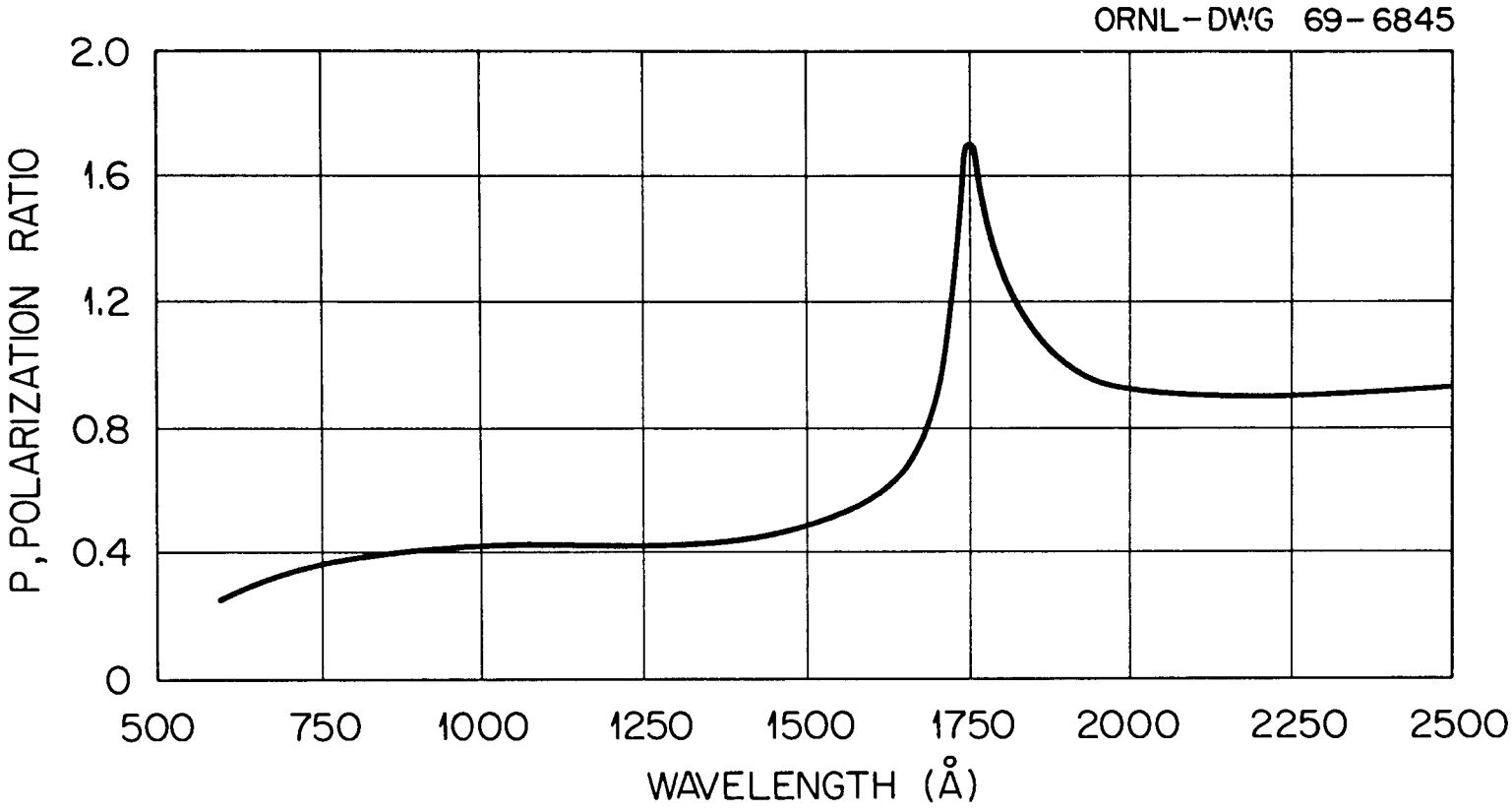

Figure 29. Polarization ratio, R_p/R_s , for Al grating coated with 650 A° Al_2O_3.

zero order, the 1st order on- and off-blaze spectra and of metal overcoating layers of various thicknesses.

The Zero Order (Reflected) Beam

For some time it has been believed and considered well understood that the energy for the anomalous peaks comes from the reflected (zero-order) beam, i.e., a peak in the diffracted beam corresponds to a dip in the reflected beam at the same wavelength [Wood (1935), Hägglund and Sellberg (1966)]. This was verified in an experiment where the concave grating 2243-32 (Al coated) was placed in the reflectance chamber and illuminated by light from the monochromator. The results of measurements made of the reflected and first order (on-blaze) spectra, given in Figure 30, show a peak in the first-order diffraction and a dip in the reflected beam occurring at the same wavelength. Although the dip appears to be small, it is in a spectrum that is 100 times as intense as the diffracted spectrum.

The First Order Off Blaze Spectrum

Apparently energy is removed from the first-order diffracted beam on the off-blaze side as well, as can be seen from Figure 31, where typical spectra for the first-order on- and off-blaze diffracted beams are shown for the same value of θ where the overcoating metal is Ag. The anomalous wavelengths (off-blaze) appear as dips at the same wavelengths as the peaks on the on-blaze side. Note the dip at the plasma wavelength for both cases indicating volume plasma absorption regardless

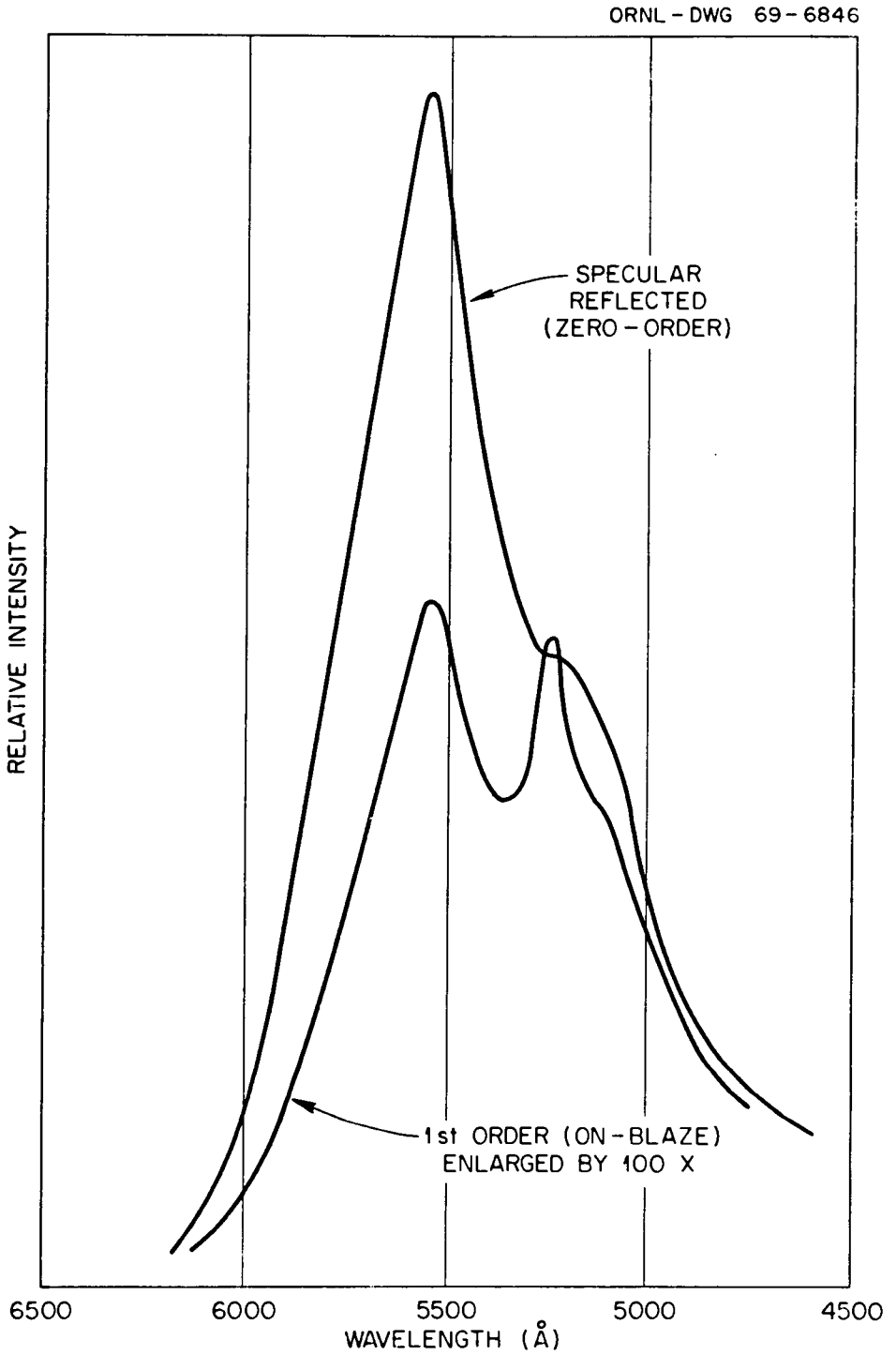

Figure 30. Anomalous polarization phenomena in (a) specular reflected (zero-order) and (b) diffracted 1st order on-blaze spectra. Reflected spectrum is 100 times more intense than diffracted spectrum.

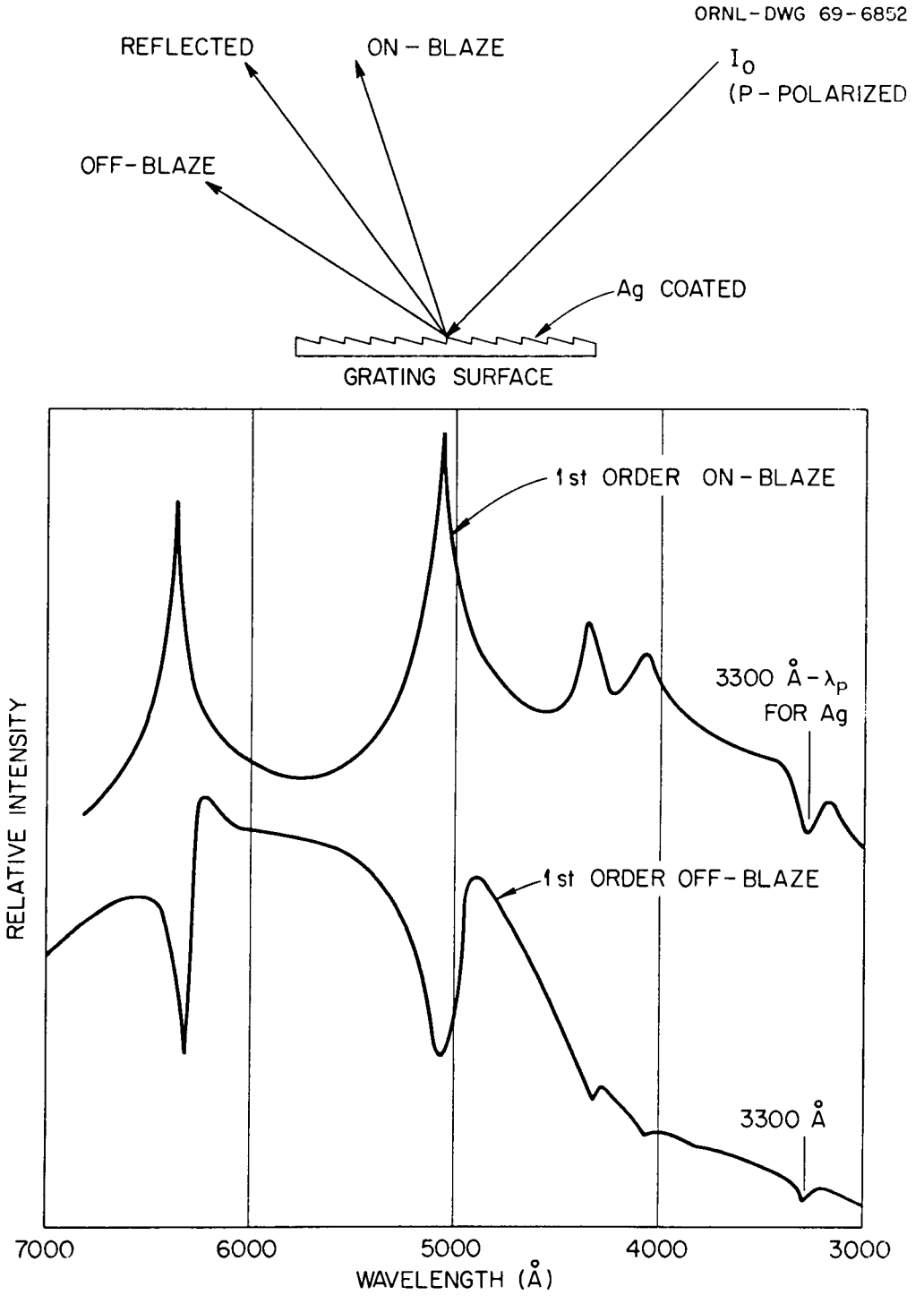

Figure 31. First-order diffracted on- and off-blaze spectra for Ag-coated grating.

of the diffraction order. This absorption in Ag is in contrast to the behavior in Al where an emission peak was observed at the volume plasma frequency. The reason for the difference is not entirely clear at this time, but may be related to the radiative mode behavior discussed later in this chapter.

Metal Layers

The effect on the intensity of overcoating different thicknesses of Ag onto an aluminum substrate at a fixed value of θ is given in Figure 32. The intensities of the peaks in the $|p-s|$ difference spectrum increase but their positions stay the same as the layer thickness is increased. It was pointed out earlier in this chapter that for metal thicknesses above about 400 A° on a metal substrate the dispersion curve is essentially that for an infinite layer, so we expect no shift in the wavelength of these peaks. The changes in intensity indicate less plasma wave damping as the thickness is increased and is probably due to an overall smoother aggregate being formed on the surface with the larger thicknesses. This increase of intensity with thickness was noted also with Al and Au evaporated layers.

The First Order On-Blaze Spectrum

The relative intensities of the anomalous peaks in the p-polarized spectra were obtained for the aluminum coated grating 2243-32 and are given in Figure 33 for positive n values and in Figure 34 for negative n values. The relative intensity is defined here as the ratio of the

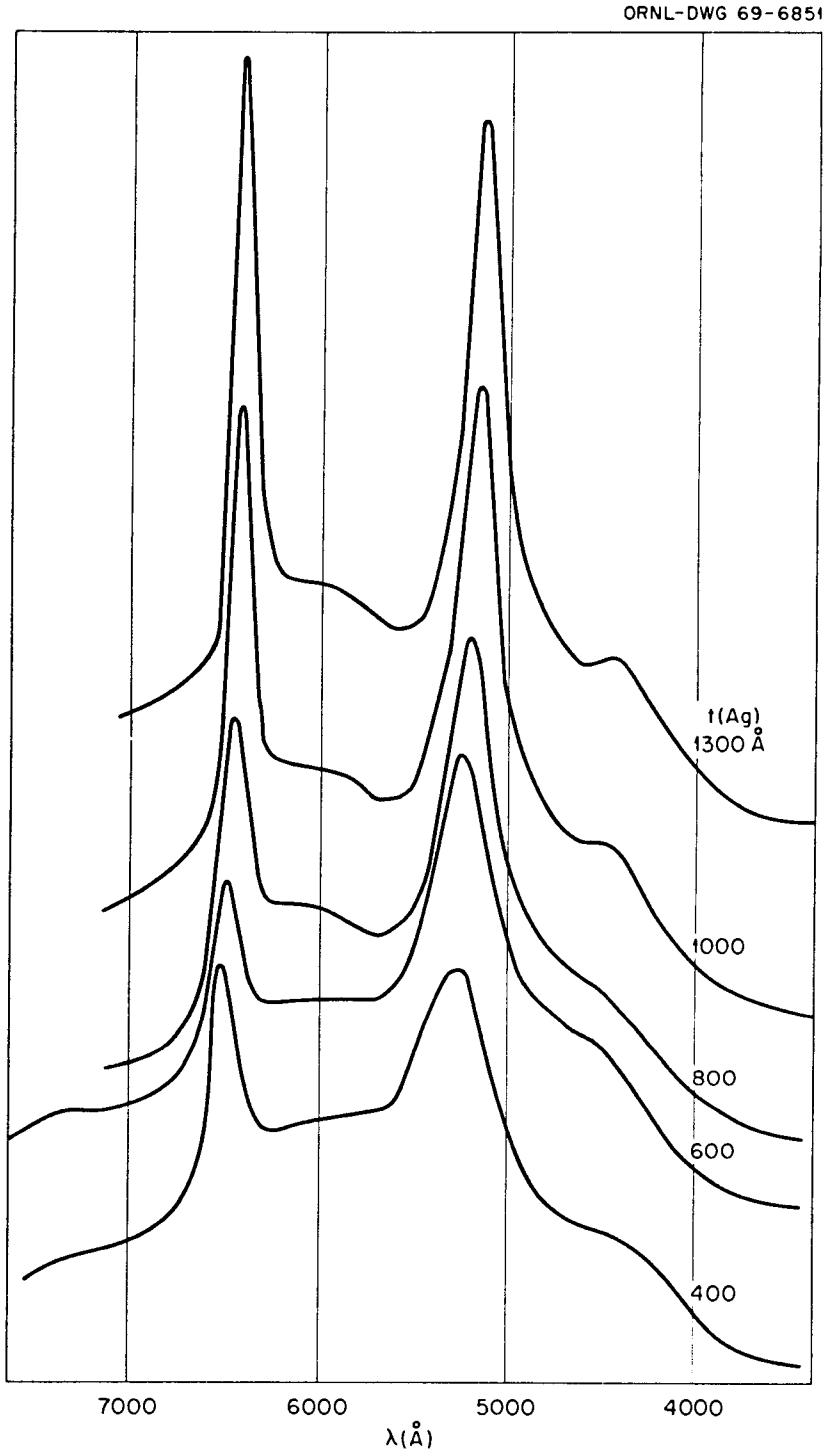

Figure 32. Relative intensity in spectra of grating coated with various thicknesses of Ag.

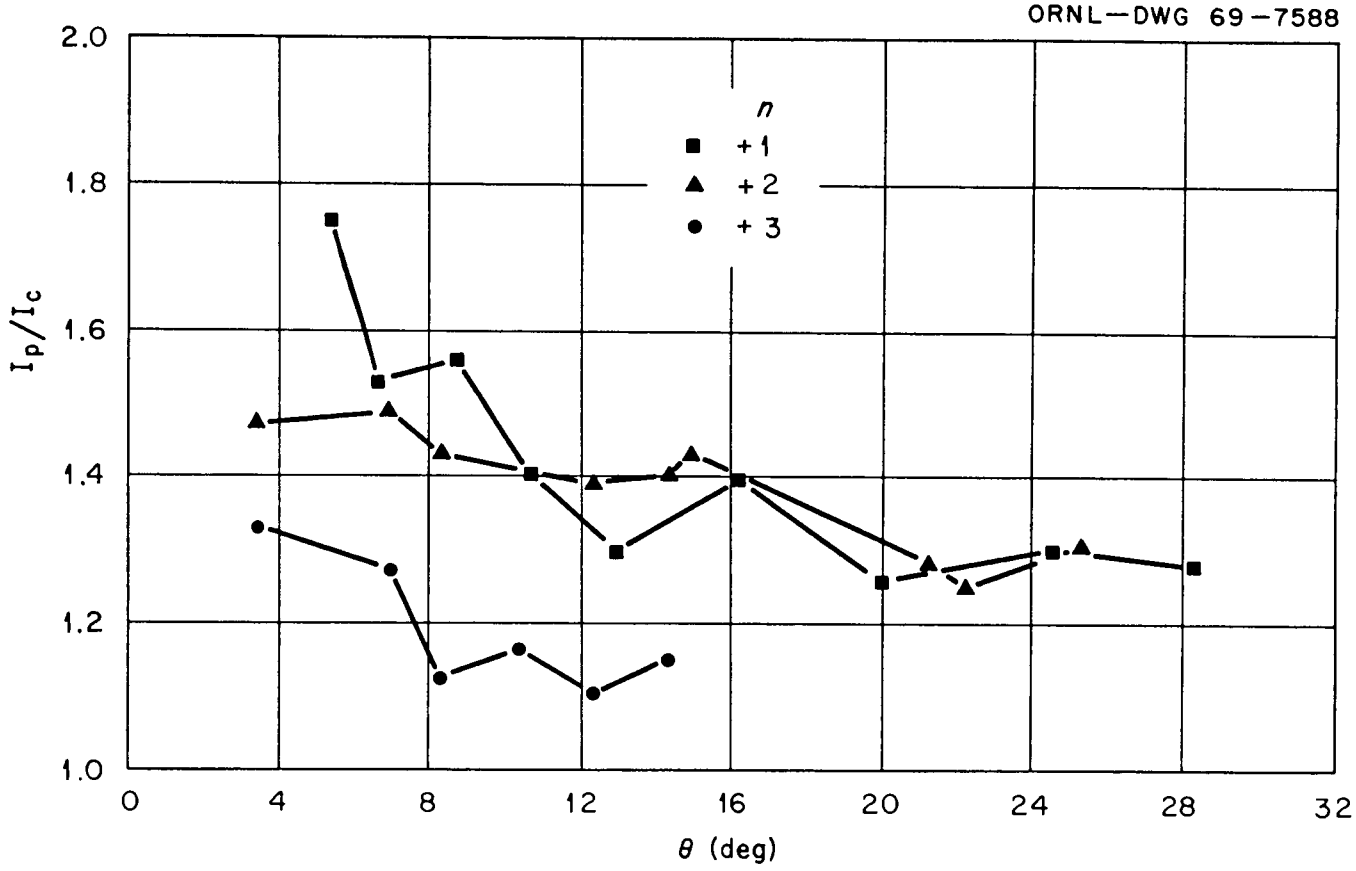

Figure 33. Relative intensities of anomalous peaks for positive branches, +n, as a function of angle, θ .

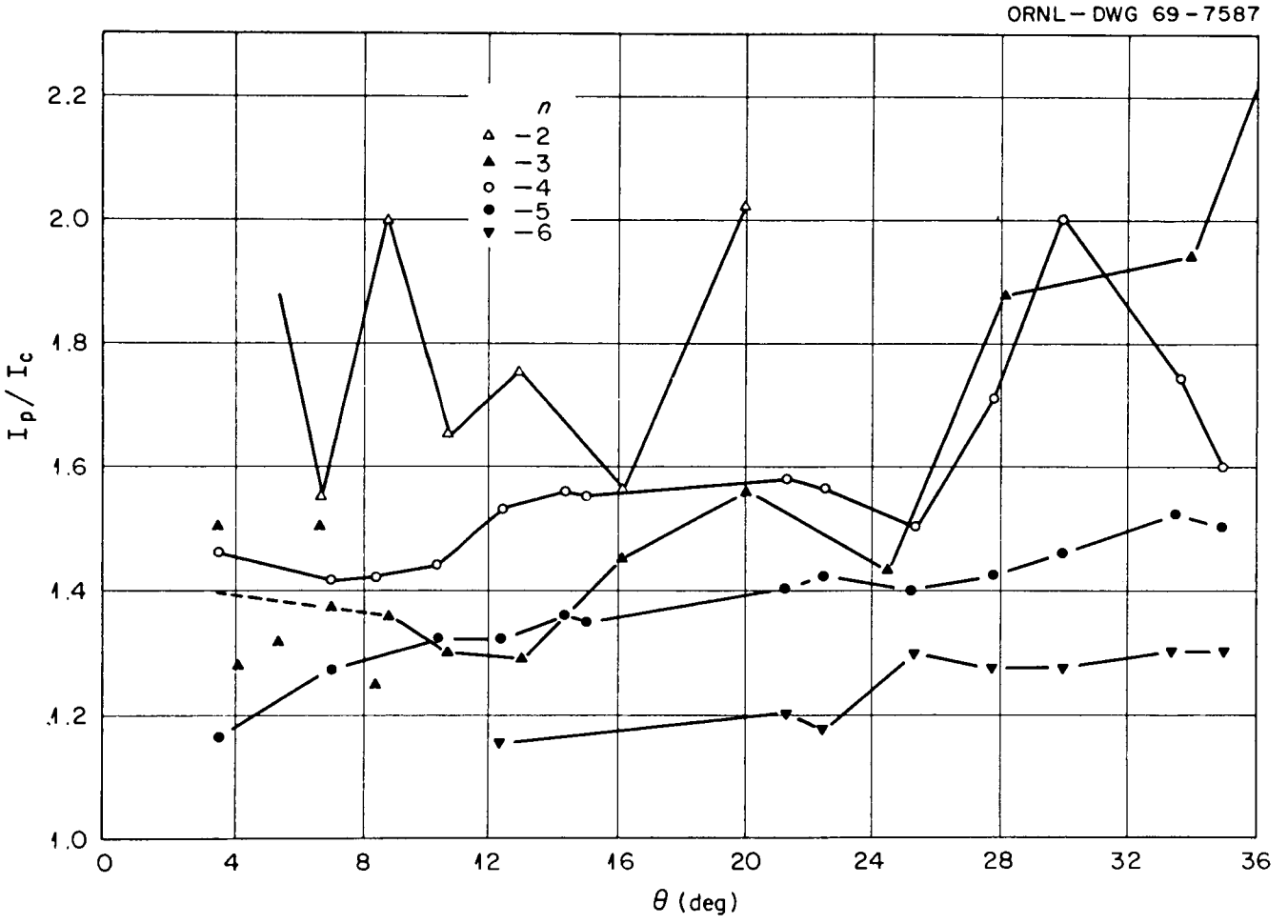

Figure 34. Relative intensities of anomalous peaks for negative branches, -n, as a function of angle, θ .

intensity at the peak to the intensity at the continuum in the absence of the peak, where both intensities are measured above the background level. The results show that the intensity increases as the n values decrease, which is what could be expected, since a large momentum transfer, corresponding to a large n, might be less probable that a small momentum transfer, involving a small n. A large n may also be associated with greater damping of the surface plasma wave. One also finds in general that as θ increases the intensity decreases for positive n and decreases for negative n, but the reason is not clear at this time. It is hoped that a detailed perturbation calculation of the intensities which is new in the process of being completed, will elucidate some of these experimental results.

III. GRATING FOILS AND THE RADIATIVE MODE

Foils on Concave Gratings - Non Radiative Mode

The first grating "foil" to be considered is the one formed by coating a thin metal layer over a dielectric coating on a concave grating. We refer to a foil here as any metal layer thin enough for coupling to occur between the surface plasma waves on either side of it. Grating 2406-22-1-5, with its 650 A° Al_2O_3 layer on an aluminum substrate, was coated with 150 A° of vacuum evaporated aluminum, and the spectrum in the vacuum- and near-ultraviolet and visible regions scanned for evidence of both the normal and tangential mode surface plasmons. The thickness of 150 A° was chosen because the dispersion curves,

Equations (56) and (57) for an oxide-free coating or Equations (59) and (60) including the oxide, show that the peaks for each mode should fall far enough apart on the dispersion plot to be resolvable. With a smaller thickness, on the other hand, a surface plasmon might not propagate without considerable damping and resultant broadening of the anomalous peaks.

Measurements made in the vacuum ultraviolet for the freshly evaporated surface showed that no anomalous polarization peaks were present. The same result was obtained when the surface was allowed to oxidize. The reason may be that the anodization of such a large dielectric thickness caused the grooves to become altered in such a way as to prevent coupling between the photons and the short wavelength surface plasmons.

In the longer wavelength region anomalous peaks were found, but only for the tangential mode. The experimental dispersion curve, obtained from Equation (93), is given in Figure 35. The solid lines are Equations (59) and (60), assuming an oxide layer of 40 A° on the aluminum surface, and the dashed line is the non-radiative mode for 40 A° Al_2O_3 on a semi-infinite Al substrate. One sees that there is a definite shift of the tangential mode from the semi-infinite case to values characteristic of thin foils, and this shift is in good agreement with theory.

The reason that the normal mode excitations did not appear could be due to (1) excessive broadening of these peaks because of some

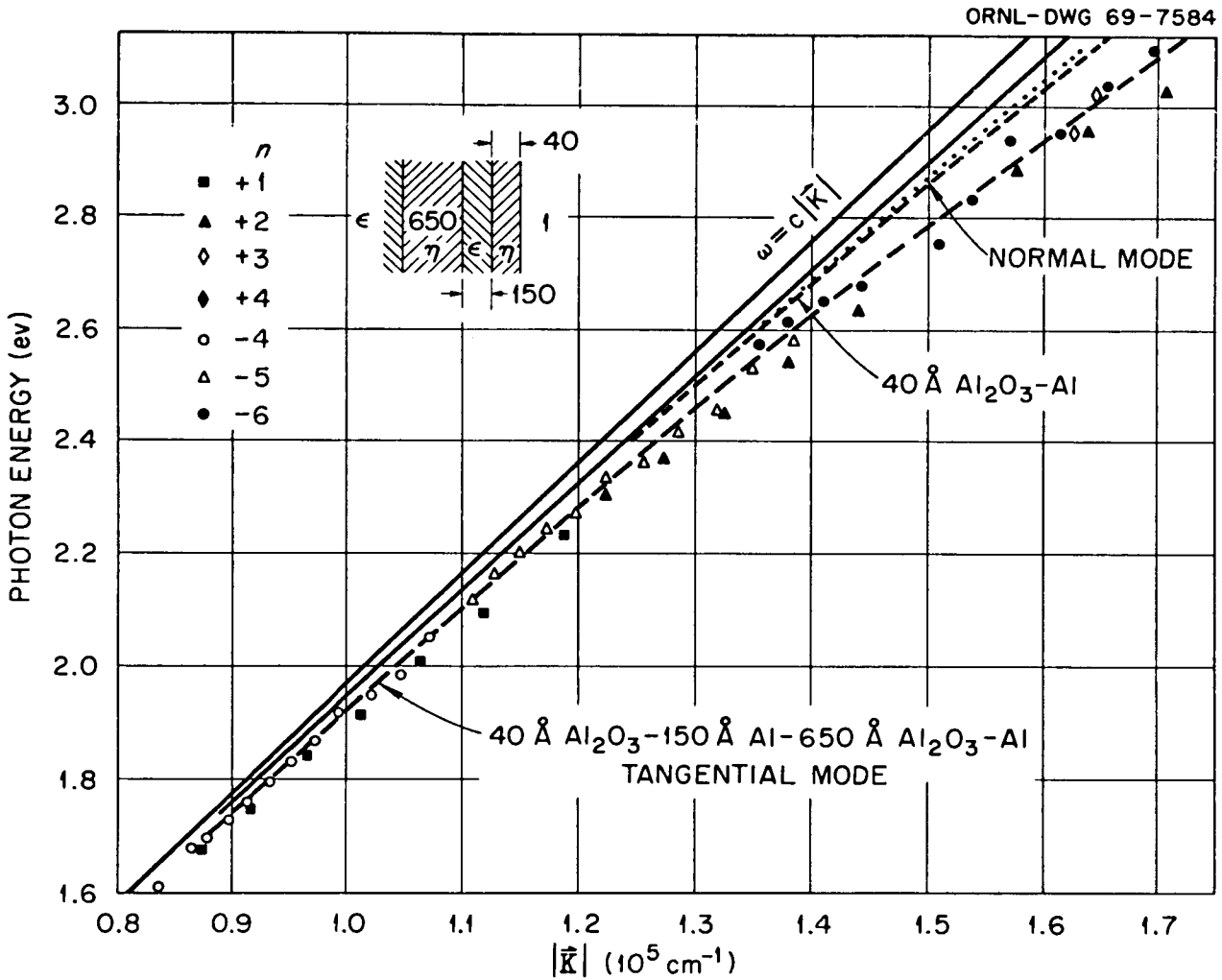

Figure 35. Non-radiative surface plasmon dispersion curves for Al substrate coated with 650 A° Al_2O_3, 150 A° Al, 40 A° Al_2O_3, and vacuum. Dotted line - normal mode; heavy dashed line - tangential mode; medium dashed line - 40 A° Al_2O_3 on Al substrate; solid line - pure Al.

unknown damping mechanism and (2) that fact that they may naturally have a low intensity for the thickness used. The best available theory, which applies to incident electron excitation, predicts equal intensities for the normal and tangential modes for an aluminum thickness of 100 A° (no oxide layer). For smaller thicknesses the tangential mode intensity is greater, but for larger thicknesses the normal mode intensity predominates, being about twice as great as the normal mode intensity at 150 A° [Schmuzer (1964)]. The experimental results, obtained at energies characteristic of the surface plasma wavelength, show good resolution of the normal and tangential peaks [Boersch, et al. (1966)] at 150 A°, but with the normal peak much weaker. Better intensity is obtained at a thickness of 270 A°, but with the peaks just barely resolvable. Other experimental results [Swan, Otto, and Fellenzer (1967)] give almost equal intensities and good resolution at a thickness of 110 A°. In both these experiments the foils were assumed to be coated with a 40 A° of oxide layer on each side.

The grating was coated once more with an additional layer of 100 A° of Al, but all this did was to shift the peaks to values on the dispersion curve characteristic of a 250 A° Al thickness, and no normal mode excitation was observed.

Some of the results obtained previously in the vacuum ultraviolet for grating 2243-32 could be re-interpreted if the Al coating is regarded as a foil. What we have is 100 A° of Al evaporated onto an Al substrate that has oxidized naturally, so there is a vacuum-metal-

dielectric-metal multilayer. The 40 to 50 A° oxide layer was disregarded in the earlier treatment. The only difficulty is that the peak at 1580 A° would have to be explained as a normal mode excitation, and there should be another peak at 1900 A° due to the tangential mode. These peaks are predicted from the appropriate dispersion curves, Equations (59) and (60), extended into the vacuum ultraviolet. Also previous results indicate that the tangential mode has a greater probability of appearing than does the normal mode.

A further attempt was made to detect the normal mode in the visible and near-ultraviolet by preparing a 300 A° Ag grating surface on a concave grating blank by the epoxy treatment mentioned earlier. The anomalies seen here were very weak and broad, corresponded to the tangential mode only, and in some spectra, were non-existent. The anomalous peaks became more pronounced if additional thicknesses of Ag were evaporated onto the surface. The weakness of these peaks may be related to the form of the dispersion equation [Equation (62)], which applies to the case of a metal foil bounded on one side by vacuum and on the other by an (effectively) infinite thickness of dielectric. For values near the light line, the F' term is oscillatory instead of exponential and difficulties are encountered when an infinite dielectric thickness is substituted into the argument of the tangent. Physically this means that the surface wave at the metal-dielectric interface can be spread out through the whole dielectric layer, and this could lead to excessive damping of the wave. As the foil thickness is increased,

coupling to the metal-dielectric surface is decreased and we approach the condition of a pure metal substrate.

Concave Gratings-Radiative Mode

The peaks observed in the vacuum ultraviolet at 850 A° and 700 A° for gratings 2243-32 and 2406-22-1-9, respectively, have been tentatively attributed to radiative mode excitation.

The first of these peaks, at 850 A°, is for the same "foil" surface considered in the previous section, where a 100 A° Al layer on an oxide layer of 40 A° is on a semi-infinite Al substrate. An approximation to the intensity of this peak may be obtained from Equation (88), which strictly applies to a metal foil bounded on both sides by vacuum. At the plasma frequency this reduces to

$$\frac{P_{pn}}{P_{sn}} = \frac{\sin^2\alpha \sin^2\beta \, \omega_p^{\,2} \, [\omega_p^{\,2} + 49 \, (\gamma + \gamma')^2/16]}{\gamma^2 \, \gamma'^2}$$

where $\psi = 0°$ with the grooves perpendicular to the plane of incidence. The electronic damping, $\hbar \gamma_d$, is given by $\hbar \gamma_d =$

$\hbar \omega_p \varepsilon_2 = 5.52$ ev where $\varepsilon_2 = 0.264$ and the angles of incidence and diffraction, α and β, are 33.3 and 36.7°, respectively, at a diffracted wavelength of 850 A°. Thus using the thickness of 115 A° and the expressions for γ and γ' (Equation (81), we obtain

$$P_{pn}/P_{sn} \approx 6.3.$$

One might ask whether the thin foil interpretation is correct, since it did not seem to be applicable to the non-radiative mode considered in the previous section. We believe, however, that the radiative mode excitation, which requires only a small momentum transfer due to the small κ vector, is more probable than the non-radiative excitation, which required a larger momentum transfer. The measured peak (Figure 25, page 140) includes effects from the normal diffracted light as well as the anomalous polarization. In the absence of the peak this ratio is about 0.4, and with it, about 0.9. The p to s ratio for the peak is thus increased by a factor of 0.9/0.4 = 2.25 over the continuum value. The calculated half-width is of the same order of magnitude as the measured value of about 4 ev (800 to 1100 A°). For the second Al evaporated layer of 90 A°, which gives a total thickness of 205 A° (neglecting the oxide layer between the two), the calculated polarization ratio becomes $P_{pn}/P_{sn} \approx 3.3$. The measured value is increased over the continuum value by a factor of 1.1/0.4 = 2.75. This peak also had a measured half-width of the same order of magnitude as the calculated value. The above experimental results would compare favorably with theory if the continuum polarization ratio were normalized to unity.

The peak at 700 A° on grating 2406-22-1-9 could not be due to any foil effects since the surface is an Al substrate several hundred A° thick. Kliewer and Fuchs (1967), however, have shown that radiative modes can exist in slabs as thick as 12000 A° (for a plasma frequency of 15 ev), and furthermore, that the energy at which these modes appear

is a function of the angle of incidence. Figure 36 shows this dependence for the lowest order excitation for 12000 A° and 240 A° thick slabs. The 700 A° peak occurs at an incidence angle of about 35°. From Figure 36 the radiative mode at this angle for the thick slab should appear at 1.2 times the plasma frequency, or an energy of 18.2 ev, which corresponds to a wavelength of 680 A°, in good agreement with the measured peak. For a thickness of 240 A°, on the other hand, the radiative mode appears at the plasma frequency for an incidence angle of 35°. This agrees with the results found for grating 2243-32, if we can regard that surface as being equivalent to a thin foil.

These comparisons must be considered somewhat tentative, since the work of Kliewer and Fuchs applies to absorption instead of re-emission. Their theory does not explain the absorption at the plasma wavelength in Ag in the on- and off-blaze spectra, because here there was a thick layer and angles of incidence larger than 35°. One explanation might be that resonance absorption simply predominates over radiative emission. Another might be that interband effects in Ag near the plasma frequency have some influence on the absorption. These are, however, a matter of speculation at this time.

Grating Foils

Grating foils of many types were investigated, and these included thin layers of Au, Al, and Ag in thicknesses from about 100 A° to several hundred A°. These were analyzed in the reflectance chamber or with the prism monochromator by scanning the spectrum with p-polarized

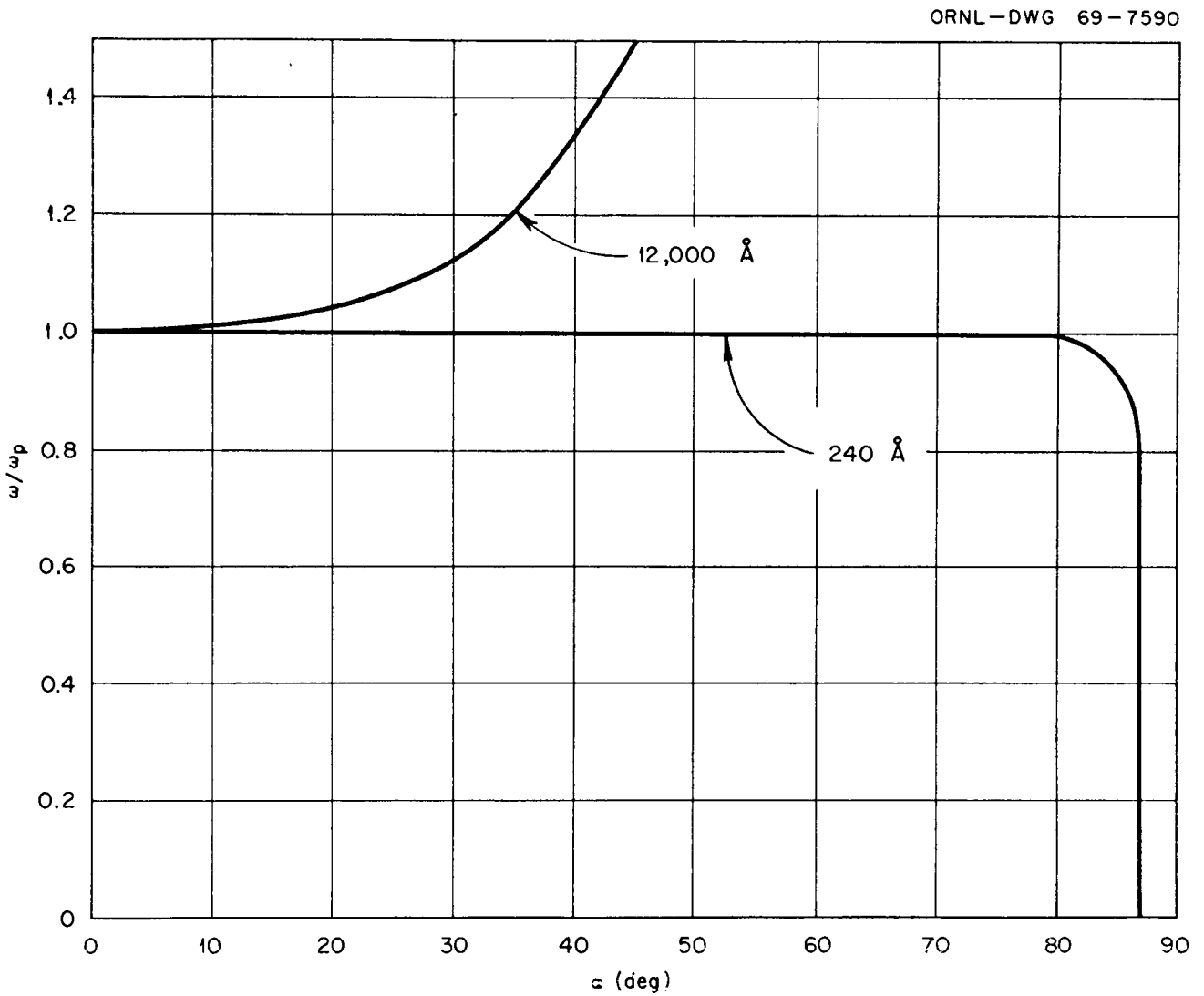

Figure 36. Radiative surface plasma modes for Al foil of thickness (a) 12000 A° (b) 240 A°, for different angles of incidence.

monochromatic light holding the angles of incidence and diffraction fixed and detecting the transmitted or diffracted light.

The only foils exhibiting plasma effects were those made of Ag having layer thicknesses on the order of 300 A°. All foils of this type, whether made with plastic replicas or reproduced from a concave grating, showed pronounced absorption at the plasma wavelength (3300 A°) in the transmitted beam at large angles of incidence ($\alpha = 60°$). This is characteristic of plasma resonance absorption and has been observed many times with ordinary Ag foils of this thickness (see Chapter I).

The theory of Wilems and Ritchie, which predicts a peak in the p-polarized spectrum at the plasma frequency should be applicable for this situation. The geometry is similar to that used in the PREL (plasma resonance emission, excited by light) experiments for ordinary foils. The only grating foil to show this behavior was the one made with the groove profile of grating 2243-32. The results of the transmitted and diffracted beam measurements are given in Figure 37. Note that the intensity of the diffracted peak decreases as the incidence angle decreases and also as the diffraction angle increases (Figure 38). This is almost in accordance with theory for flat foils, which predicts that the maximum intensity should occur at a diffraction angle of 30° [Kretschmann and Raether (1967)]. Evaluation of Equation (88), with $\alpha = 60°$, $\beta = 30°$, $\gamma_d = 1.10$ ev, and $\hbar\omega_p = 3.76$ ev, and $a = 300$ A°, yields $P_{pn}/P_{sn} \simeq 12$, which is larger than the observed peak. The ratio of the diffracted peak intensity to that of the transmitted beam is

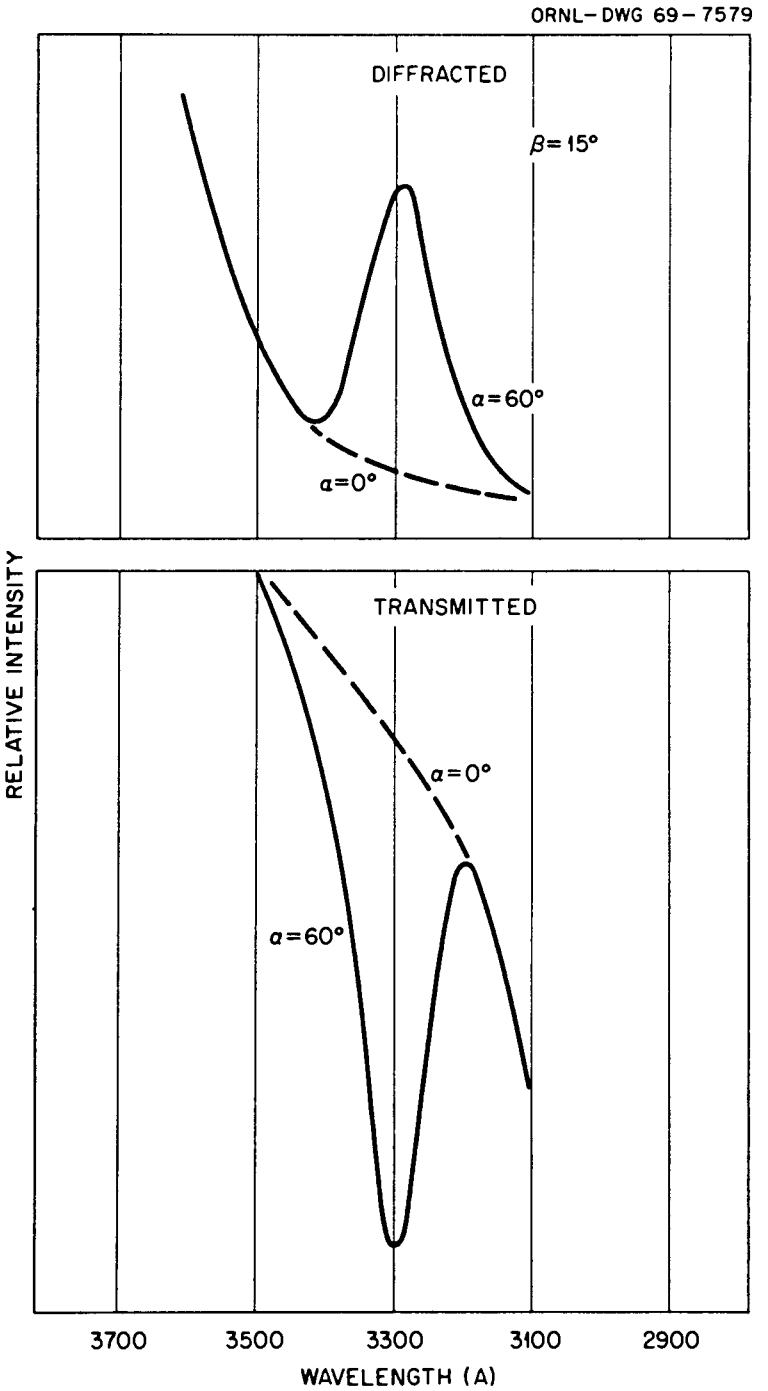

Figure 37. Plasma radiation excited by light for 300 A° Ag grating foil. Intensity of transmitted beam is 100 times that of diffracted beam.

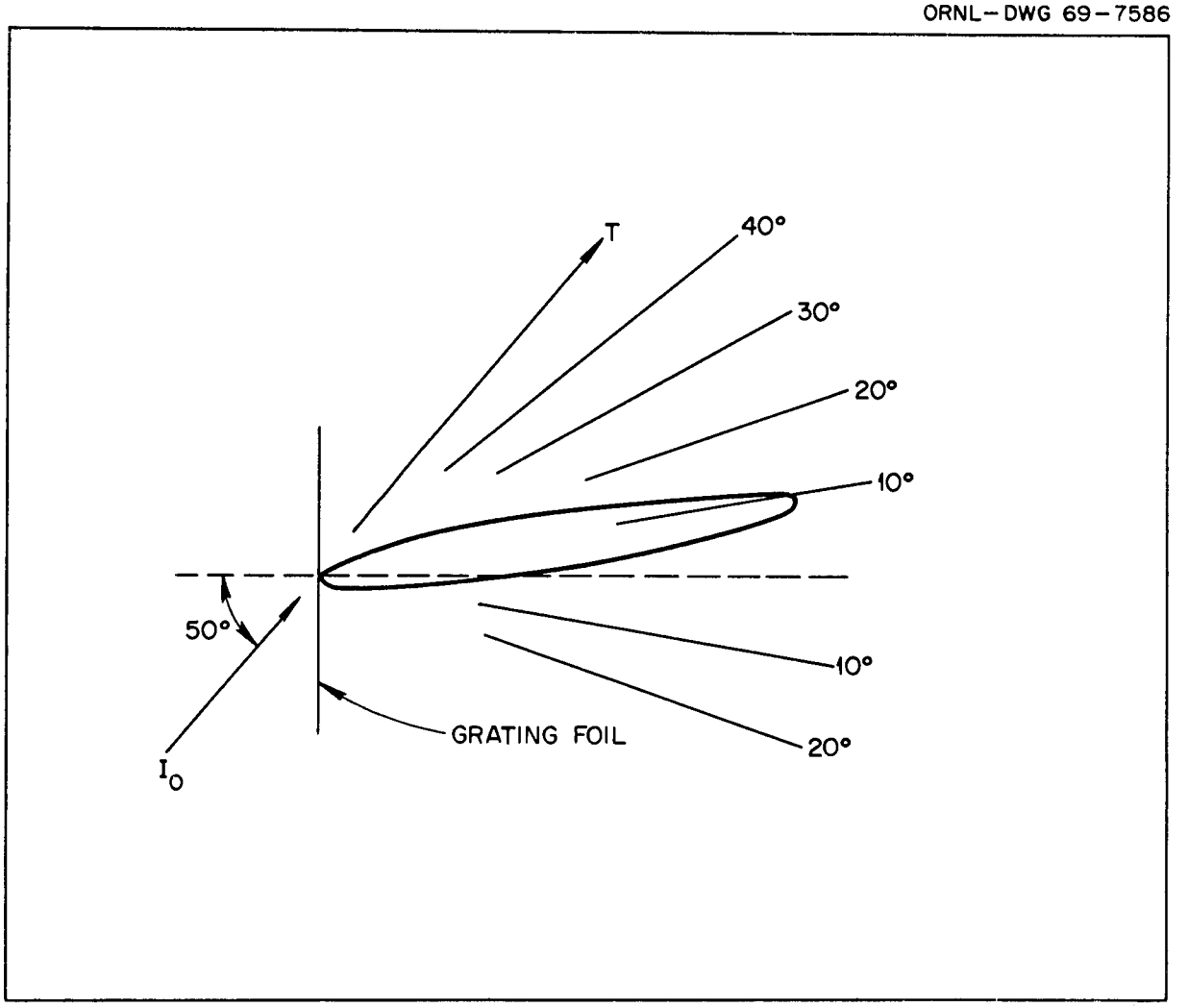

Figure 38. Relative intensity at the plasma wavelength of p-polarized peak in diffracted beam for various diffraction angles.

very good, however, being on the order of 10^{-2}. This compares with a value of about 10^{-4} obtained by Brambring and Raether (1967) in a PREL experiment.

The Grating Profile

The previous experiments have all illustrated the importance of the grating profile in allowing coupling to occur between the incident photons and the surface plasmons. It is curious that only the 600 line/mm, 1500 A° blaze grating demonstrated anomalous polarization effects. In an effort to see if there were significant structural differences in the groove shape between this grating and the others, electron micrographs were made of the surfaces of grating 2243-32 and one of the plastic replicas (Figure 39). These photographs do not, however, show any unusual differences between the two surfaces. It is hoped that later photographs using shadowing techniques will bring out the relief features of the grooves in more detail.

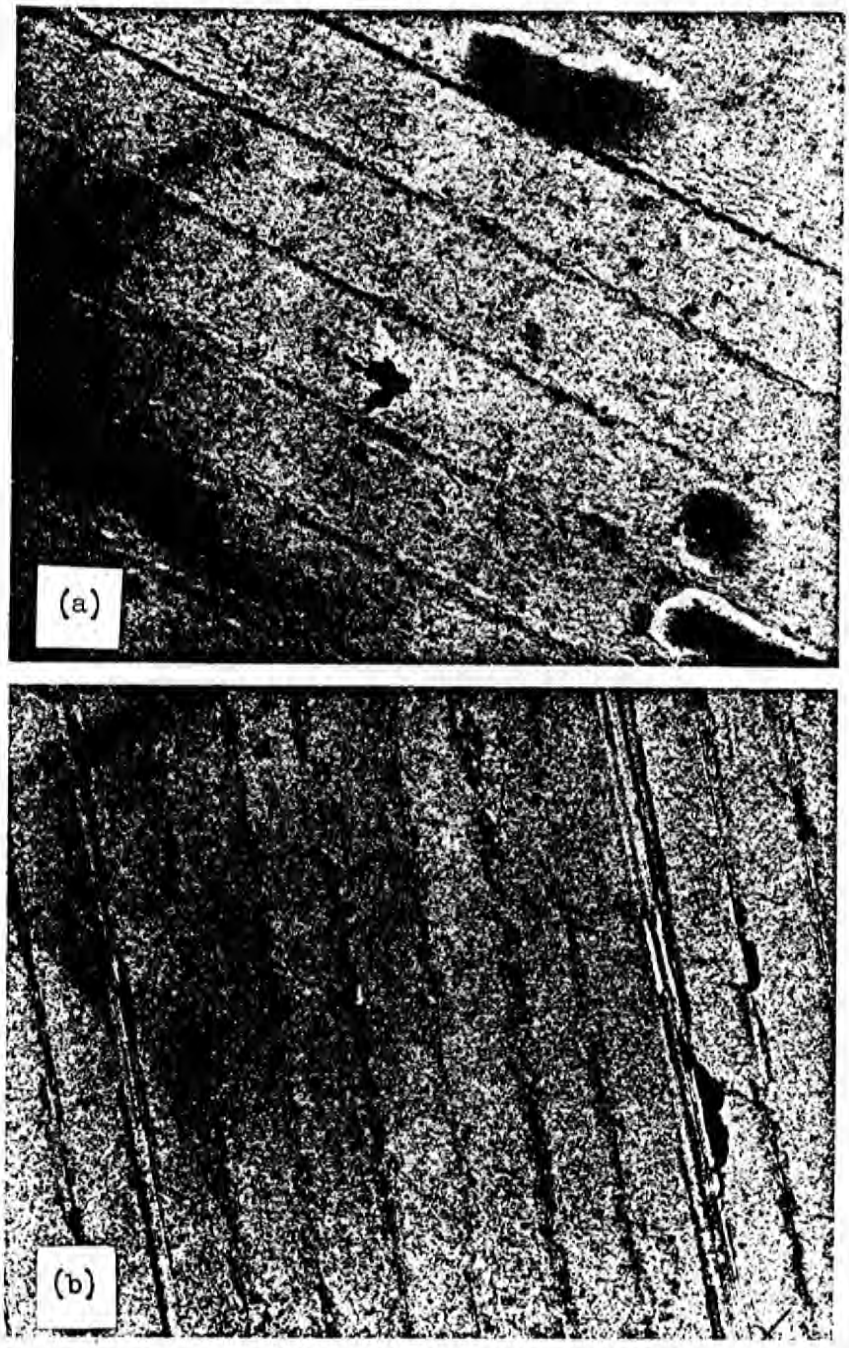

Figure 39. (a) Grating profile of 600 line/mm concave grating exhibiting anomalies (b) grating profile of 600 line/mm plastic replica grating exhibiting no anomalies.

CHAPTER VI

SUMMARY

This study has revealed many interesting results concerning Wood's anomalies and the properties of surface plasma waves in metals. In the first place it is believed that Wood's anomalies can be well explained in terms of the dispersion of surface plasmons, whether on the pure metal surface or on one coated with different dielectrics. This has been demonstrated in the visible and near ultraviolet by the excellent agreement between the experimental dispersion curves obtained directly from the anomalous wavelengths and those curves obtained theoretically assuming surface plasmon propagation on the surface. In particular, we have investigated those cases dealing with (1) semi-infinite Al, Au, and Ag substrates (2) semi-infinite Al substrates coated with varying thicknesses of the dielectrics MgF_2, Al_2O_3, and diffusion pump oil (3) thin Al layers separated from an Al substrate by a thick Al_2O_3 dielectric layer. In the first two of these it was the non-radiative surface wave that was excited. A (retarded) dispersion relation was developed for the case of dielectric-coated metal layers that was extended into a low energy region not previously investigated. Shifts to longer wavelengths were found for the dielectric coated surfaces that were characteristic of the depolarizing effect of these layers. In the third case the wavelength shift was characteristic of the non-radiative tangential mode on thin metal layers.

Studies were made to detect Wood's anomalies in the vacuum ultraviolet, a region that had not been investigated earlier for their presence. Peaks were found in this region that corresponded very well with the appropriate non-radiative surface plasmon dispersion curves. Here Al substrates with various thicknesses of Al_2O_3 and diffusion pump oil were investigated. It was found that only a small dielectric layer (~50 A°) will shift the anomalous peaks several hundred A° in this region, but for greater thicknesses any further shift is small. In the visible and near-ultraviolet regions, on the other hand, the wavelength shift is small for small layers (~50 A°), but can be quite large (several hundred A°) for a dielectric layer several hundred A° thick.

Radiative modes on concave gratings and thin grating foils were also investigated. With the concave gratings an Al substrate and an Al-Al_2O_3 thin layer on an Al substrate were investigated. The results were in reasonably good agreement with the theory for radiative surface plasmons, but the evidence is not as conclusive as for the non-radiative modes.

We believe that the results show good evidence for the existence of the surface plasmon as an elementary excitation and for the use of time-dependent quantum mechanical perturbation theory to describe the interactions involved. A further quantum-mechanical effect, the self-energy of the surface plasmon, was used to predict quite accurately the band-gap effect that was particularly evident for the MgF_2 coated Al grating and the Au coated grating. No further definitive remarks can

be made about these gaps except that they appear to become more predominant the further their dispersion curve is from the light line, $\omega = c|\vec{k}|$, i.e., for surface plasmons that are propagating much slower than the speed of light.

Experiments conducted on the intensities of the anomalies revealed the following: (1) surface plasmons propagate with less damping as the metal layer thickness is increased (2) the energy for the anomalous peaks in the on-blaze spectra comes from the central (reflected) image and perhaps even from the off-blaze spectra (3) anomalies appearing at higher energies are damped to a greater degree than those at lower energies.

It was also verified that anomalies do not appear at wavelengths less than the plasma wavelength, λ_p , of the metal that coats the grating. For example, anomalies that were found in the vacuum ultraviolet for Al did not exist for Ag and Au.

We believe that the presence of the anomalies is greatly influenced by the groove shape of the grating profile. The fact that the anomalies appeared for only one type of grating with a particular blaze angle is evidence of this. The groove shape obviously affects the strength of the coupling between the incident light and the surface plasmons, but electron micrographs did not reveal this difference.

It is suggested that further studies could be conducted with (1) comprehensive experimental and theoretical investigations of the intensities in all the diffracted orders (2) different overcoating

layers, such as certain metals whose plasma wavelengths lie in the vacuum ultraviolet, or with certain semi-conductors, to see if plasma waves can be made to propagate, and (3) experiments with different grating line spacing and blaze angles to find some correlation between groove shape and the anomalous polarization peaks.

BIBLIOGRAPHY

BIBLIOGRAPHY

Aisenberg, S., Bull. Am. Phys. Soc., 12, 984 (1967).

Anderson, W. A., G. L. Griffin, C. F. Mooney, R. S. Wiley, Applied Optics, 4, 999 (1965).

Arakawa, E. T., R. J. Herickhoff, R. D. Birkhoff, Phys. Rev. Letters, 12, 319 (1964).

Arakawa, E. T., N. O. Davis, R. D. Birkhoff, Phys. Rev., 135, A224 (1964).

Bausch and Lomb, booklet 35-261, 0866 (1967).

Berning, P. H., G. Hass, and R. P. Madden, J. Opt. Soc. Am., 50, 586 (1960).

Bloch, F., Z. Physik, 81, 363 (1933).

Bloch, F., Helv. Phys. Acta, 7, 385 (1934).

Boersch, H., J. Geiger, A. Imbusch, and N. Niedrig., Phys. Letters, 22, 146 (1966).

Born, M., and E. Wolf, Principles of Optics, (Pergammon Press, New York, 1959), pp. 608-612.

Bösenberg, J., and H. Raether, Phys. Rev. Letters, 18, 397 (1967).

Brambring, J., and H. Raether, Phys. Rev. Letters, 15, 882 (1965).

Brambring, J., and H. Raether, Z. Physik, 199, 118 (1967).

Brambring, J., Z. Physik, 200, 186 (1967).

Canfield, L. R., G. Hass, and W. R. Hunter, J. de Physique, 25, 124 (1964).

Duncanson, A., and R. W. H. Stevenson, Proc. Phys. Soc. (London), 72, 1001 (1958).

Ehrenreich, H., H. R. Philipp, and B. Segall, Phys. Rev., 132, 1918 (1963).

Emerson, L. C., E. T. Arakawa, R. H. Ritchie, and R. D. Birkhoff, "Emission Spectra of Irradiated Metal Foils," Oak Ridge National Laboratory Report, ORNL-3450 (1963).

Evering, F. C., Applied Optics, 5, 1313 (1966).

Evering, F. C., and M. Aujouanne, Applied Optics, 8, 710 (1969).

Fano, U., J. Opt. Soc. Am., 31, 213 (1941).

Ferrell, R. A., Phys. Rev., 111, 1214 (1958).

Ferrell, R. A., and E. A. Stern, Am. J. Phys., 31, 810 (1962).

Fisher, E. I., I. Fujita, and G. L. Weissler, "Optical Constants of Silver and Barium in the Vacuum Ultraviolet Spectral Region," University of Southern California, Technical Report No. USC-VacUV-108 (1966).

Frank, I., and V. Ginsburg, J. of Physics, 9, 353 (1945).

Garber, F. W., J. A. Harter, R. D. Birkhoff, and R. H. Ritchie, "Low Energy Electron Beam Studies in Thin Metal Films," Oak Ridge National Laboratory, ORNL-TM-2406 (1969).

Hägglund, J., and F. Sellberg, J. Opt. Soc. Am., 56, 1031 (1966).

Hamm, R. N., R. A. MacRae, and E. T. Arakawa, J. Opt. Soc. Am., 55, 1460 (1965).

Hass, G., Z. Anorg. u. Allgem. Chem., 254, 96 (1947).

Hass, G., J. Opt. Soc. Am., 39, 532 (1949).

Hass, G., and M. E. McFarland, J. Appl. Phys., 21, 436 (1950).

Hass, G., and J. E. Waylonis, J. Opt. Soc. Am., 51, 719 (1961).

Hessel, A, and A. A. Oliner, Applied Optics, 4, 1275 (1965).

Holland, L., Vacuum Deposition of Thin Films (Chapman and Hall, Ltd., London, 1961), pp. 208, 244.

Huebner, R. H., E. T. Arakawa, R. N. Hamm, and R. A. MacRae, "Optical Constants of Evaporated Metal Films of Silver and Indium," Oak Ridge National Laboratory, ORNL-TM-1104 (1965).

Hunter, W. R., J. de Physique, 25, 154 (1964).

Jarrell, R. F. and G. W. Stroke, Applied Optics, 3, 1251 (1964).

Jenkins, F. A. and H. E. White, Fundamentals of Optics, (McGraw-Hill Book Co., New York, 1957), p. 520.

Kittel, C., Introduction to Solid State Physics, 3rd Ed., (John Wiley and Sons, Inc., New York, 1966), pp. 253-265.

Kliewer, K. L. and R. Fuchs, Phys. Rev., 153, 498 (1967).

Kloos, T., Z. Physik, 208, 77 (1968).

Kretschmann, E. and H. Raether, Z. Naturforschung, 22a, 1623 (1967).

Kretschmann, E. and H. Raether, Z. Naturforschung, 23a, 2135 (1968).

Lindhard, J., J. Kgl. Danske-Videnskab, Selskab, Mat.-Fys. Medd., 28, 8 (1964).

McAlister, A. J. and E. A. Stern, Phys. Rev., 132, 1599 (1963).

Otto, A., Z. Physik, 216, 398 (1968).

Painter, L. R., R. D. Birkhoff, and E. T. Arakawa, "Electronic Properties of Liquid Water in the Vacuum Ultraviolet Region," Oak Ridge National Laboratory, ORNL-TM-2261 (1968).

Palmer, C. H., J. Opt. Soc. Am., 42, 269 (1952).

Palmer, C. H., J. Opt. Soc. Am., 46, 50 (1956).

Palmer, C. H., F. C. Evering, and F. M. Nelson, Applied Optics, 4, 1271 (1965).

Pines, D., Rev. Mod. Phys., 28, 184 (1956).

Pines, D., Elementary Excitations in Solids, (W. A. Benjamin, Inc., 1963).

Raether, H., Solid State Excitation by Electrons, Springer Tracts in Modern Physics, Vol. 38 (Springer-Verlag, Berlin, 1965).

Rayleigh, Phil. Mag., 14, 60 (1907a).

Rayleigh, Proc. Royal Soc. (London), A,79, 399 (1907b).

Ritchie, R. H., Phys. Rev., 106, 874 (1957).

Ritchie, R. H. and H. B. Eldridge, Phys. Rev., 126, 1935 (1962).

Ritchie, R. H. and R. E. Wilems, Phys. Rev., 178, 372 (1969).

Ritchie, R. H., E. T. Arakawa, J. J. Cowan, and R. N. Hamm, Phys. Rev. Letters, 21, 1530 (1968).

Romanov, Y. A., Izvestiya Vuzov-Radiophysics, 7, 828 (1964).

Schultz, L. G. and F. R. Tangherlini, J. Opt. Soc. Am., 44, 362 (1954).

Schultz, L. G., J. Opt. Soc. Am., 44, 357 (1954).

Schmuzer, P., Z. Physik, 180, 105 (1964).

Schreiber, P. and H. Raether, Z. Naturforschung, 21a, 2116 (1966).

Shieh, S., Z. Physik, 217, 406 (1968a).

Shieh, S., Phys. Rev., 172, 1310 (1968b).

Sommerfeld, A., Ann. Physik, 28, 665 (1909).

Steinmann, W., Phys. Rev. Letters, 5, 470 (1960).

Steinmann, W., J. Hofmann, and K. Stettmaier, Phys. Rev. Letters, 23, 234 (1966).

Steinmann, W., Phys. Stat. Sol., 28, 437 (1968).

Stern, E. A. and R. A. Ferrell, Phys. Rev., 120, 130 (1960).

Stern, E. A., comment in Optical Properties and Electronic Structure of Metals and Alloys, edited by F. Abeles (North-Holland Publishing Co., Amsterdam, 1966), p. 397.

Stern, E. A., Phys. Rev. Letters, 19, 1321 (1967).

Stewart, J. E. and W. S. Gallaway, Applied Optics, 1, 421 (1962).

Stratton, J. A., Electromagnetic Theory, (McGraw-Hill Book Co., New York, 1941), pp. 573-587.

Swan, J. B., A. Otto, and H. Fellenzer, Phys. Stat. Sol., 23, 171 (1967).

Teng, Y., and E. A. Stern, Phys. Rev. Letters, 19, 511 (1967a).

Teng, Y. and E. A. Stern, "Plasma Radiation from Metal Grating Surfaces," University of Maryland Technical Report No. 749 (1967b).

Twersky, V., J. Appl. Phys., 23, 1099 (1952).

Twersky, V., J. Opt. Soc. Am., 52, 145 (1962).

Walkenhorst, W., Z. f. Techn. Physik, 22, 14 (1941).

Wilems, R. E. and R. H. Ritchie, Phys. Rev. Letters, 19, 1325 (1967).

Wilems, R. E. and R. H. Ritchie, "Non-Linear Interactions in Quantum Plasmas," Oak Ridge National Laboratory, ORNL-TM-2101 (1968).

Wood, R. W., Phil. Mag., 4, 396 (1902).

Wood, R. W., Phil. Mag., 23, 310 (1912).

Wood, R. W., Phys. Rev., 48, 928 (1935).

APPENDIXES

APPENDIX A

We present here the derivation of the classical dispersion relation [Equations (52) and (53)] for a bound surface plasma wave (TM electromagnetic wave) on a dielectric coated metal surface (Figure 5c, page 35). The method is the same as that used by Otto (1965) and Kloos (1968).

The electric fields for the surface plasma wave have the following form:

$$\vec{E} = e^{i(\kappa x-\omega t)} \begin{cases} \vec{A}\, e^{-k_1 z} & z > a \\ \vec{B}\, e^{-k_2 z} + \vec{C}\, e^{k_2 z} & 0 \leq z \leq a \\ \vec{D}\, e^{k_2 z} & z < 0 \end{cases} \qquad \text{(A1)}$$

$$\vec{E} = (E_x,\ 0,\ E_z)$$

$$k_1 = \sqrt{\kappa^2 - \frac{\omega^2}{c^2}} \qquad k_2 = \sqrt{\kappa^2 - \eta\,\frac{\omega^2}{c^2}} \qquad k_3 = \sqrt{\kappa^2 - \varepsilon\,\frac{\omega^2}{c^2}}\ .$$

These solutions satisfy the wave equations

$$\nabla^2 \vec{E} - \frac{1}{c^2}\,\frac{\partial^2 \vec{E}}{\partial t^2} = 0 \qquad \text{for} \quad z > a$$

$$\nabla^2 \vec{E} - \frac{\eta}{c^2}\,\frac{\partial^2 \vec{E}}{\partial t^2} = 0 \qquad \text{for} \quad 0 \leq z \leq a$$

$$\nabla^2 \vec{E} - \frac{\varepsilon}{c^2} \frac{\partial^2 E}{\partial t^2} = 0 \quad \text{for } z < 0 \quad .$$

In a homogeneous, charge-free medium we may write

$$\nabla \cdot \vec{E} = 0 \quad .$$

From which we have

$$\begin{aligned} i\kappa A_x - k_1 A_z &= 0 \qquad & i\kappa C_x + k_2 C_z &= 0 \\ i\kappa B_x - k_2 B_z &= 0 \qquad & i\kappa D_x + k_3 D_z &= 0 \end{aligned} \quad . \tag{A2}$$

At the boundaries the tangential component of the electric field, $\vec{E}$, and the normal component of the displacement field, $\vec{D}$, must be continuous. Thus we have

$$\begin{aligned} A_x e^{-k_1 a} &= B_x e^{-k_2 a} + C_x e^{k_2 a} \\ D_x &= B_x + C_x \\ A_z e^{-k_1 a} &= \eta(B_z e^{-k_2 a} + C_z e^{k_2 a}) \\ \varepsilon D_z &= \eta(B_z + C_z) \quad . \end{aligned} \tag{A3}$$

Combining (A2) and (A3), we can write the z-components of the field strength

$$
\begin{aligned}
k_1 e^{-k_1 a} A_z - k_2 e^{-k_2 a} B_z + k_2 e^{k_2 a} C_z &= 0 \\
- k_2 B_z + k_2 C_z - k_3 D_z &= 0 \\
e^{-k_1 a} A_z - \eta e^{k_2 a} B_z - \eta e^{k_2 a} C_z &= 0 \\
- \eta B_z - \eta C_z + \varepsilon D_z &= 0
\end{aligned}
\quad . \qquad (A4)
$$

This system of homogeneous equations yields a non-zero solution for the fields if its determinant vanishes. The dispersion relation, Equation (52), results from this calculation. Equation (53) results from the same procedure if we let $k_2 \to i\, k_2'$.

Dispersion curves were most easily obtained by solving for the thickness so that (52) and (53) have the following form

$$
\tanh (k_2 \tau) = \frac{-\eta\, k_2 (k_3 + \epsilon k_1)}{\varepsilon\, k_2^2 + \eta^2 k_1 k_3} \qquad k_2 = \sqrt{\kappa^2 - \eta \frac{\omega^2}{c^2}}
$$

$$
\tan (k_2' \tau) = \frac{\eta\, k_2' (k_3 + \varepsilon k_1)}{\varepsilon\, k_2'^2 - \eta^2 k_1 k_3} \qquad k_2' = \sqrt{\eta \frac{\omega^2}{c^2} - \kappa^2} \; .
$$

Explicit solutions for τ were obtained for a given value of ω by letting k take on a large number of values beginning at the zero dielectric thickness line, $\kappa = \frac{\omega}{c} \left(\frac{\varepsilon_1}{1+\varepsilon_1} \right)^{1/2}$, and extending in small equal increments to the infinite dielectric thickness line $\kappa = \frac{\omega}{c} \left(\frac{\varepsilon_1 \eta_1}{\eta_1 + \varepsilon_1} \right)^{1/2}$. These calculations were performed on the CDC 1604-A computer.

APPENDIX B

We show here the expansion of the matrix equation (58) for the case of a dielectric coated metal layer bounded by a second dielectric coated metal layer (Figure 5c, page 35). The general terms become, for this case,

$$a_o = \eta k_o + k_1 \qquad b_o = \eta k_o - k_1$$

$$a_1 = \varepsilon k_1 + \eta k_2 \qquad b_1 = \varepsilon k_1 - \eta k_2$$

$$a_2 = \eta k_2 + \varepsilon k_3 \qquad b_2 = \eta k_2 - \varepsilon k_3$$

$$\varepsilon_{n+1} k_n - \varepsilon_n k_{n+1} \to \varepsilon k_3 - \eta k_2 = x_1$$

$$\varepsilon_{n+1} k_n + \varepsilon_n k_{n+1} \to \varepsilon k_3 + \eta k_2 = x_2$$

where

$$k_o = \sqrt{\kappa^2 - \frac{\omega^2}{c^2}} \qquad k_1 = \sqrt{\kappa^2 - \eta\frac{\omega^2}{c^2}} \qquad k_2 = \sqrt{\kappa^2 - \varepsilon\frac{\omega^2}{c^2}}$$

and (58) becomes

$$\left(b_o e^{-k_1\tau_1} \quad a_o e^{k_1\tau_1}\right)\begin{pmatrix} a_1 e^{-k_2 d} & b_1 e^{k_2 d} \\ b_1 e^{-k_2 d} & a_1 e^{k_2 d} \end{pmatrix}\begin{pmatrix} a_2 e^{k_1\tau_2} & b_2 e^{k_1\tau_2} \\ b_2 e^{-k_1\tau_1} & a_2 e^{k_1\tau_2} \end{pmatrix}\begin{pmatrix} x_1 \\ x_2 \end{pmatrix} = 0.$$

When this is expanded we obtain

$$b_o\, b_1\, e^{-k_1\tau_1 - k_1\tau_2}\,(-\, b_1^{\,2}\, e^{k_2 d} + a_1^{\,2}\, e^{-k_2 d})$$

$$+\; b_o\, a_1\, e^{-k_1\tau_1 + k_1\tau_2}\,(b_1\, a_1\, e^{k_2 d} - a_1\, b_1\, e^{-k_2\, d})$$

$$+\; a_o\, b_1\, e^{k_1\tau_1 - k_1\tau_2}\,(-a_1\, b_1\, e^{k_2 d} + b_1\, a_1\, e^{-k_2 d})$$

$$+\; a_o\, a_1\, e^{k_1\tau_1 + k_1\tau_2}\,(a_1^{\,2}\, e^{k_2 d} - b_1^{\,2}\, e^{-k_2 d}) = 0$$

Expansion and rearrangement of terms leads to Equation (59) and substitution of $k_1 \rightarrow ik_1'$ leads to Equation (60).

APPENDIX C

In the interaction described by Figure 6c, page 65, and Equation (78), one defines the initial and final states by

$$|i> = \frac{1}{\sqrt{N_{\vec{k},\lambda}}} (\hat{c}^{+}_{\vec{k},\lambda})^{N_{\vec{k},\lambda}} |0>$$

$$|f> = \frac{1}{\sqrt{(N_{\vec{k},\lambda} - 1)!}} \hat{c}^{+}_{\vec{k}',\lambda'} (\hat{c}^{+}_{\vec{k},\lambda})^{N_{\vec{k},\lambda} - 1} |0>$$

and the intermediate states by

$$|I> = \frac{1}{\sqrt{(N_{\vec{k},\lambda} - 1)!}} \hat{b}^{+}_{\vec{\kappa}} (\hat{c}^{+}_{\vec{k},\lambda})^{N_{\vec{k},\lambda} - 1} |0>$$

$$|I'> = \frac{1}{\sqrt{(N_{\vec{k},\lambda} - 1)!}} \hat{b}^{+}_{\vec{\kappa}'} (\hat{c}^{+}_{\vec{k},\lambda})^{N_{\vec{k},\lambda} - 1} |0>$$

where $\hat{b}^{+}$ and $\hat{c}^{+}$ are the creation operators for the surface plasmon and photon, respectively. $N_{\vec{k},\lambda}$ is the number of photons in state $\vec{k},\lambda$, and $|0>$ is the vacuum state. The Hamiltonians, $H^{(1)}_{RNP}$ and $H_{NP-NP-SDV}$, contain both creation and destruction and destruction operators for the photon and the surface plasmon [Wilems and Ritchie (1968)]. The summation over the surface plasmon intermediate states yields

$$\mathrm{III} = \frac{a\hbar^3}{8L^3} N_{\vec{k},\lambda}^{1/2} (\hat{e}_{\vec{k}',\lambda'} \cdot \hat{z})(\hat{e}_{\vec{k},\lambda} \cdot \hat{z})\, g(\vec{k}_\rho - \vec{k}'_\rho)$$

$$\times \frac{\omega_p^4}{(\omega\omega')^{1/2} (\omega - \omega_p + i\frac{\gamma'}{2})(\omega - \omega_p + i\frac{\gamma}{2})}$$

where the autocorrelation function, $g(\vec{k}_\rho - \vec{k}'_\rho)$, includes the effects of the SDV.

APPENDIX D

COMPUTER CODE LISTINGS

```
      PROGRAM DISPREL

C     DISPERSION RELATION FOR METAL FOIL,NORMAL AND TANGENTIAL
C     MODES,EQUATION (47), READ ENERGY IN EV, THICKNESS IN ANGSTROMS

      TYPE REAL KSQ,K
    1 READ 2,E,EP
    2 FORMAT(2F10.0)
      W=50678.48*E
      WSQ=W*W
      K=W
      PRINT 3,E,EP
    3 FORMAT(1H1,9HENERGY = ,F6.2,5X,4HE = ,F7.2/)
      PRINT 13
   13 FORMAT(1H ,10X,1HK,11X,8HD NORMAL,11X,12HD TANGENTIAL/)
      AINF=SQRTF(WSQ*EP/(1.0+EP))
      DO 4I=1,200
      KSQ=K*K
      A1=KSQ-WSQ
      B1=KSQ-EP*WSQ
      A=SQRTF(A1)
      B=SQRTF(B1)
      X=-EP*A/B
      IF(K.LT.AINF)9,10
    9 XT=-0.5*LOGF(ABSF((1.0-X)/(1.0+X)))
      DN=(2.0*XT/B)*(1.0E+8)
      PRINT 7,K,DN
    7 FORMAT(1H ,E15.3,5X,E10.3)
      GO TO 4
   10 XC=-0.5*LOGF(ABSF((X-1.0)/(X+1.0)))
      DT=(2.0*XC/B)*(1.0E+8)
      PRINT 8,K,DT
    8 FORMAT(1H ,E15.3,26X,E10.3)
    4 K=K+250.
      GO TO 1
      END
```

```
      PROGRAM DISPREL

C     DISPERSION RELATION FOR DIELECTRIC LAYER ON METAL SLAB,
C     EQUATIONS (52) AND (53). LOWER ENERGY REGION.  K TERMINATES
C     AT INFINITE DIELECTRIC THICKNESS

      TYPE REAL KSQ,K
    1 READ 2,E,EP,ETA
    2 FORMAT(4F10.0)
      WSQ=(50678.48*E)**2
      K=SQRTF(WSQ*EP/(1.0+EP))
      PRINT 3,E,EP,ETA
    3 FORMAT(1H1,9HENERGY = ,F6.2,5X,4HE = ,F7.2,5X,6HETA = ,F7.2/)
      PRINT 13
   13 FORMAT(1H ,10X,1HK,11X,1HT/)
      AMAX=SQRTF(WSQ*EP*ETA/(ETA+EP))
      AK=K+250000.
      IF(AK.LT.AMAX)14,15
   14 IMAX=500
      GO TO 16
   15 IMAX=(AMAX-K)/500.
   16 DO 4I=1,IMAX
      KSQ=K*K
      A1=KSQ-WSQ
      B1=ETA*SQ-KSQ
      C1=KSQ-EP*WSQ
      A=SQRTF(A1)
      C=SQRTF(C1)
      IF(A1.LT.0.0.OR.B1.LT.0.0)9,10
   10 B=SQRTF(B1)
      TN=ETA*B*(C+EP*A)/(EP*B*B-ETA*ETA*A*C)
      X=ATANF(TN)
      GO TO 12
    9 B=SQRTF(-B1)
      TN=-ETA*B*(C+EP*A)/(EP*B*B+ETA*ETA*A*C)
      X=-0.5*LOGF(ABSF((1.0-TN)/(1.0+TN)))
   12 T=(X/B)*(1.0E+8)
      PRINT 7,K,T,B1
    7 FORMAT(1H ,E15.3,5X,E10.3,10X,E10.2)
    4 K=K+500.
      GO TO 1
      END
```

```
      PROGRAM DISPREL

C     DISPERSION RELATION FOR METAL LAYER ON DIELECTRIC COATED METAL
C     SLAB, EQUATIONS (56) AND (57). LOWER ENERGY REGION. K TERMINATES
C     AT INFINITE DIELECTRIC THICKNESS

      TYPE REAL KSQ,K,NUM
    1 READ 2,E,EP,ETA,D
    2 FORMAT(4F10.0)
      W=50678.48*E
      WSQ=W*W
      K=W
      PRINT 3,E,EP,ETA,D
    3 FORMAT(1H1,9HENERGY = ,F6.2,5X,4HE = ,F7.2,5X,6HETA = ,F7.2,
     1      5X,4HD = ,F7.2/)
      PRINT 13
   13 FORMAT(1H ,10X,1HK,14X,1HT,20X,2HC1/)
      AMAX=SQRTF(WSQ*EP*ETA/(ETA+EP))
      AK=K+125000.
      IF(AK.LT.AMAX)14,15
   14 IMAX=500
      GO TO 16
   15 IMAX=(AMAX-K)/250.
   16 DO 4I=1,IMAX
      KSQ=K*K
      A1=KSQ-WSQ
      B1=KSQ-EP*WSQ
      C1=ETA*WSQ-KSQ
      A=SQRTF(A1)
      B=SQRTF(B1)
      EX=EXP(-2.0E-8*B*D)
      IF(C1.LT.0.0)9,10
    9 C=SQRTF(-C1)
      NUM=2.0*ETA*EP*B*C*(EP*A+B)
      DN1=(EP**3)*A*C*C+ETA*ETA*(B**3)
      DN2=ETA*ETA*A*B+EP*C*C
      TNH=NUM/(DN1*(EX-1)-EP*B*DN2*(EX+1))
      Y=-0.5*LOGF(ABSF((1.0-TNH)/(1.0+TNH)))
      GO TO 11
   10 C =SQRTF(C1)
      NUM=2.0*ETA*EP*B*C*(EP*A+B)
```

```
      DN1=ETA*ETA*(B**3)-(EP**3)*A*C*C
      DN2=ETA*ETA*A*B-EP*C*C
      TN=NUM/(DN1*(EX-1)-EP*B*DN2*(EX+1))
      Y=ATANF(TN)
   11 T=(Y/C)*(1.0E+8)
      PRINT 7,K,T,C1
    7 FORMAT(1H ,E15.3,5X,E10.3,10X,E10.3)
    4 K=K+250.
      GO TO 1
      END
```

```
      PROGRAM DISPREL

C     DISPERSION RELATION FOR DIELECTRIC LAYER ON METAL LAYER ON
C     DIELECTRIC LAYER ON METAL SLAB, EQUATIONS (59) AND (60), USES
C     COMPLEX DIELECTRIC CONSTANT FOR DIELECTRIC LAYER

      TYPE REAL KSQ,K
      TYPE COMPLEX ETA,B1,B,AA,AB,AC,AD,AE,AF,AG,AH,CS1,SN1,CS2,
     1    SN2,CS12,SN12,AN1,AN2,AN3,AN4,AN5,AN6,DN1,DN2,EX,Y,D
    1 READ 2,E,EP,ETA,T1,T2
    2 FORMAT (2F10.0,C(F10.0,F10.0),2F10.0)
      W=50678.48*E
      WSQ=W*W
      K=W
      PRINT 3,E,EP,ETA,T1,T2
    3 FORMAT (1H1,9HENERGY = ,F6.2,5X,4HE = ,F7.2,5X,6HETA = ,
     1      C(F7.2,F10.2),5X,5HT1 = ,F7.2,5X,5HT2 = ,F7.2/)
      DO 4I=1,500
      KSQ=K*K
      A1=KSQ-WSQ
      B1=ETA*WSQ-KSQ
      C1=KSQ-EP*WSQ
      A=SQRTF(A1)
      C=SQRTF(C1)
      AD=(ETA**4)*A*(C**3)
      IF((REAL(B1)).LT.0.0)9,10
    9 B=CSQRT(-B1)
      AA=ETA*(EP**3)*A*(B**3)
      AB=ETA*ETA*EP*EP*A*B*B*C
      AC=(ETA**3)*EP*A*B*C*C
      AE=(EP**3)*(B**4)
      AF=ETA*EP*EP*(B**3)*C
      AG=ETA*ETA*EP*B*B*C*C
      AH=(ETA**3)*B*C*C
      CS1=0.5*(CEXP(B*T1*1.0E-8)+CEXP(-B*T1*1.0E-8))
      SN1=0.5*(CEXP(B*T1*1.0E-8)-CEXP(-B*T1*1.0E-8))
      CS2=0.5*(CEXP(B*T2*1.0E-8)+CEXP(-B*T2*1.0E-8))
      SN2=0.5*(CEXP(B*T2*1.0E-8)-CEXP(-B*T2*1.0E-8))
      CS12=0.5*(CEXP(B*(T1+T2)*1.0E-8)+CEXP(-B*(T1+T2)*1.0E-8))
      SN12=0.5*(CEXP(B*(T1+T2)*1.0E-8)-CEXP(-B*(T1+T2)*1.0E-8))
      AN1=(AA+AH)*CS1*SN2
```

```
      AN2=(AD+AE)*SN1*SN2
      AN3=(AB+AG)*CS1*CS2
      AN4=(AC+AF)*SN1*CS2
      AN5=(AB+AG)*CS12
      AN6=(AC+AF)*SN12
      DN1=(AB+AG)*SN1*SN2
      DN2=(AC+AF)*CS1*SN2
      EX=(AN1+AN2+AN3+AN4+AN5+AN6)/(AN1+AN2-DN1-DN2)
      GO TO 11
   10 B=CSQRT(B1)
      AA=ETA*(EP**3)*A*(B**3)
      AB=ETA*ETA*EP*EP*A*B*B*C
      AC=(ETA**3)*EP*A*B*C*C
      AE=(EP**3)*(B**4)
      AF=ETA*EP*EP*(B**3)*C
      AG=ETA*ETA*EP*B*B*C*C
      AH=(ETA**3)*B*C*C
      CS1=CCOS(B*T1*1.0E-8)
      SN1=CSIN(B*T1*1.0E-8)
      CS2=CCOS(B*T2*1.0E-8)
      SN2=CSIN(B*T2*1.0E-8)
      CS12=CCOS(B*(T1+T2)*1.0E-8)
      SN12=CSIN(B*(T1+T2)*1.0E-8)
      AN1=(AA-AH)*CS1*SN2
      AN2=(AD+AE)*SN1*SN2
      AN3=(AB+AG)*CS1*CS2
      AN4=(AC-AF)*SN1*CS2
      AN5=(AB+AG)*CS12
      AN6=(AC-AF)*SN12
      DN1=(AB+AG)*SN1*SN2
      DN2=(AC-AF)*CS1*SN2
      EX=(AN1-AN2-AN3-AN4-AN5-AN6)/(AN1-AN2-DN1+DN2)
   11 Y=-CLOG(EX)
      D=(Y/(2.0*C))*(1.0E+8)
      PRINT 7,K,D,B1
    7 FORMAT (1H ,E15.3,5X,C(E10.3,E14.3),10X,C(E10.3,E14.3))
    4 K=K+7500.
      GO TO 1
      END
```

```
      PROGRAM DISPREL

C     DISPERSION RELATION FOR METAL FOIL BOUNDED BY UNEQUAL
C     DIELECTRIC THICKNESSES,  EQUATIONS (61) AND (62)

      COMMON A,B,B1,ETA
      TYPE REAL KSQ,K
    1 READ 2,E,EP,ETA,T1,T2
    2 FORMAT(5F10.0)
      W=50678.48*E
      WSQ=W*W
      K=W
      PRINT 3,E,EP,ETA,T1,T2
    3 FORMAT(1H1,9HENERGY = ,F6.2,5X,5HEP = ,F7.2,5X,6HETA = ,F7.2,5X,
     1     5HT1 = .F5.0,5X,5HT2 = ,F5.0/)
      PRINT 13
   13 FORMAT(1H ,10X,1HK,11X,1HD/)
      AMAX=SQRTF(WSQ*EP*ETA/(ETA+EP))
      AK=K+125000.
      IF(AK.LT.AMAX)14,15
   14 IMAX=500
      GO TO 16
   15 IMAX=(AMAX-K)/250.
   16 DO 4I=1,IMAX
      KSQ=K*K
      A1=KSQ-WSQ
      B1=ETA*WSQ-KSQ
      C1=KSQ-EP*WSQ
      IF(B1.LT.0.0)9,10
    9 B=SQRTF(-B1)
      GO TO 11
   10 B=SQRTF(B1)
   11 TNH=(EP*ETA*C*(G(T1)+G(T2))/B)/
     1     (-EP*EP*G(T1)*G(T2)-ETA*ETA*C*C/(B*B))
      Y=-0.5*LOGF(ABSF((1.0-TNH)/(1.0+TNH)))
      D=(Y/C)*(1.0E+8)
      PRINT 7,K,D,B1
    7 FORMAT(1H ,E15.3,5X,E10.3,10X,E10.3)
    4 K=K+500.
      GO TO 1
```

```
      END DISPREL
      FUNCTION G(X)
      COMMON A,B,B1,ETA
      IF(B1.LT.0.0)15,16
   15 TN=TANH(B*X*1.0E-8)
      G=(ETA*A+B*TN)/(ETA*A*TN+B)
      RETURN
   16 TN=TAN(B*X*1.0E-8)
      G=(ETA*A-B*TN)/(ETA*A*TN+B)
      END
```

```
      PROGRAM DISPREL

C     DISPERSION RELATION FOR DOUBLE DIELECTRIC LAYER ON METAL SLAB,
C     EQUATIONS (63)-(66). K INTERVAL SMALL BELOW 3.0 EV AND LARGE
C     ABOVE 3.0 EV. USES REAL PARAMETERS

      TYPE REAL KSQ,K,NU
    1 READ 2,E,EP,ETA,NU,T2
    2 FORMAT (5F10.0)
      W=50678.48*E
      WSQ=W*W
      K=W
      PRINT 3,E,EP,ETA,NU,T2
    3 FORMAT(1H1,9HENERGY = ,F6.2,5X,4HE = ,F7.2,5X,6HETA = ,
     1      F7.2,5X,5HNU = ,F7.2,5X,5HT2 = ,F7.2/)
      PRINT 13
   13 FORMAT(1H ,10X,1HK,14X,2HT1,20X,2HB1,20X,2HC1/)
      IF(E.LT.3.00)12,17
   12 AMAX=SQRTF(WSQ*EP*ETA/(ETA+EP))
      AK=K+125000.
      XINC=250.
      IF(AK.LT.AMAX)14,15
   17 XINC=7500.
   14 IMAX=500
      GO TO 16
   15 IMAX=(AMAX-K)/250.
   16 DO 4I=1,IMAX
      KSQ=K*K
      A1=KSQ-WSQ
      B1=NU*WSQ-KSQ
      C1=ETA*WSQ-KSQ
      D1=KSQ-EP*WSQ
      A=SQRTF(A1)
      D=SQRTF(D1)
      IF(B1.LT.0.0)9,10
    9 IF(C1.LT.0.0)21,22
   21 B=SQRTF(-B1)
      C=SQRTF(-C1)
      GO TO 11
   22 B=SQRTF(-B1)
      C=SQRTF(C1)
      GO TO 11
```

```
10 IF(C1.LT.0.0)23,24
23 B=SQRTF(B1)
   C=SQRTF(-C1)
   GO TO 11
24 B=SQRTF(B1)
   C=SQRTF(C1)
11 AA=ETA*NU*EP*A*B*C
   AB=NU*NU*EP*A*C*C
   AC=ETA*EP*B*B*C
   AD=NU*EP*B*C*C
   AE=ETA*ETA*NU*A*B*D
   AF=NU*NU*ETA*A*C*D
   AG=ETA*ETA*B*B*D
   AH=NU*ETA*B*C*D
   IF(B1.LT.0.0)19,20
19 IF(C1.LT.0.0)31,32
31 TN=TANH(C*T2*1.0E-8)
   TNH=(-(AA+AH)-(AD+AE)*TN)/((AC+AF)+(AB+AG)*TN)
   Y=-0.5*LOGF(ABSF((1.0-TNH)/(1.0+TNH)))
   GO TO 41
32 TN=TANF(C*T2*1.0E-8)
   TNH=(-(AA+AH)+(AD-AE)*TN)/((AC+AF)+(-AB+AG)*TN)
   Y=-0.5*LOGF(ABSF((1.0-TNH)/(1.0+TNH)))
   GO TO 41
20 IF(C1.LT.0.0)33,34
33 TN=TANH(C*T2*1.0E-8)
   TNH=(-(AA+AH)-(AD+AE)*TN)/((-AC+AF)+(AB-AG)*TN)
   Y=ATANF(TNH)
   GO TO 41
34 TN=TANF(C*T2*1.0E-8)
   TNH=((AA+AH)-(AD-AE)*TN)/((AC-AF)+(AB+AG)*TN)
   Y=ATANF(TNH)
   GO TO 41
41 T1=(Y/B)*(1.0E+8)
   PRINT 7,K,T1,B1,C1
 7 FORMAT (1H ,E15.3,5X,E10.3,10X,E10.3,10X,E10.3)
 4 K=K+XINC
   GO TO 1
   END
```

```
      PROGRAM DISPREL

C     DISPERSION RELATION FOR DOUBLE DIELECTRIC LAYER ON METAL SLAB,
C     EQUATIONS (63)-(66). HIGH ENERGY REGION. USES REAL DIELECTRIC
C     CONSTANT FOR METAL AND ONE OF DIELECTRIC LAYERS-COMPLEX
C     DIELECTRIC CONSTANT FOR OTHER DIELECTRIC LAYER. REDUCES TO
C     EQUATIONS (52) AND (53) FOR T2=0.  CAN OBTAIN FIGURE 27 FOR
C     ALUMINUM OXIDE USING COMPLEX DIELECTRIC CONSTANT

      TYPE REAL KSQ,K
      TYPE COMPLEX NU,B1,B,AA,AB,AC,AD,AE,AF,AG,AH,TNH,Y,T1
    1 READ 2,E,EP,ETA,NU,T2
    2 FORMAT (3F10.0,C(F10.0,F10.0),F10.0)
      W=50678.48*E
      WSQ=W*W
      K=W
      PRINT 3,E,EP,ETA,NU,T2
    3 FORMAT(1H1,9HENERGY = ,F6.2,5X,4HE = ,F7.2,5X,6HETA = ,
     1     F7.2,5X,5HNU = ,C(F7.2,F10.2),5X,5HT2 = ,F7.2/)
      PRINT 13
   13 FORMAT(1H ,10X,1HK,14X,2HT1,30X,2HB1,30X,2HC1/)
      DO 4I=1,500
      KSQ=K*K
      A1=KSQ-WSQ
      B1=NU*WSQ-KSQ
      C1=ETA*WSQ-KSQ
      D1=KSQ-EP*WSQ
      A=SQRTF(A1)
      D=SQRTF(D1)
      IF((REAL(B1)).LT.0.0)9,10
    9 IF(C1.LT.0.0)21,22
   21 B=CSQRT(-B1)
      C=SQRTF(-C1)
      GO TO 11
   22 B=CSQRT(-B1)
      C=SQRTF(C1)
      GO TO 11
   10 IF(C1.LT.0.0)23,24
   23 B=CSQRT(B1)
      C=SQRTF(-C1)
      GO TO 11
```

```
24 B=CSQRT(B1)
   C=SQRTF(C1)
11 AA=ETA*NU*EP*A*B*C
   AB=NU*NU*EP*A*C*C
   AC=ETA*EP*B*B*C
   AD=NU*EP*B*C*C
   AE=ETA*ETA*NU*A*B*D
   AF=NU*NU*ETA*A*C*D
   AG=ETA*ETA*B*B*D
   AH=NU*ETA*B*C*D
   IF((REAL(B1)).LT.0.0)19,20
19 IF(C1.LT.0.0)31,32
31 TN=TANH(C*T2*1.0E-8)
   TNH=(-(AA+AH)-(AD+AE)*TN)/((AC+AF)+(AB+AG)*TN)
   Y=-0.5*CLOG((1.0-TNH)/(1.0+TNH))
   GO TO 41
32 TN=TANF(C*T2*1.0E-8)
   TNH=(-(AA+AH)+(AD-AE)*TN)/((AC+AF)+(-AB+AG)*TN)
   Y=-0.5*CLOG((1.0-TNH)/(1.0+TNH))
   GO TO 41
20 IF(C1.LT.0.0)33,34
33 TN=TANH(C*T2*1.0E-8)
   TNH=(-(AA+AH)-(AD+AE)*TN)/((-AC+AF)+(AB-AG)*TN)
   Y=CATAN(TNH)
   GO TO 41
34 TN=TANF(C*T2*1.0E-8)
   TNH=((AA+AH)-(AD-AE)*TN)/((AC-AF)+(AB+AG)*TN)
   Y=CATAN(TNH)
   GO TO 41
41 T1=(Y/B)*(1.0E+8)
   PRINT 7,K,T1,B1,C1
 7 FORMAT (1H ,E15.3,5X,C(E10.3,E14.3),10X,C(E10.3,E14.3),10X,E10.3)
 4 K=K+7500.
   GO TO 1
   END
```

INTERNAL DISTRIBUTION

1-2. Central Research Library (CRL)
3. Document Ref. Section (DRS)
4-18. Laboratory Records (LRD)
19. Laboratory Records (ORNL RC)
20. ORNL Patent Office
21-45. E. T. Arakawa
46-55. R. D. Birkhoff
56. A. E. Carter
57. L. G. Christophorou
58. R. N. Compton
59-83. J. J. Cowan
84. F. J. Davis
85. W. R. Garrett
86. R. N. Hamm
87. J. A. Harter
88. C. E. Klots
89. J. L. Liverman
90. H. G. MacPherson
91. W. J. McConnell
92-93. K. Z. Morgan
94. D. R. Nelson
95-119. R. H. Ritchie
120. H. C. Schweinler
121. W. S. Snyder
122. J. A. Stockdale
123. J. E. Turner
124. A. M. Weinberg
125. J. E. Cantlon (C)
126. C. D. Cooper (C)
127. J. C. Frye (C)
128. E. Gerjuoy (C)
129. J. B. Hursh (C)
130. G. S. Hurst (C)
131. J. L. Magee (C)
132. M. R. Williams (C)
133. H. O. Wyckoff (C)

EXTERNAL DISTRIBUTION

134. F. Abeles, Institute d'Optique, 3, Blvd. Pasteur, Paris, France.
135. N. Axelrod, Bell Telephone Laboratories, Murray Hill, N.J. 07971.
136. G. Arnett, Space Sciences Laboratory, SNE-SSL-TR, George C. Marshall Space Flight Center, Alabama.
137. R. L. Batdorf, Bell Telephone Laboratories, P.O. Box 241, Reading, Pa. 19603.
138. D. E. Bedo, Air Force Cambridge Research Lab., L. G. Hanscom Field, Bedford, Mass. 01730.
139. H. E. Bennett, Physics Optics Branch, Michelson Laboratory, U.S. Naval Ordnance Test Station, China Lake, California 94108.
140. A. J. Blodgett, Jr., I.B.M., East Fishkill, New York.
141. H. Boersch, I. Physikalischen Institut der Technischen Universitat, Berlin, W. Germany.
142. A. Bril, Phillips Eindhoven Project Department, Phillips Laboratory, Eindhoven, Netherlands.
143. P. Broquet, Faculte des Sciences, Paris, France.
144. Fred Brown, Department of Physics, University of Illinois, Urbana, Illinois 61801.
145. Thomas Callcott, Physics Department, University of Tennessee, Knoxville, Tennessee 37916.

146. Manuel Cardona, Physics Department, Brown University, Providence, Rhode Island 02912.
147. Y. Cauchois, Faculte des Sciences de Paris, 11, rue Pierre Curie, Paris, France.
148. W. H. Chambers, University of California, LASL, Box 1663, Los Alamos, New Mexico 87544.
149. M. L. Cohen, Physics Department, University of California, Berkeley, California 94720.
150. J. T. Cox, Night Vision Lab., USAECOM, Fort Belvoir, Virginia 22060.
151. J. R. Cuthill, Metallurgy Division, National Bureau of Standards, Washington, D.C. 20234.
152. Paul E. Dalbec, Dept. of Physics, The American University, Washington, D.C. 20016.
153. N. and H. Damany, CNRS, 1, Place Aristide-Briand, Bellevue, France.
154. R. N. Dexter, Department of Physics, 475 North Charter Street, The University of Wisconsin, Madison, Wisconsin 53706.
155. P. Dobberstein, Physikalisch-Technische Bundensanstalt, Berlin-Charlottenberg, Germany.
156. J. G. Dodd, Department of Physics, University of Tennessee, Knoxville, Tennessee 37916.
157. A. Ejiri, Institute of Physics, College of General Education, University of Tokyo, 865, Komaba, Megaro-ku, Tokyo, Japan.
158. Brother James Farrell, FSC, Physics Department, University of Notre Dame, Notre Dame, Indiana 46556.
159. B. Feuerbacher, Sektion Physik, der University Munchen, Germany.
160. H. A. Fowler, Electron Physics Section, National Bureau of Standards, Washington, D.C. 20234.
161. H. Fujita, Department of Physics, University of Illinois, Urbana, Illinois 61801.
162. John C. Garth, Radiation Effects Branch, Solid State Sciences Laboratory,Air Force Cambridge Research Labs., Laurence G. Hanscom Field, Bedford, Massachusetts 01730.
163. M. P. Givens, University of Rochester, Institute of Optics, Rochester, New York 14627.
164. Allen N. Goland, Physics Department, Brookhaven National Laboratory, Upton, L. I., New York 11973.
165. Paul M. Grant, IBM Corporation, Research Laboratory, Monterey and Cottle Roads, San Jose, California 95114.
166. R. Haensel, Physikalisches Staatsinstitut, II. Institut fur Experimental-physik, der Universitat Hamburg, Hamburg 50, Luruper Chausee 149, West Germany.
167. H. D. Hagstrum, Bell Telephone Labs., Murray Hill, New Jersey 07971.
168. W. F. Hanson, Apt. H-11, 301 Woodlawn Pike, Knoxville, Tenn. 31920.
169. G. Hass, U.S. Army Electronics Command, Fort Belvoir, Va. 22060.
170. J. David Hayes, 3402 Kavanaugh, Huntsville, Alabama 35810

171. R. J. Herickhoff, Apt. H-19, 1401 Monks Avenue, Mankato, Minn. 56001.
172. L. J. Heroux, AFCRL, L. G. Hanscom Field, Bedford, Mass. 01730.
173. D. C. Hinson, ITT Industrial Lab., Ft. Wayne, Indiana 46805.
174. Jerome Holiday, U.S. Steel Corp., Laboratory for Fundamental Research, Monroeville, Pennsylvania 15146.
175. R. H. Huebner, Division of Biology and Medicine, USAEC, Washington, D.C. 20545.
176. Dr. T. Huen, University of California, Lawrence Radiation Laboratory, L121, Box 808, Livermore, California 94550.
177. W. R. Hunter, U.S. Naval Research Laboratory, Washington, D.C. 20390.
178. Mitio Inokuti, Physics Department, Argonne National Laboratory, Argonne, Illinois 60439.
179. P. Jaegle, Laboratoire de Chimie Physique, Faculte des Sciences de Paris, Paris, France.
180. Mel Johnson, Bendix Corporation, Research Laboratory Division, 20800 10½ Mile Road, Southfield, Michigan 48076.
181. Wolfgang Klein, Night Vision Laboratory, U.S. Army Mobility Equipment Research and Development Center, Fort Belvoir, Va. 22060.
182. O. Klemperer, Imperial College, University of London, London, England.
183. C. Kunz, II. Institute for Experimental Physics, DESY, 2 Hamburg, Germany.
184. G. J. Lapeyre, Department of Physics, Montana State University, Bozeman, Montana 59715.
185. L. J. LeBlanc, University of Moncton, Moncton, N.B., Canada.
186. P. W. Levy, Brookhaven National Laboratory, Upton, L. I., New York.
187. R. E. LaVilla, Matls. B-212, National Bureau of Standards, Washington, D.C. 20234.
188. Dave Lynch, Physics Department, Iowa State University, Ames, Iowa.
189. R. A. MacRae, Physics Department, Jacksonville, State University, Jacksonville, Alabama.
190. R. P. Madden, Far UV Physics, Division 222, National Bureau of Standards, Washington, D.C. 20234.
191. L. Marton, National Bureau of Standards, 4515 Linnean Avenue, SW, Washington, D.C.
192. H. Mayer, Physikalisches Institut des Technischen Hoshchule, Clausthal, Germany.
193. H. Mendlowitz, Department of Physics, Howard University, Washington, D.C. 20001.
194. Kazuo P. Miyake, Inst. for Optical Research, Kyoiku University, Tokyo, Japan.
195. M. Y. Nakai, Osaka Laboratory, JAERI, 588 Mii, Neyagawa-City, Osaka, Japan.
196. Takeshi Namioka, Institute for Optical Research, Tokyo University of Education, 400 Hyakunintyo-4, Sinzyuku-ku, Tokyo, Japan.
197. A. H. Nielsen, Department of Physics, University of Tennessee, Knoxville, Tennessee 37916.

198. P.-O. Nilsson, Chalmers University of Technology, Department of Physics, Gibraltargatan 5B, Gotenburg, S Sweden.
199. J. F. Osantowski, Code 284, Bldg. 5, Room 14, Goddard Space Flight Center, Greenbelt, Maryland 20771.
200. A. Otto, II. Physikalisches Institut der Universitat Munchen, Munchen, W. Germany.
201. Mrs. L. Pajasova, Institute of Solid State Physics, Czechoslovak Academy of Science, Cukrovarnicka 10, Praha 6, Czechoslovakia.
202. J. C. Phillips, Institute for the Study of Metals, University of Chicago, Chicago, Illinois.
203. C. M. Pleass, Bell Telephone Laboratories, P. O. Box 241, Reading, Pennsylvania 19603.
204. W. A. Pliskin, IBM Components Division, East Fishkill, New York.
205. W. Pong, Department of Physics and Astronomy, University of Hawaii, Honolulu, Hawaii 96822.
206. C. J. Powell, Electron Physics Section, National Bureau of Standards, Washington, D. C. 20234.
207. F. Pradal, C.N.R.S., Faculte des Sciences, 118, route de Narbonne, 118, 31 - Toulouse 04, France.
208. H. Rabin, Solid State Division, U.S. Naval Research Lab., Washington, D.C. 20390.
209. H. Raether, Institute fur Angewandte Physik, Universitat Hamburg, Hamburg, Germany.
210. William A. Rense, Physics Department, University of Colorado, Boulder, Colorado 80304.
211. Mme. S. Robin, Laboratoire de Spectroscopie, Faculte des Sciences, Avenue du General Leclerc, 35 Rennes, France.
212. Mme. S. Robin-Kandare, Faculte des Sciences, Laboratoire de Physique, 34 - Montpelier, France.
213. D. M. Roessler, Bell Telphone Labs, Mountain Avenue, Murray Hill, N. J. 07974.
214. J. A. R. Samson, Geophysics Corporation of America, Experimental Physics Department, Bedford, Mass. 01730.
215. T. Sasaki, University of Tokyo, College of General Education, Komaba, Tokyo, Japan.
216. G. Sauerbrey, Physikalisch-Technische Bundensanstalt, Berlin-Charlottenburg, Germany.
217. E. J. Scheibner, Georgia Institute of Technology, Atlanta, Georgia.
218. S. E. Schnatterly, Department of Physics, Palmer Physical Laboratory, Princeton University, P. O. Box 708, Princeton, N.J. 08540.
219. W. J. Scouler, Solid State Physics, Massachusetts Institute of Technology, Lincoln Laboratory, Lexington, Massachusetts 02173.
220. S. Y. Shieh, Physics Department, University of Tennessee, Knoxville, Tenn. 37916.

221. B. Fitton, Surface Physics Division, European Space Research and Technology Center, Noordwijk, Holland.
222. M. Skibowski, Section Physik der Universitat Munchen, Munchen, Germany.
223. W. E. Spicer, Stanford Electronics Laboratory, Stanford University, Stanford, California.
224. J. L. Stanford, U.S. Naval Testing Station, China Lake, California.
225. W. Steinmann, Section Physik der Universitat Munchen, Munchen, Germany.
226. G. Stephan, Laboratorie de Spectroscopie, Faculte des Sciences, 1, Rue E. Rostand, Rennes, France.
227. J. R. Stevenson, Physics Department, Georgia Institute of Technology, Atlanta, Georgia.
228. J. B. Swan, Department of Physics, University of Western Australia, Nedlands, Western Australia.
229. Nils Swanson, West 103, National Bureau of Standards, Washington, D.C. 20234.
230. Ye-Yung Teng, Lowell Technological Institute, Lowell, Massachusetts 01854.
231. J. Toots, A-50 Physics Bldg., National Bureau of Standards, Washington, D.C. 20234.
232. R. C. Vehse, Bell Telephone Labs, P. O. Box 241, Reading, Pennsylvania 19603.
233. B. J. Waclawski, 104 FW Bldg., National Bureau of Standards, Washington, D.C. 20234.
234. W. C. Walker, Department of Physics, University of California, Santa Barbara, Goleta, California.
235. G. L. Weissler, University of Southern California, Department of Physics, Los Angeles, California 90007.
236. R. E. Wilems, No. 3, Hillside Court E, Morris Plains, N.J. 07950.
237. S. E. Williams, University of Western Australia, Perth, Australia.
238. F. T. Wooten, Lawrence Radiation Laboratory, University of California, Berkeley, California.
239. S. Yamaguchi, Department of Physics, Tokyo Metropolitan University, Setagaya-ku, Tokyo, Japan.
240. A.Y.-C. Yu, Fairchild Semiconductor, Research and Development Lab., Palo Alto, California.
241. Laboratory and University Division, AEC, ORO
242-256. Division of Technical Information Extension, ORO.